https://theses.gla.ac.uk/

Theses Digitisation:

https://www.gla.ac.uk/myglasgow/research/enlighten/theses/digitisation/

This is a digitised version of the original print thesis.

Copyright and moral rights for this work are retained by the author

A copy can be downloaded for personal non-commercial research or study, without prior permission or charge

This work cannot be reproduced or quoted extensively from without first obtaining permission in writing from the author

The content must not be changed in any way or sold commercially in any format or medium without the formal permission of the author

When referring to this work, full bibliographic details including the author, title, awarding institution and date of the thesis must be given

Enlighten: Theses
https://theses.gla.ac.uk/
research-enlighten@glasgow.ac.uk

A STUDY OF HADRONIC FINAL STATES IN e^+e^- ANNIHILATION AT 44 GeV

by

Graham Munro McCurrach
Department of Natural Philosophy
University of Glasgow

Submitted for the degree of Ph.D.
at the University of Glasgow

March 1987

ProQuest Number: 10995564

All rights reserved

INFORMATION TO ALL USERS
The quality of this reproduction is dependent upon the quality of the copy submitted.

In the unlikely event that the author did not send a complete manuscript
and there are missing pages, these will be noted. Also, if material had to be removed,
a note will indicate the deletion.

ProQuest 10995564

Published by ProQuest LLC (2018). Copyright of the Dissertation is held by the Author.

All rights reserved.
This work is protected against unauthorized copying under Title 17, United States Code
Microform Edition © ProQuest LLC.

ProQuest LLC.
789 East Eisenhower Parkway
P.O. Box 1346
Ann Arbor, MI 48106 – 1346

ABSTRACT

The analysis of multihadronic events resulting from the interaction of an electron and a positron has been carried out using the data obtained with the CELLO detector situated at the PETRA e^+e^- storage ring. There are 5605 events in the data sample which were acquired at an average beam energy of 22 GeV.

These events were used to ascertain whether the hadronic data could be described by a candidate theory of the strong interaction; namely quantum chromodynamics. It is shown that quantum chromodynamics describes the main features of the data.

The theoretical properties of the transition from quark and gluons to hadrons is discussed, and in particular, three models of fragmentation are discussed. The relative merits of the string model, the independent jet model and the cluster model were evaluated from an experimental viewpoint and on a theoretical basis. The string model of fragmentation was found to give the best agreement with the published experimental data.

Using the string model of fragmentation, a value of α_S, the strong interaction coupling constant, was obtained. This was done by statistically fitting the experimental corrected data to the theoretical quantum chromodynamic prediction. Various distributions were employed to determine α_S and their relative merits assessed. It was found that the energy energy correlation asymmetry provided the most accurate measure of the strong coupling constant, namely,

$$\alpha_S(Q^2 = 1936GeV^2) = 0.152 \pm 0.010(\text{systematic}) \pm 0.01(\text{statistical})$$

PREFACE

This thesis describes the study of one-photon virtual exchange interactions carried out using data from the CELLO detector at the PETRA e^+e^- storage ring situated at DESY, Hamburg, W. Germany.

The study was designed to show that the strong interaction, one of the four fundamental forces, could be described by the theory of quantum chromodynamics and if this were true, to ascertain the strength of the strong interaction by determining the strong interaction coupling constant.

The results obtained in this thesis depend directly or indirectly on the work of many people, although the physics analysis presented in this analysis is the individual work of the author.

The author's individual contribution to the experiment included the supervision and maintainenance of the muon detectors and an analysis of the Monte Carlo at the generator level. The author was also involved in a study of the liquid argon calorimeter, and in particular, the energy deposition characteristics of photons in this part of the detector.

No portion of the work referred to in this thesis has been submitted in support of an application for another degree or qualification in this or any other university or institution of learning.

ACKNOWLEDGEMENTS

It is a pleasure to thank the many people who have helped me in various ways throughout the three years. Firstly, I would like to thank the other members of the CELLO Collaboration for all their help and encouragement, particularly Drs. Wim de Boer and Guilio d'Agostini, and Juan Fuster. I also enjoyed working closely with the Saclay group, and I am indebted to Dr. George Cozzika for his patience in teaching me about the muon chambers.

I wish to thank the Department of Natural Philosophy under Prof. E.Laing and the High Energy Physics group under Prof. I.Hughes for giving me the opportunity to undertake this research. My thanks also go to my supervisor Dr. Peter Bussey for his help, guidance and encouragement during this study, to Prof. Ian Skillicorn for his advice and help and to Dr. Ken Smith for his interest over the years.

The task of arranging travel, finding some accommodation and dealing smoothly with the Science and Engineering Research Council was carried out competently and in their usual friendly manner by Catherine McIntyre in Glasgow and Josephine Zilberkweit in Hamburg.

There are many friends and collagues who helped to make this time of research an enjoyable experience; in my first year Juls, Stan, Alan, together with Stephen who also kept me in touch with happenings at Glasgow throughout my stay in Hamburg, in his unbiased manner. In my two years abroad in Hamburg many people had to listen to my ramblings and noises in the Desy cafeteria and elsewhere including Paul, Tim, Jan, Richard, Susan, John, Alan, Denis, Craig, Janice, Sandra, Nia, Ian and Pamela.

Thanks also to several friends who also helped me directly in my work; Alan for introducing me to the software side of CELLO, Denis for introducing me to GEP and sharing an office with me and my drying socks, and

to Craig who also shared an office with me and my output and who helped with the assembling of this thesis by sending text to Glasgow after I had left Hamburg. I also thank the computing support staff in Hamburg and Glasgow for their work and advice.

I would also like to thank the Science and Engineering Research Council for their financial support throughout the three years.

Finally, thanks to all my friends who kept in touch when I was in Hamburg and to my family for all their support and encouragement.

TABLE OF CONTENTS

ABSTRACT i

PREFACE ii

ACKNOWLEDGEMENTS iii

TABLE OF CONTENTS v

CHAPTER 1. THEORETICAL INTRODUCTION 1

1.1 Introduction to particle physics 1

1.2 The Glashow-Salam-Weinberg model 2

1.3 Gluons and colour 4

1.4 Quantum chromodynamics 6

1.5 Calculations in QCD 7

1.6 Renormalisation in QCD 9

1.7 Asymptotic freedom 10

1.8 e^+e annihilation into jets in QCD perturbation theory 11

1.8.1 Fixed order QCD 12

1.8.2 Leading-log QCD 14

1.9 Shape variables in e^+e^- annihilation 14

CHAPTER 2. EXPERIMENTAL STATUS OF QCD 18

2.1 Introduction. 18

2.2 Deep inelastic lepton nucleon scattering 18

2.3 e^+e^- annihilation into hadrons 19

(a) The total cross section 19

(b) Observation of jets 20

2.4 Monte Carlo hadronization models 21

2.4.1 Independent jet model 22

2.4.2 String fragmentation model 25

2.4.3 Cluster fragmentation models 27

2.5 Comparison of hadronization models 29
2.6 Previous determinations of α_S 30
CHAPTER 3. PETRA AND THE CELLO DETECTOR 35
3.1 Introduction 35
3.2 PETRA 35
3.3 The CELLO Detector 36
3.4 The superconducting solenoid 37
3.5 The central tracking detector 37
3.6 The end cap proportional wire chambers 39
3.7 The lead liquid argon calorimeter 39
3.8 The muon detector 40
3.9 The forward detector 41
3.10 The trigger 42
3.10.1 The charged particle trigger 42
3.10.2 The neutral particle trigger 43
3.11 The hole tagger 44
CHAPTER 4. DATA ACQUISITION AND EVENT SELECTION . 45
4.1 Introduction. 45
4.2 Data acquisition system 45
4.3 Use of the emulator 47
4.4 The filter program 48
4.5 The reconstruction program 51
4.6 Event selection 52
CHAPTER 5. STUDY OF HADRONIC FINAL STATES 55
5.1 Introduction 55
5.2 The variables used 55
5.3 Energy-energy correlations 57
5.4 Further track and event selection 58
5.5 Correcting the data 61

5.6 The distributions 67
(a) Sphericity 67
(b) Thrust 67
(c) Angular distribution of the sphericity axis 67
(d) Angular distribution of the thrust axis 67
(e) Particle momenta 68
(f) Particle production with respect to the jet axis 68
(g) Rapidity 69
(h) Topological event measures 69
(i) Energy-energy correlations 70
5.7 Summary 70
Chapter 6. DETERMINATION OF α_S 71
6.1 Introduction. 71
6.2 The Procedure 71
6.3 Results 72
CHAPTER 7. SUMMARY AND CONCLUSIONS 76
The CELLO Collaboration 79
REFERENCES 80

CHAPTER ONE

THEORETICAL INTRODUCTION

1.1 Introduction to particle physics

Research into high energy physics is carried out to try to discover the fundamental structure of matter. At the beginning of the twentieth century it was believed that 92 atomic elements were the elementary building blocks of nature. Then came the discovery that the atoms themselves were made up of a nucleus containing protons and neutrons surrounded by clouds of orbiting electrons. At present, there are thought to be three main groups of elementary particles; quarks, leptons and gauge bosons, some properties of which are shown in table 1.1.

Four known forces dictate the way in which these particles interact. The most familiar force is the electromagnetic force, which through the mediation of photons influences charged particles. This force dominates outside the nucleus and is hence responsible for much of chemistry, biology and everyday life. The weak force is responsible for many nuclear processes such as the beta decay of neutrons into protons and is thought to act through the exchange of weak bosons. Quarks are bound together by the strong force, carried by gluons, and all particles which undergo strong interactions are called hadrons. All particles are influenced by the gravitational force but this interaction is negligible at present energies, compared with the other three forces. The strong force is a million times stronger than the weak force and a thousand times the strength of the electromagnetic force.

The calculational framework of modern particle physics is relativistic quantum field theory, of which quantum electrodynamics (the theory describing the electromagnetic interactions of photons and electrons) is the prototype. During the last twenty years, the importance of a special class

Group	Symbol	Name	Spin	Charge
Quarks	u	up	$\frac{1}{2}$	$\frac{2}{3}$
	d	down	$\frac{1}{2}$	$-\frac{1}{3}$
	s	strange	$\frac{1}{2}$	$-\frac{1}{3}$
	c	charm	$\frac{1}{2}$	$\frac{2}{3}$
	b	bottom	$\frac{1}{2}$	$-\frac{1}{3}$
	t	top	$\frac{1}{2}$	$\frac{2}{3}$
Leptons	e	electron	$\frac{1}{2}$	-1
	μ	muon	$\frac{1}{2}$	-1
	τ	tauon	$\frac{1}{2}$	-1
	ν_e	$e-$ neutrino	$\frac{1}{2}$	0
	ν_μ	$\mu-$ neutrino	$\frac{1}{2}$	0
	ν_τ	$\tau-$ neutrino	$\frac{1}{2}$	0
Gauge Bosons	γ	photon	1	0
	W^+		1	+1
	W^-	weak bosons	1	-1
	Z		1	0
	$g_i (i = 1 \ldots 8)$	gluons	1	0

Table 1.1 : The main groups of elementary particles and some of their properties. The unit of charge is defined in such a way that the electron charge is -1. The spin is given in units of $\hbar$.

of quantum field theory, called gauge theories has become apparent. Quantum electrodynamics (or QED) is the simplest example of such a theory, while another example is the theory of the strong interaction; quantum chromodynamics (or QCD).

The electromagnetic and weak interactions are unified in the Glashow-Salam-Weinberg model, which together with quantum chromodynamics forms the standard model of elementary particle interactions.

1.2 The Glashow-Salam-Weinberg model

The application of the gauge principle to the weak interactions of quarks and leptons produced a model which led to the electromagnetic and the weak interactions being unified.

The relevant symmetry group was first proposed by Glashow [**1**] in 1961 and then investigated by Weinberg [**2**] in 1967 and Salam [**3**] in 1968. Glashow recognised that the interactions were invariant under weak isospin $SU(2)_L$ transformations, suggested by the fact that the coupling of the weak interaction to both quarks and leptons has the same strength. He also saw that a second symmetry was involved,i.e., the $U(1)_Y$ symmetry of the electromagnetic interaction.

An $SU(2) \times U(1)$ invariant Lagrangian could then be constructed by combining these two transformations. This is done by replacing the basic electromagnetic interaction, as used in QED to calculate electromagnetic amplitudes, with two basic interactions

$$-igJ_\mu \cdot W^\mu = -ig\bar{\psi}_L \gamma_\mu T \cdot W^\mu \psi_L$$
$$-i\frac{g'}{2} j_\mu^Y B^\mu = -g'\bar{\psi}\gamma_\mu \frac{Y}{2}\psi B^\mu$$

The first of these interactions involves an isotriplet of weak currents J_μ

coupling to three vector bosons W^μ with the operators T being the generators of the $SU(2)_L$ group. In the second interaction, a weak hypercharge current j^Y_μ is coupled to a fourth vector boson B^μ with Y the generator of $U(1)_Y$.

The fundamental constants g and g' represent the couplings of the $SU(2)_L$ and $U(1)_Y$ parts of the gauge group respectively.

Since the weak isospin assignments and associated transformation properties apply to the left-handed parts of the wavefunctions only, the left-handed fermions form isospin doublets ψ_L while the right- handed fermions are isosinglets ψ_R.

Thus for leptons we have

$$\psi_L = \begin{pmatrix} \nu \\ e \end{pmatrix}_L \qquad \psi_R = e_R$$

and for quarks

$$\psi_L = \begin{pmatrix} u \\ d' \end{pmatrix}_L \qquad \psi_R = u_R \text{ or } d_R$$

The Kobayashi-Maskawa matrix [4] determines the combinations in the charged current. The electromagnetic current is a combination of the two neutral currents J^3_μ and j^Y_μ and the two physical neutral gauge fields A_μ and Z_μ are combinations of the gauge fields W^3_μ and B_μ.

The Higgs mechanism has to be used to incorporate particle masses in a gauge invariant manner. This requires the addition of an isospin doublet of complex scalar fields, with $Y = 1$ and a non-zero vacuum expectation value, to the Lagrangian. Thus, the gauge symmetry is spontaneously broken with the theory remaining renormalizable, while the $W^\pm$ and the Z^0 become massive and the photon remains massless.

1.3 Gluons and colour

It is thought that the complexity of all hadronic matter, e.g. protons, neutrons and pions and all the other strongly interacting elementary particles can be considered to be made up of smaller building blocks called quarks. These are fermions, like the leptons, with spin $\frac{1}{2}$, with three quarks combining to form a baryon, and a quark and an antiquark forming a meson. The hadronic properties of charge, strangeness, charm, beauty and baryon number are all possessed by quarks although sometimes not in integer units, as can be seen from table 1.2.

At present accelerator energies five types of quarks called flavours are needed to explain the entire hadron spectrum,i.e., up, down, strange, charm and bottom. The u, d quarks transform as a doublet under an almost exact $SU(2)$ of flavour, the u, d, s transform as a triplet under an approximate $SU(3)$ of flavour, the u, d, s, c transform as a quartet under a badly broken $SU(4)$ of flavour.

A series of experiments on deep inelastic lepton scattering [**5**] showed that quarks were not merely mathematical objects used to construct hadrons, but behaved as freely moving, point-like objects. In these experiments, a nucleon is struck by a high momentum probe, which is usually a photon, as shown in figure 1.1. If the photon's momentum is high enough it will have a small enough wavelength to penetrate the hadron and thereby see the constituents inside, which are found to have all the quark properties. However, at today's energies these partons never seem to emerge from the hadron.

Since these partons do not appear as isolated objects outside the nucleon it has been postulated that they must have some property which is not possessed by hadrons. This property is called colour [**6**] and comes in,

	QUANTUM NUMBER				
QUARK	charge	strangeness	charm	beauty	baryon
u	2/3	0	0	0	1/3
d	-1/3	0	0	0	1/3
s	-1/3	-1	0	0	1/3
c	2/3	0	+1	0	1/3
b	-1/3	0	0	-1	1/3

Table 1.2 : Some of the quantum numbers of the five quark flavours

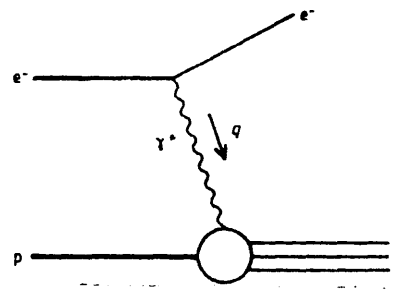

Figure 1.1 : Deep inelastic scattering $e^- p \rightarrow e^- X$

say, the three shades of red, green and blue.

The introduction of the concept of colour has explained why the lowest mass, spin 3/2 states of apparently identical quarks can exist. For example, three u quarks combine in a completely symmetric ground state to form the Δ^{++} baryon, which is a state forbidden by Fermi-Dirac statistics. However, with the introduction of colour the quark wavefunction for the Δ state can be written as $u_R u_G u_B$ and so the three u quarks are now distinguishable by their colour quantum number, thus solving the statistics problem.

A red, a green and a blue quark comprise every baryon, while a meson is a linear superposition of red-antired, green-antigreen, and blue- antiblue. Hadrons, although built of coloured quarks are colour-neutral or white, since they are observed in nature.

It is clear that a strong force is needed to bind the quarks together in the hadron and to overcome the electromagnetic repulsion of, for example the three u quarks in the Δ^{++} baryon. This force is mediated by gluons with two quarks exchanging a virtual gluon in an analogous fashion to the exchange of a virtual photon in quantum electrodynamics (QED). A schematic representation of this is given in figure 1.2.

The gluons are bicoloured objects and occur in nine varieties with the ability to interact with each other (see for example figure 1.3) under a colour transformation, apart from one combination, which is a colour singlet lacking any net colour charge and so cannot carry colour from one quark to another. This singlet gluon need not be confined and can couple to quarks with a strength independent of the other eight and since it is arbitrary, this coupling is set to zero. Eight gluons are then left and this octet is allowed to transform as the adjoint representation of $SU(3)$. The mediating gluons are required to have odd spin so that the colour forces that succeed in binding a $q\bar{q}$ pair into a meson fail with a qq pair. The spin is taken to be one since

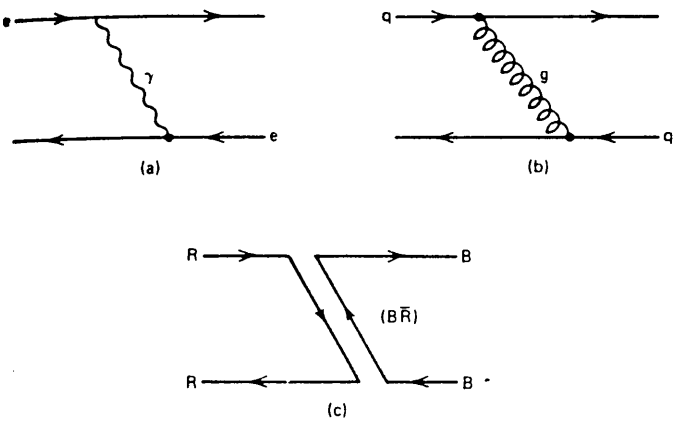

Figure 1.2 : (a) Electromagnetic interaction by photon exchange (b) Strong interaction by gluon exchange (c) Flow of colour in (b)

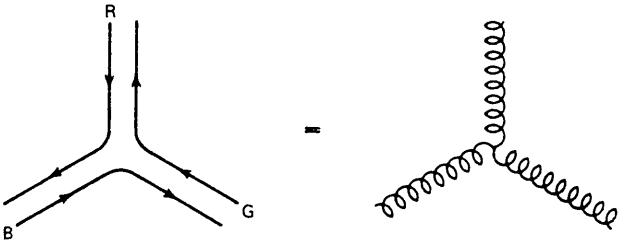

Figure 1.3 : Self-coupling of gluons

this is the only renormalizable choice.

1.4 Quantum chromodynamics

In quantum chromodynamics (QCD), a triplet of coloured quarks interacts through the exchange of an octet of vector gluons, described by a Yang-Mills gauge theory.

Spinors ψ_i ,where $i = 1, \ldots, N$, describe the quark fields and transform as the fundamental representation of $SU(N)$. The gluon fields are described by A_a^μ , where $a = 1, \ldots, (N^2 - 1)$, and transform according to the adjoint representation.

The $N \times N$ matrices $(T^a)_{ij}$ represent the $SU(N)$ transformations, and for $N = 3$ these matrices are just equal to $\frac{1}{2}\lambda_a$ where λ_a are the Gell-Mann matrices with $a = 1, \ldots, 8$.

The commutator of any two of these matrices is a linear combination of all the T's ;-

$$[T^a, T^b] = if^{abc}T^c \tag{1-1}$$

where f^{abc} are real constants and are called the structure constants of the group.

The QCD Lagrangian density assuming massless quarks is given by,

$$L_{QCD} = i\bar{\psi}_i\gamma_\mu D_{ij}^\mu\psi_j - \frac{1}{4}F_a^{\mu\nu}F_{a\mu\nu} \tag{1-2}$$

where the covariant derivative is defined as follows,

$$D_{ij}^\mu = \partial^\mu\delta_{ij} - ig(T^a)_{ij}A_a^\mu$$

and the field strength tensor is,

$$F_a^{\mu\nu} = \partial^\mu A_a^\nu - \partial^\nu A_a^\mu + gf^{abc}A_b^\mu A_c^\nu$$

with g the only coupling of the theory.

An Abelian theory like QED is easily obtained by setting $f^{abc} = 0$ in equation (1-1) and hence making the commutator zero. Equation (1-2) is thus the non-Abelian generalisation of a successful theory, namely QED.

The invariance of the Lagrangian is expressed in terms of $L_{QCD} \rightarrow L_{QCD}$ under any infinitesimal local gauge transformation defined by ϵ_a, such that

$$\psi_i \rightarrow \psi_i - i(T^a)_{ij}\psi_j\epsilon_a$$

$$\bar{\psi}_i \rightarrow \bar{\psi}_i + i\bar{\psi}_j(T^a)_{ji}\epsilon_a$$

$$A_a^\mu \rightarrow A_a^\mu + f^{abc}\epsilon_b A_c^\mu - \frac{1}{g}\partial^\mu\epsilon_a$$

This property of local gauge invariance uniquely determines the structure of the theory and made it consistent with unitarity.

One of the properties of any physical theory is that probability must be conserved in any scattering process. The high-energy behaviour of scattering amplitudes is thus severely constrained by the unitarity of the S-matrix. The renormalisability of the underlying field theory is closely related to this behaviour. Yang and Mills [7] recognised that imposing the condition of local gauge invariance made the theory renormalizable and so give sensible high energy behaviour for physical processes.

1.5 Calculations in QCD

There are two methods of performing calculations in QCD at the present time, using either lattice gauge theory or perturbation theory.

Lattice gauge theory methods attempt to compute properties directly derivable from the Lagrangian of equation (1-2). This technique is difficult and requires a large amount of computer time and hence present results

are only concerned with static problems, such as the spectrum of hadronic masses.

In order to perform calculations, the gauge freedom of QCD has to be removed by choosing a specific gauge of which the most common are the Feynman gauge, the Landau gauge and the axial gauge. Calculations in QCD using perturbation theory are carried out by applying the Feynman rules deduced from the Lagrangian, given in table 1.3. The two covariant gauges are specified by the parameter ζ with $\zeta = 0$ being the Landau gauge and $\zeta = 1$ the Feynman gauge.

The gluon propagator, however, has too many degrees of freedom for a massless physical vector particle and in effect includes an unphysical scalar component, which must be removed. This is achieved by adding appropriate ghost fields to the Lagrangian with contributions arising wherever there are gluon loops. If the axial gauge is used, no ghost terms are needed.

The presence of gluon and fermion loops in some graphs in perturbative QCD leads to the appearance of three types of colour factor. Two of these are the Casimirs $C(F)$ and $C(A)$, while the third is the trace factor $T(F)$, which are shown diagrammatically in figure 1.4.

For $SU(N)$ and N_f flavours, we have

$$\sum_{a=1}^{N^2-1} \sum_{k=1}^{N} T^a_{ik} T^a_{kj} \equiv C(F)\delta_{ij} = \left(\frac{N^2-1}{2N}\right)\delta_{ij}$$

$$\sum_{c,d=1}^{N^2-1} f_{acd} f_{bcd} \equiv C(A)\delta_{ab} = N\delta_{ab}$$

$$N_f \sum_{i,j=1}^{N} T^a_{ji} T^b_{ij} \equiv N_f T(F)\delta_{ab} = \frac{N_f}{2}\delta_{ab}$$

Feynman rules	Covariant gauge (ξ)	Axial gauge (n^μ)
	$-i\frac{\delta_{ij}}{\not{p}}$	$\frac{\delta_{ij}}{\not{p}}$
	$-i\frac{\delta_{ab}}{q^2}\left(g^{\mu\nu}-\frac{q^\mu q^\nu}{q^2}+\xi\frac{q^\mu q^\nu}{q^2}\right)$	$-i\frac{\delta_{ab}}{q^2}\left(g^{\mu\nu}-\frac{n^\mu q^\nu+q^\mu n^\nu}{n\cdot q}+\frac{n^2 q^\mu q^\nu}{(n\cdot q)^2}\right)$
	$-i\frac{\delta_{ab}}{q^2}$	None
	$-igT^a_{ij}\gamma^\mu$	$-igT^a_{ij}\gamma^\mu$
	$-gf_{abc}q^\mu$	None
	$-gf_{abc}[g_{\lambda\mu}(p-q)_\nu+g_{\mu\nu}(q-r)_\lambda$ $+g_{\nu\lambda}(r-p)_\mu]$	$-gf_{abc}[g_{\lambda\mu}(p-q)_\nu+g_{\mu\nu}(q-r)_\lambda$ $+g_{\nu\lambda}(r-p)_\mu]$
	$-ig^2[f_{abe}f_{cde}(g_{\kappa\mu}g_{\lambda\nu}-g_{\kappa\nu}g_{\lambda\mu})$ $+f_{ace}f_{bde}(g_{\kappa\lambda}g_{\mu\nu}-g_{\kappa\nu}g_{\lambda\mu})$ $+f_{ade}f_{cbe}(g_{\kappa\mu}g_{\lambda\nu}-g_{\kappa\lambda}g_{\mu\nu})]$	$-ig^2[f_{abe}f_{cde}(g_{\kappa\mu}g_{\lambda\nu}-g_{\kappa\nu}g_{\lambda\mu})$ $+f_{ace}f_{bde}(g_{\kappa\lambda}g_{\mu\nu}-g_{\kappa\nu}g_{\lambda\mu})$ $+f_{ade}f_{cbe}(g_{\kappa\mu}g_{\lambda\nu}-g_{\kappa\lambda}g_{\mu\nu})]$

Table 1.3 : The Feynman rules for performing calculations in QCD

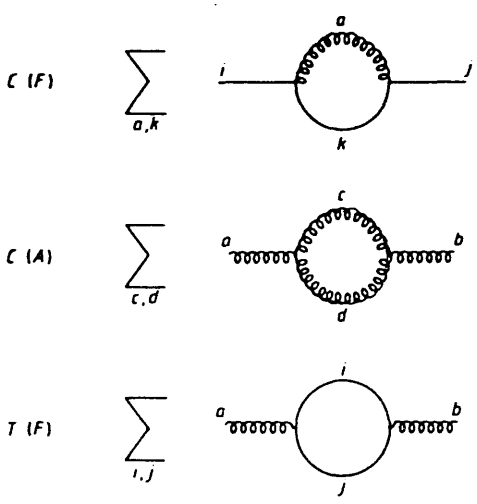

Figure 1.4 : Diagrammatic representation of the two Casimirs and the trace factor for $SU(N)$

1.6 Renormalisation in QCD

There are two types of diagrams or terms, called loop and tree diagrams respectively, in a perturbative expansion. In the loop diagrams, examples of which can be seen in figure 1.5(a), an intermediate virtual state is created and then destroyed, and these represent the higher order corrections. The tree diagrams, such as those in figure 1.5(b), have no such loops and correspond to the lowest order terms. Mathematical difficulties occur in the calculation of loop diagrams because integrations need to be performed over the momenta of the intermediate particles. These integrals are usually divergent, since they extend up to infinite momenta, and hence reflect the failure of the theory at large momenta. This problem is dealt with using the procedure of renormalisation.

This means that the infinities of the theory are absorbed into the basic constants of the theory, such as the coupling constants and masses, which are then renormalized to their finite physical values. Hence, these coupling constants and masses cannot be calculated in this theory and must be measured experimentally.

The Lagrangian is then rewritten in terms of the renormalized fields ψ_R and $A_a^{\mu,r}$, which are given by ;

$$\psi = Z_2^{1/2}\psi_R$$

$$A_a^{\mu} = Z_3^{1/2}A_a^{\mu,r}$$

where Z_2 and Z_3 are the renormalization constants of the quark and gluon field respectively.

The renormalization constants are determined by using a particular renormalisation scheme, of which there are three main examples.

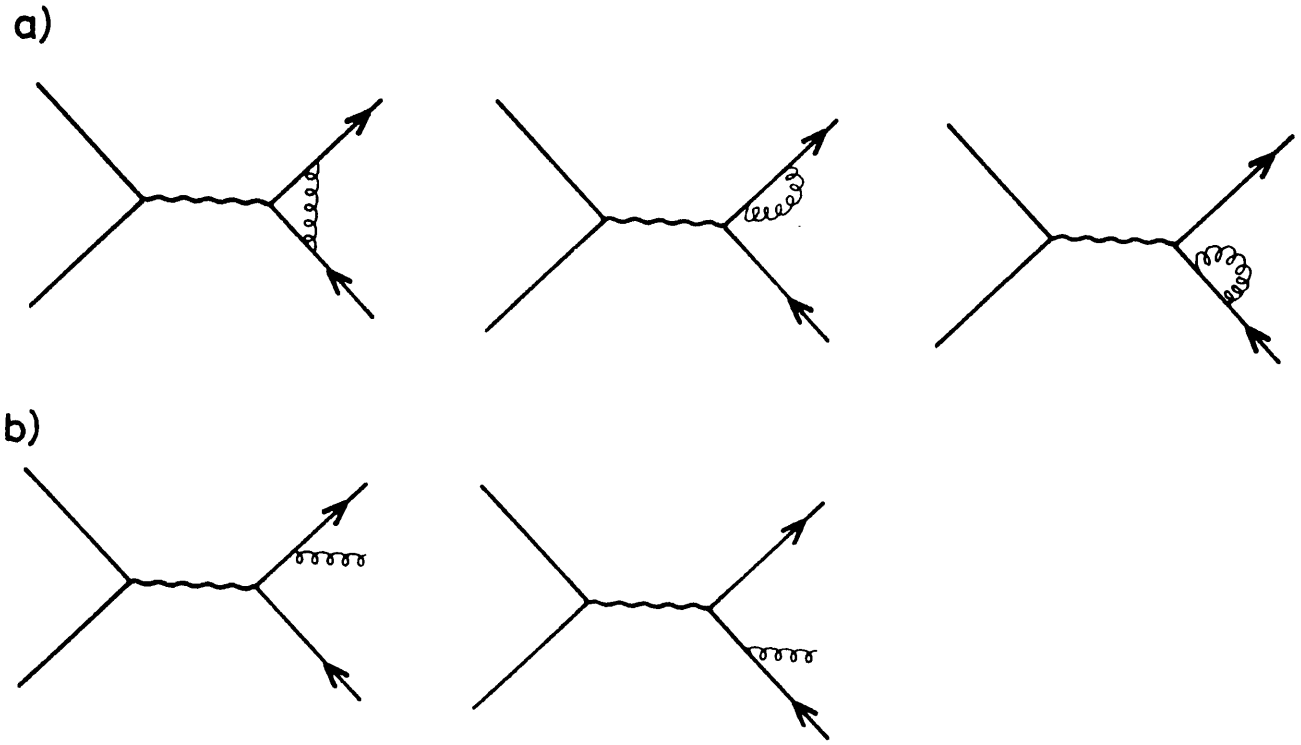

Figure 1.5 : Feynman diagrams for (a) $q\bar{q}$ and (b) $q\bar{q}g$ production to order α_S

The minimal subtraction (ms) scheme uses the method of dimensional regularisation and has the advantage of being gauge-independent. This increases the number of space-time dimensions, X, to a number other than four and then the infinities appear as simple poles at $X = 4$. A finite result is obtained by subtracting these poles $\sim \frac{1}{X-4}$ The disadvantage of this scheme is that the momentum scale is introduced solely on dimensional grounds. The modified minimal subtraction scheme ($\overline{ms}$) involves the removal of constants like $(ln4\pi - \gamma_E)$, where γ_E is the Euler-Mascheroni constant, which appear in many quantities through dimensional regularisation. A third scheme is momentum subtraction (mom) in which the vertices and the coupling are renormalized at a momentum close to the momentum of interest. This method has the disadvantage of being gauge-dependent.

Physical quantities should not depend on the particular renormalisation scheme used and so perturbative expansions carried out to all orders should yield the same result.

1.7 Asymptotic freedom

The quark-gluon interaction of QCD that binds a hadron together would seem to be an even stronger force, with a larger coupling, than the force that keeps a nucleus intact. This is suggested by the fact that free quarks and gluons have not been observed in nature i.e., they are confined in colour singlet hadron states. In deep inelastic scattering experiments using a high momentum probe however, the quarks appear to be freely moving particles with an effectively small coupling. The procedure of renormalisation provides the solution to this apparent contradiction and leads to the property of asymptotic freedom.

In the process of renormalisation, the coupling g is renormalised by defining its value to be $g(\mu^2)$ at some new momentum scale $Q^2 = \mu^2$. This

momentum scale is usually taken in e^+e^- annihilation to be the centre of mass energy squared, denoted by s.

The behaviour of $g(\mu^2)$ is defined by the differential equation

$$\beta(g) = \mu \frac{\partial}{\partial \mu} g$$

where the β function can be calculated in perturbation theory.

Defining $\alpha_S(Q^2) \equiv \frac{g^2(Q^2)}{4\pi}$ this equation gives the solution,

$$\alpha_S(Q^2) = \frac{\alpha_S(\mu^2)}{1 + \left(\frac{\beta_0}{4\pi}\right) \alpha_S(\mu^2) ln\left(\frac{Q^2}{\mu^2}\right)}$$

which can be rewritten as

$$\alpha_S^{(1)}(Q^2) = \frac{12\pi}{(33 - 2N_f) ln\left(\frac{Q^2}{\Lambda_{LL}^2}\right)}$$

where N_f is the number of quark flavours and Λ_{LL} is a constant defined by

$$\alpha_S^{(2)}(Q^2) = \frac{12\pi}{(33 - 2N_f) ln\left(\frac{Q^2}{\Lambda_{LL}^2}\right) + 6\left(\frac{153 - 19N_f}{33 - 2N_f}\right) ln\left(ln\left(\frac{Q^2}{\Lambda_{LL}^2}\right)\right)} \qquad (1\text{–}3)$$

From equation (1-3) it can be seen that as Q^2 increases, $\alpha_S^{(2)}(Q^2)$ decreases and is therefore small for high Q^2 (short distance) interactions such as are found in deep inelastic scattering. Hence, for high Q^2 processes the perturbative expansion converges quickly as $\alpha_S^{(2)}(Q^2)$ is small, while low Q^2 processes are difficult, if not impossible, to calculate. The theory of QCD is thus said to be asymptotically free.

1.8 e^+e^- annihilation into jets in QCD peturbation theory

In e^+e^- annihilation, the hadrons that are formed from the interaction of the underlying partons are found to be produced in jets of particles.

The partons possess a spread in momentum since they are confined to the interaction region. This effect is enhanced in the transverse direction with respect to the beam axis, thus giving the partons an intrinsic transverse momentum. Thus, in turn, the hadrons are produced in jets or cones, with a limited transverse momentum of a few hundred MeV with respect to the original parton direction.

There are two different methods used to describe the evolution of partons in e^+e^- annihilation. The first method is known as fixed order QCD, where every term in a perturbative expansion is used up to a given order, with the higher order terms being ignored. This is in contrast to leading-log QCD, in which the largest contributions from all orders are summed, while the non-leading terms at each stage are neglected.

The process which leads to the production of hadrons from the initial state partons is not calculable in QCD. Thus, several phenomenological models have been introduced to describe this fragmentation process, and these will be discussed in the next chapter.

1.8.1 Fixed order QCD

The diagrams that contribute to the process $e^+e^- \rightarrow q\bar{q}$ and are of order α_S are shown in figure 1.5(a,b). The graphs in figure 1.5(a) are $O(\alpha_S)$ and are multiplied by the zeroth order diagram of figure 1.6 thus giving the $O(\alpha_S)$ corrections to the two jet cross section $e^+e^- \rightarrow q\bar{q}$. Each of these diagrams is ultraviolet divergent, i.e., the integrals over the virtual momenta k diverge as $k \rightarrow \infty$. However, the divergences cancel when the contributions from all three graphs are summed, but divergences still arise when $k \rightarrow 0$, because the gluon is thought to be massless. These infra-red divergences cancel if the contributions from the process $e^+e^- \rightarrow q\bar{q}g$, which also have infra-red divergences, are added. Another divergence, called the

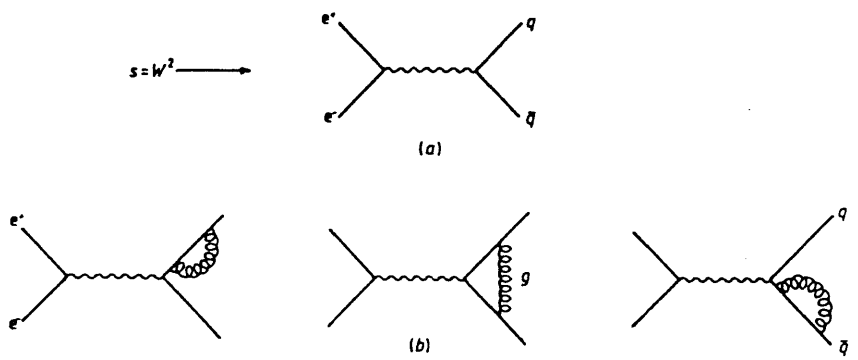

Figure 1.6 : The process $e^+e^- \rightarrow q\bar{q}$ (a) to zeroth order (b) to $O(\alpha_S$ i.e., the one-gluon corrections

collinear divergence, occurs when the virtual gluon is collinear with the outgoing quark ,i.e., Θ, the angle between the quark and the gluon , $\rightarrow 0$.

The dimensional regularization procedure of 't Hooft [**8**], as mentioned earlier, defines these divergent integrals and hence controls the divergences.

Figure 1.5(b) contains the gluon bremsstrahlung diagrams which also need to be considered for the process $e^+e^- \rightarrow q\bar{q}g$ up to order α_S.

One more gluon can be emitted from one of the quark branches if order α_S^2 effects are considered. This leads to a four parton final state, which is interpreted as the production of four jets. The two processes that produce final states are $e^+e^- \rightarrow q\bar{q}gg$ and $e^+e^- \rightarrow q\bar{q}q\bar{q}$, the diagrams for which are shown in figure 1.7. Four jet events are produced only in kinematic regions away from degenerate regions, which is where some of the partons are collinear or soft. The degenerate regions correspond to two and three jets and give infrared and mass singularities on integration.

The divergences in three jet cross section are cancelled by the $O(\alpha_S^2)$ virtual corrections to 3 jets shown in figure 1.7. The two jet divergences cancel if the virtual two loop corrections to the $q\bar{q}$ final state are considered with the 2 jet contribution in the virtual $q\bar{q}g$ diagrams of figure 1.8.

The second order three parton final state correction has been calculated by several groups, known as the FKSS[**9**], ERT[**10**] and VGO[**11**] groups respectively. These three groups obtain different results largely as a result of using different cutoff procedures in order to decide whether two partons should be classified as two separate jets. These differences are now understood and the generator in the Monte Carlo used in this study employs the calculations of the FKSS group.

It has recently been suggested [**12**] that the approximations used for the four parton cross section are invalid because the neglected terms are not

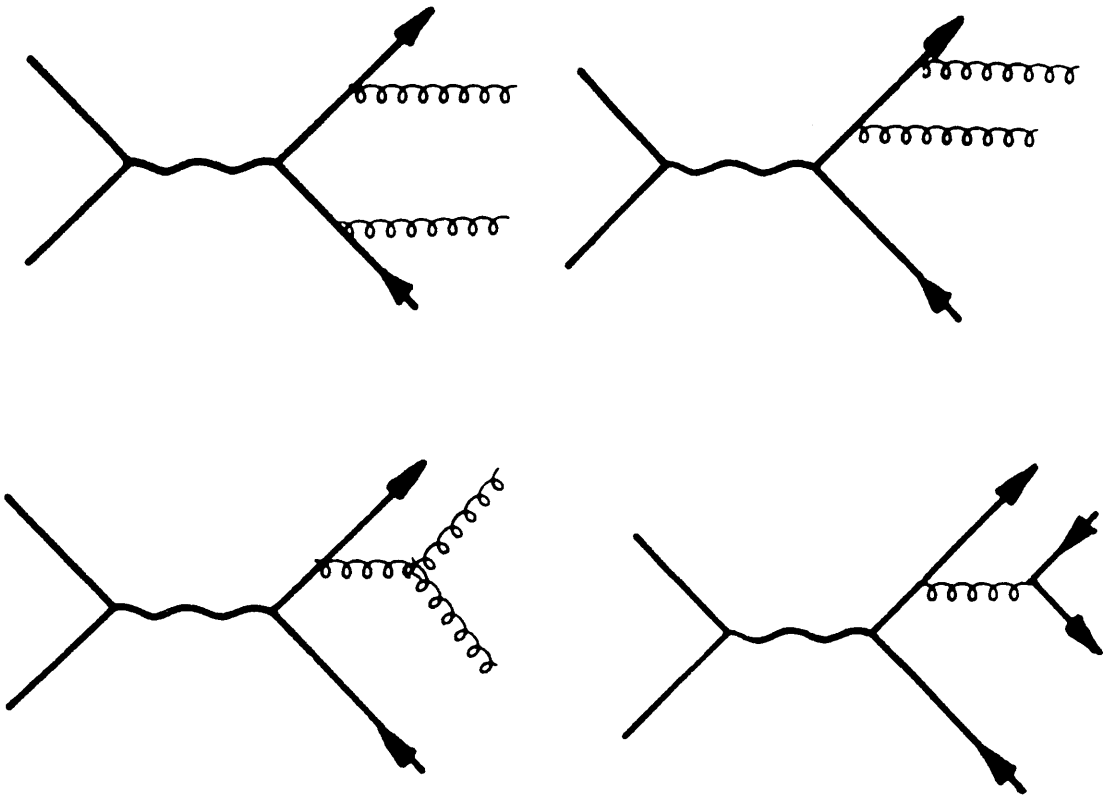

Figure 1.7 : Feynman diagrams with four partons ($q\bar{q}gg$ and $q\bar{q}q\bar{q}$) in the final state

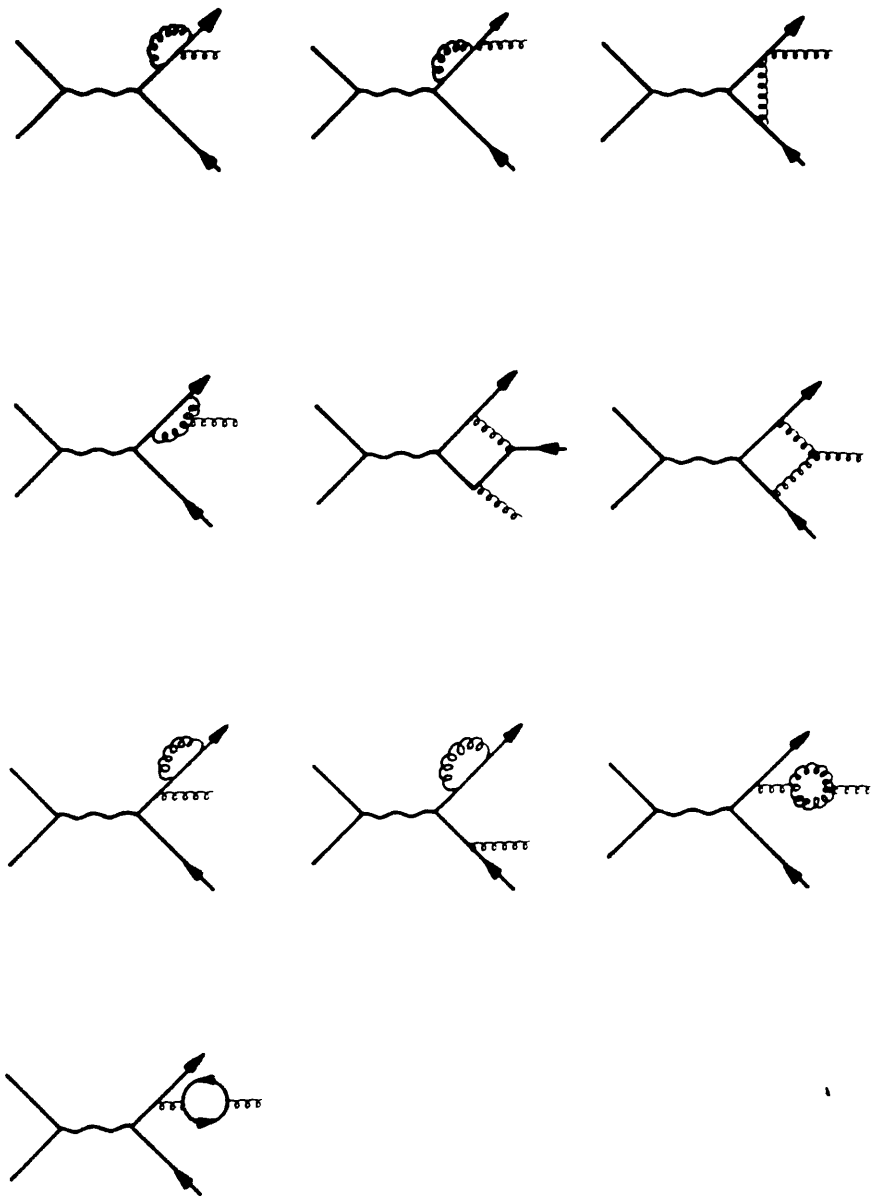

Figure 1.8 : Feynman diagrams with $q\bar{q}g$ in the final state to order α_S^2

negligible. However, this point is still a matter of debate amongst theorists and as such, will not be considered further in this work.

1.8.2 Leading-log QCD

In e^+e^- annihilation, the initial quark-antiquark pair are produced with a mass scale determined by the energy of the virtual photon. If a parton then radiates another parton its mass is reduced since it has lost part of its energy and momentum. This process of parton radiation leads to the production of a parton shower by which the initial state partons evolve through multiple gluon radiation. This evolution occurs perturbatively and can be calculated using the leading-log approximation. The shower continues until the mass of the parton reaches a small cutoff value. The advantage of the leading-log method is that the development of a parton system can be described over the whole time period for which perturbation theory is valid. This is in contrast to the fixed order method, which is only applicable for a short period of time. The details of the leading-log approximation can be found in the review article on QCD by Pennington [**13**]

1.9 Shape variables in e^+e^- annihilation

In the simple quark parton model, the process $e^+e^- \rightarrow q\bar{q} \rightarrow hadrons$ produces two identical jets of hadrons back-to-back. When processes such as $e^+e^- \rightarrow q\bar{q}g$ are allowed by perturbative QCD this simple picture of the event shape becomes more complex. At high energies, the two-jet system becomes asymmetric with a fat jet, from say the qg subsystem, recoiling against a slim jet, from the antiquark. The emission of a wide-angle high energy gluon leads to a distinct three-jet structure, when the centre of mass energy is sufficiently high.

Shape variables are used to measure and quantify this jet structure in e^+e^- annihilation events.

The most common shape variables are those determined using the second- rank momentum tensor [**14**] ;

$$M_{\alpha\beta} = \sum_{j=1}^{N} P_{j\alpha} P_{j\beta} \qquad (\alpha, \beta = x, y, z) \tag{1-4}$$

where N is the number of particles in the event, and P_{2y}, for example, is the momentum of the second particle in the y-direction (as defined in a right handed Cartesian coordinate system). The unit eigenvectors $\hat{n}_1, \hat{n}_2, \hat{n}_3$ have corresponding normalised eigenvalues given by

$$Q_k = \frac{\sum_{j=1}^{N} (\vec{p}_j \cdot \hat{n}_k)^2}{\sum_{j=1}^{N} p_j^2} \qquad k = 1, 2, 3$$

These eigenvalues satisfy the equation

$$Q_1 + Q_2 + Q_3 = 1$$

and are ordered such that

$$Q_1 \leq Q_2 \leq Q_3$$

The plane defined by $\hat{n}_2$ and $\hat{n}_3$ is called the event plane, while the sphericity axis is defined as the direction $\hat{n}_3$. These vectors are shown schematically in figure 1.9, together with $\hat{n}_1$, which defines the direction in which the sum of the momentum components is minimal.

From the above eigenvalues the quantities sphericity, S, and aplanarity, A, can be calculated,

$$S = \frac{3}{2}(Q_1 + Q_2)$$

$$A = \frac{3}{2}(Q_1)$$

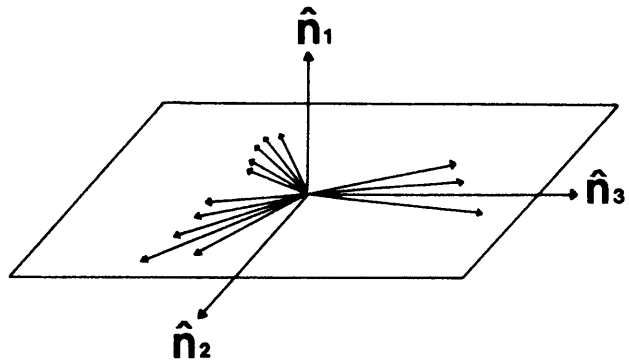

Figure 1.9 : The coordinate system determined for a three-jet event by the momentum tensor

The sphericity of an event is a measure of how well the event shape resembles that of a spherical as opposed to an elongated structure. A collinear two jet system has $S = 0$ while an isotropic event has $S = 1$.

A measure of the extent to which the event structure is not planar is given by aplanarity, since it gives the minimum squared momentum out of the event plane. Hence, flat events have $A = 0$.

However, the above variables are incalculable in QCD perturbation theory since the cancellation of collinear divergences arising from gluon bremstrahlung cannot occur. This is because the sum in equation (1-4) is quadratic in particle momenta, and hence changes when one momentum is replaced by a collinear sum of momenta ,i.e.,

$$p_i \rightarrow p_i^a + p_i^b = p_i$$

Infra-red safe variables were proposed to solve this problem, and are essentially linear in particle momenta, which allows the cancellation of perturbative divergences to take place.

One such variable is thrust [**15**], defined as

$$T = max \frac{\sum |p_j^L|}{\sum |p_j|}$$

where p_j^L is the longitudinal particle momentum of the jth particle relative to an axis chosen to maximize $\sum |p_j^L|$.

The major axis, $\hat{e}_2$, is perpendicular to the thrust axis, $\hat{e}_1$, and is the direction along which the projected energy flow in the plane perpendicular to $\hat{e}_1$ is a maximum. The minor axis, $\hat{e}_3$, is chosen to be orthogonal to $\hat{e}_1$ and $\hat{e}_2$.

Thus,

$$\text{Major} = max \frac{\sum |p_j \cdot \hat{e}_2|}{\sum |p_j|}$$

$$\text{Minor} = max \frac{\sum |p_j \cdot \hat{e}_3|}{\sum |p_j|}$$

This leads to the definition of the jet measure, oblateness as,

$$\text{oblateness} = \text{Major} - \text{Minor}$$

The values for T range between 0.5 for isotropic events and 1 for a collinear configuration, whilst the oblateness is 0 for a two-jet event.

One problem that arises when using the thrust variable, is that the introduction of an arbitrary cutoff parameter as one of the limits of integration in the integral of the differential thrust distribution, leads to a systematic uncertainty in the results. This is because the $O(\alpha_S)$ perturbative thrust distribution diverges for $T \rightarrow 1$.

This phenomenon is related to the singularities discussed earlier with the $O(\alpha_S)$ virtual corrections to two jet events yielding additional divergences at $T = 1$.

This problem is solved by introducing a cut-off parameter T_C, which makes the integral convergent and hence cancels the real and virtual divergences. However, this solution means that there is no reliable $O(\alpha_S)$ prediction for the thrust distribution in the region $T_c \leq T \leq 1$.

In the section of this study devoted to the determination of α_S , both infrared safe and unsafe variables will be used. This is because it has been found that at PETRA energies the $M_{\alpha\beta}$ variables may provide more sensitive tests of jet structure.

Other variables such as the energy energy correlation asymmetry will be defined in the relevant analysis chapter.

CHAPTER TWO

EXPERIMENTAL STATUS OF QCD

2.1 Introduction

As mentioned earlier, hadronic matter is thought to be composed of quarks, which are bound together by colour fields with gluons being the quanta of the colour field. The theory of quantum chromodynamics describes the interaction between the quarks and gluons.

The evidence for hadrons being composed of quarks comes from three main areas of study. These are the spectroscopy of hadrons, deep inelastic lepton scattering and e^+e^- annihilation physics. The latter two topics are discussed below, whilst a review of hadron spectroscopy can be found in the publication by Soding and Wolf [**16**].

2.2 Deep inelastic lepton nucleon scattering

In the late 1960's and early 1970's, scattering experiments involving electrons and nucleons, such as those illustrated in figure 1.1, where a high momentum probe strikes a nucleon, showed that the nucleon structure functions were approximately scale invariant. This behaviour was evidence for the existence of virtually free, pointlike partons within the nucleons. Later, 't Hooft interpreted the success of the quark-parton model in describing these results as being a consequence of asymptotic freedom and this led to the proposal of a nonabelian gauge field theory of the strong interaction. Scaling is however, not expected to hold exactly in field theories of the strong interaction because of gluonic radiative corrections. Evidence for these corrections has been found in scattering experiments [**17**] where the range of momentum transfers has been increased to $Q^2 \sim 200GeV^2$. Thus,

the theory of quantum chromodynamics can be tested by a quantitative interpretation of these results.

The fact that exact scaling as predicted by the naive parton model, does not hold was first shown in deep inelastic muon scattering experiments [**18**] at Fermilab. The qualitative nature of the scaling violation can be understood by realising that as Q^2 increases and the probing photon's wavelength shortens its resolving power increases. Hence, the quarks begin to be resolved into systems comprising quarks plus clouds of gluons and $q\bar{q}$ pairs, and so the probed proton's momentum is shared by more and more constituents as Q^2 increases. Thus each constituent must carry a smaller and smaller fraction of the hadron's momentum.

The QCD corrections to the basic quark parton scaling property have been calculated perturbatively by two groups [**19**] and lead to the prediction that the structure functions fall logarithmically with Q^2 for large $\varkappa$ and rise for small $\varkappa$. This behaviour can be seen in figure 2.1. Other types of scale breaking contributions to the structure functions are expected, which arise from final state interactions between the struck quark and other partons within the nucleus. However, these higher order twist contributions decrease like $\frac{1}{Q^2}$ and cannot be calculated perturbatively.

2.3 e^+e^- annihilation into hadrons

(a) The total cross section

A measurement of the total cross section for e^+e^- annihilation into hadrons, denoted by σ_{TOT}, provides another test of QCD. In the simple quark parton model, the two annihilating leptons produce a virtual photon which then creates $q\bar{q}$ pairs. These then decay with unit probability into hadronic final states.

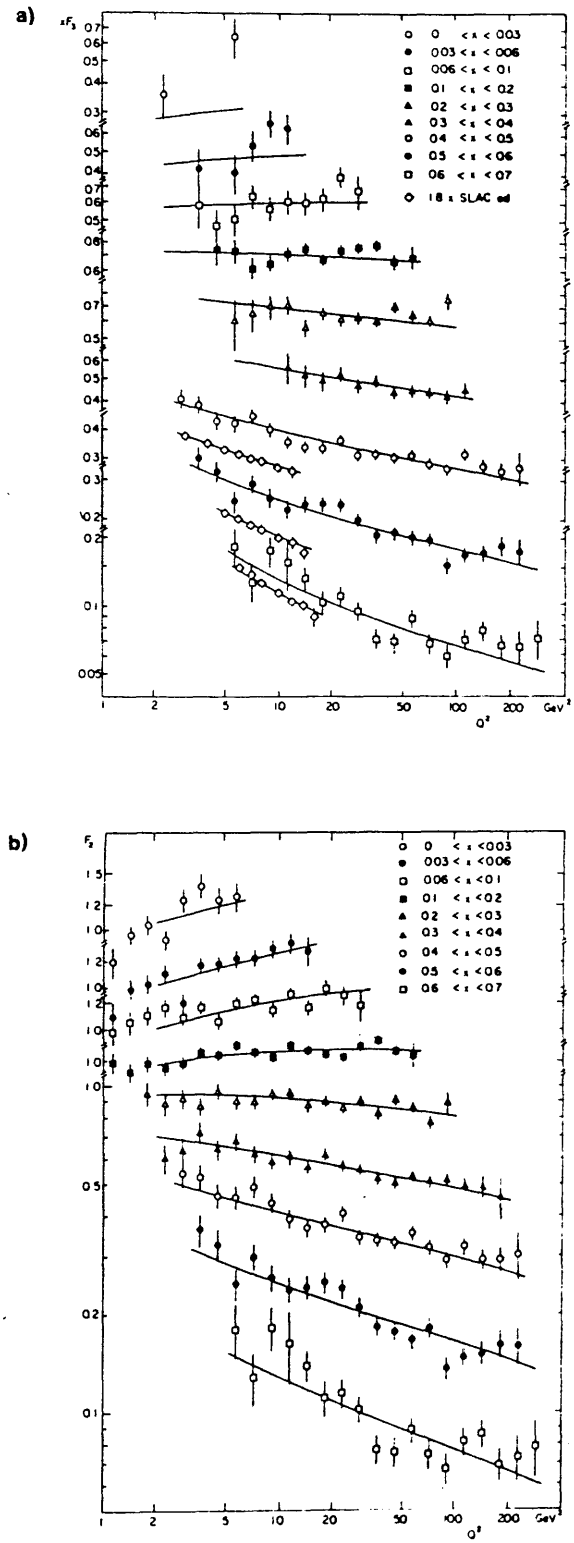

Figure 2.1 : The momentum dependence of the structure functions in each χ bin from lepton nucleon experiments [**17**] (a) structure function $xF_3(x, Q^2)$ (b) structure function $F_2(x, Q^2)$

It is usual to express σ_{TOT} in terms of the ratio,

$$R(e^+e^- \rightarrow \text{hadrons}) \equiv \frac{\sigma_{TOT}}{\sigma_{\mu\mu}} = 3\sum_q e_q^2$$

where $\sigma_{\mu\mu}$ is the lowest order QED cross section for muon pair production, and the sum 'q' is over all active quark flavours.

The experimental results for R are shown in figure 2.2, which shows clearly the transitions from regions where the u, d, s quarks are excited to the u, d, s, c and u, d, s, c, b regions. The value of R also shows that the number of colours is three and confirms the standard charge assignments.

In the context of QCD, R will be modified since gluon corrections need to be taken into account. These modify the $\gamma^* q\bar{q}$ vertex and the quark propagators, as shown in figure 1.6(b) to first order in α_S. Thus, to $O(\alpha_S^2)$ in QCD ,

$$R = 3\sum_q e_q^2 \left(1 + C_1\left(\frac{\alpha_S}{\pi}\right) + C_2\left(\frac{\alpha_S}{\pi}\right)^2\right)$$

where the quark masses are assumed to be zero. The perturbation coefficients have been computed up to second order by several groups of theorists, [**20**] with $C_1 = 1$. The coefficient, C_2, is dependent on the particular normalisation scheme that is used e.g.,

$$C_2 = 1.99 - 0.12N_f \qquad (\overline{ms}) \quad \text{scheme}$$

$$C_2 = -2.19 + 0.16N_f \qquad (mom) \quad \text{scheme}$$

(b) Observation of jets

The production of jets in e^+e^- annihilation through the process $e^+e^- \rightarrow q\bar{q}$ was first suggested in 1970 by Bjorken and Brodsky [**14**]. Jets were discovered experimentally at the e^+e^- storage ring SPEAR using the MARK-II detector of the SLAC-LBL collaboration [**21**]. This was done by defining the jet axis using sphericity, and then showing that the observed hadrons

had a limited transverse momentum with respect to this jet axis. The results of this analysis are shown in figure 2.3 and indicate the first evidence for jet formation in e^+e^- annihilation.

The measurement of the angular distribution of the jet axis with respect to the beam direction can also provide a test of the underlying quark structure of the jet. The distribution for the production of massless spin $\frac{1}{2}$ particles is

$$\frac{d\sigma}{dcos\Theta} \sim 1 + cos^2\Theta$$

which can be applied to $e^+e^- \rightarrow q\bar{q}$ for massless quarks. Figure 2.4 shows the data for the angular distribution of the sphericity axis with a fit of the form $1 + a \quad cos^2\Theta$.

(c) Three jet events

During the summer of 1979, when PETRA ran for the first time at a centre-of-mass energy above 27 GeV, the collaborations noticed hadronic events which did not consist of two back-to-back jets. These three jet events are explained by hard non-collinear gluon bremstrahlung $e^+e^- \rightarrow q\bar{q}g$. An example of such an event is shown in figure 2.5.

2.4 Monte Carlo hadronization models

At the present time, the production of hadrons from a parton final state is not calculable in QCD, and this has led to the use of phenomenological parameterizations of hadron production. There are, in general, two types of these models. The older models start with a configuration of partons, which has been generated by fixed order perturbation theory. Recently, fragmentation models have been introduced which use the leading-log approximation to evolve the partons.

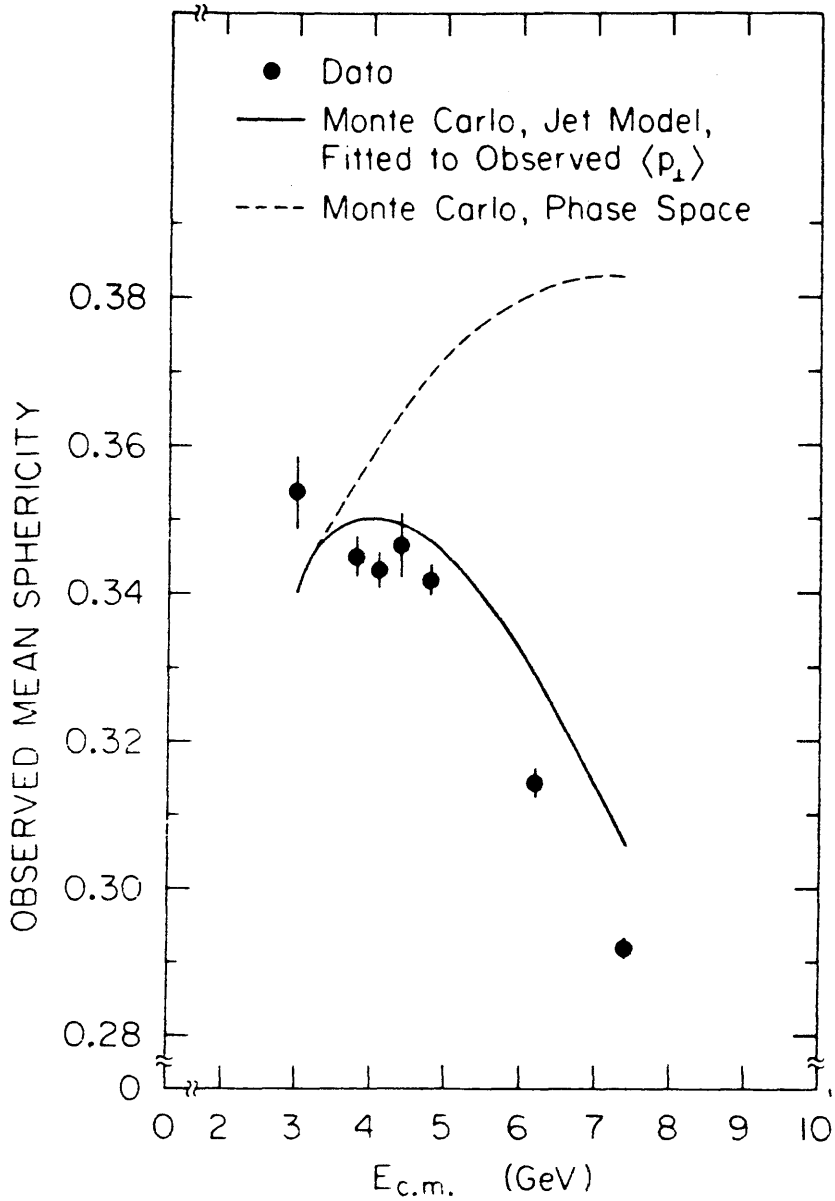

Figure 2.3 : The results of the MARK-II analysis showing evidence for the formation of jets in e^+e^- annihilation

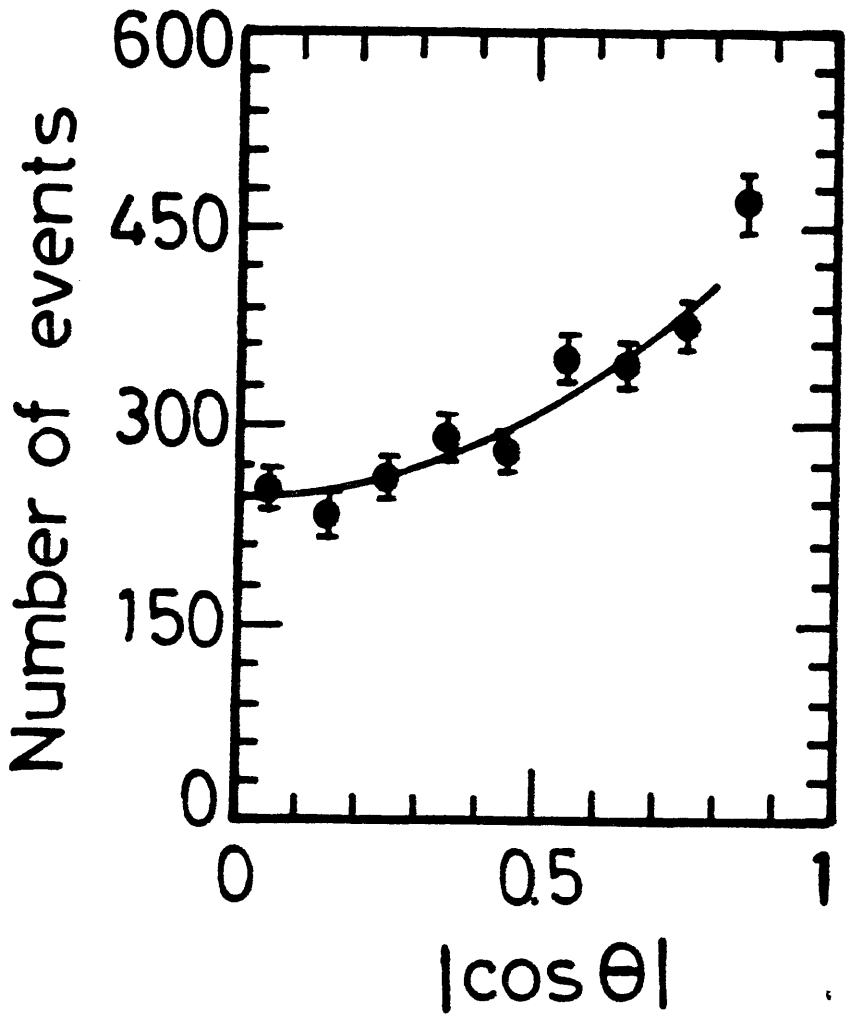

Figure 2.4 : Angular distribution of the sphericity axis with respect to the beam direction of the form $1 + 1.04cos^2\Theta$

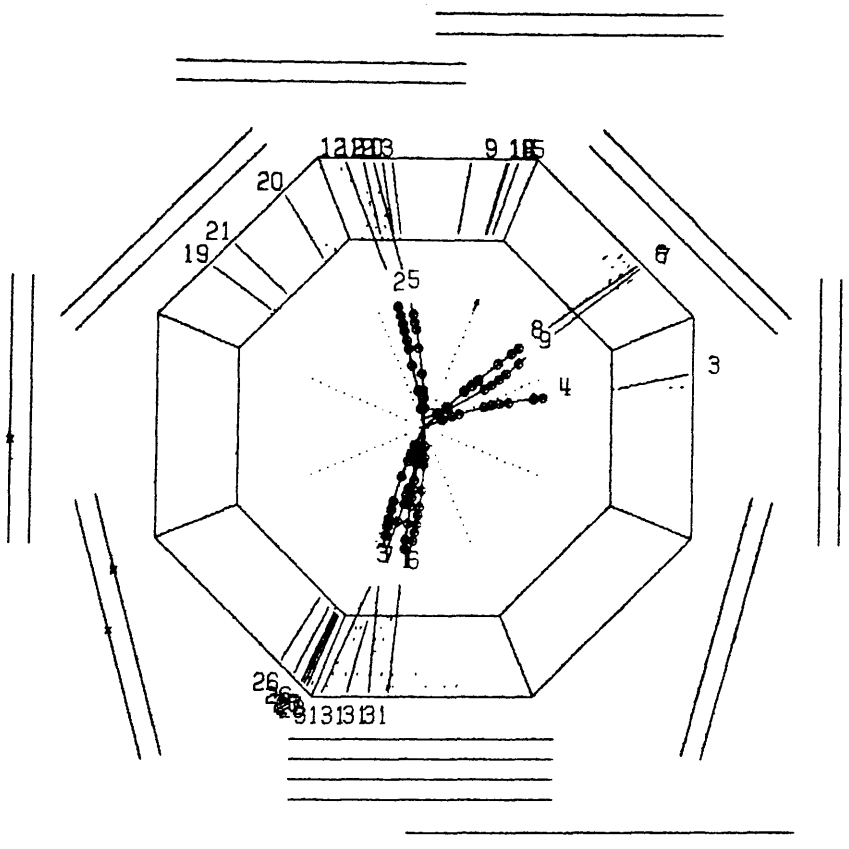

Figure 2.5 : An example of a three-jet event as found in the CELLO detector

The three most widely used models to describe the hadronization process are :

(1) the independent jet fragmentation model

(2) the string fragmentation model

(3) the cluster fragmentation model

The first two of the above models use fixed order QCD, whilst the third uses the leading-log approximation.

2.4.1 Independent jet model

This model was originally proposed by Feynman and Field [**22**] as a parameterization of hadron formation in jets, and takes into account two experimental facts :

(1) the hadrons have a limited transverse momenta with respect to the jet axis

(2) the energy distribution of the hadrons within a jet has an approximate scaling property.

Hadron production in quark jets is described in this model through the repetition of a basic transition,

$$Q_a \rightarrow M(Q_a\overline{Q}_b) + Q_b \qquad (2\text{–}1)$$

in which an initial quark fragments into a meson M and a residual quark Q_b. The creation of a $(Q_a\overline{Q}_b)$ pair from the vacuum can be thought of as producing this transition. Figure 2.6 shows the result of several iterations of the mechanism in equation (2-1), with the production of a chain of primary hadrons and a low energy leftover quark, which is then ignored if it has a low enough energy.

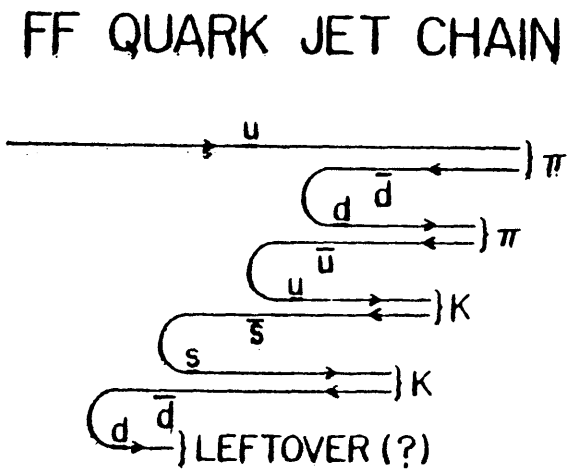

Figure 2.6 : Illustration of quark jet hadronization in the Field-Feynman model

The essential characteristics of this model are now described and four parameters, which are determined by fits to experimental results, are introduced.

The distribution of the transverse momentum, p_T, of the quarks created in this process is of the form,

$$\frac{d\sigma}{dp_T^2} \propto exp\left(\frac{-p_T^2}{2\sigma_q^2}\right)$$

where σ_q is the transverse momentum smearing parameter and is assumed to be independent of the incident quarks' energy.

In this model, all primary hadrons produced in the decay chain are assumed to be either vector or pseudoscalar mesons. The relative production rate is described by the ratio

$$R_M = \frac{N_V}{N_V + N_P}$$

The flavours of the quark pairs are allowed to be $(s\bar{s})$, $(u\bar{u})$ or $(d\bar{d})$ with $(u\bar{u})$ and $(d\bar{d})$ having an equal production probability. The relative amounts of each flavour is determined by the ratio

$$R_F = \frac{N(s\bar{s})}{N(u\bar{u}) + N(d\bar{d}) + N(s\bar{s})}$$

A phenomenological function $f(Z)$ is introduced to describe the fragmentation and is parameterized as

$$f(Z) = 1 - a + 3a(1 - Z)^2 \qquad (2\text{–}2)$$

with the variable Z being defined by

$$Z = \frac{(E + p_L)_{Meson}}{(E + p_L)_{Q_A}}$$

where p_L is the longitudinal momentum of the particle.

The following values of the four parameters provide a reasonable fit to experimental results

$$\sigma_q = 320MeV$$

$$R_M = 0.5$$

$$R_F = 0.4$$

$$a = 0.77$$

These values specify the standard Feynman-Field independent jet model and it should be noted that the values are assumed to be independent of the initial quarks' energy.

Several additions and modifications to this model are needed to describe gluon fragmentation and heavy quark production and fragmentation. The Ali [**23**] and Hoyer [**24**] models are the two most popular models which incorporate these extensions. In these models, the gluon is split into a quark- antiquark pair,

$$G \rightarrow Q(Z) + \overline{Q}(1-Z) \tag{2-3}$$

The quark and antiquark then fragment independently according to the Field-Feynman prescription. In the Hoyer model, the energy of the gluon is assigned with equal probability to either the q or $\bar{q}$. This has the effect that the gluons are treated as quarks of random flavour.

The Ali model distributes the energy sharing in equation (2-3) according to the Altarelli-Parisi splitting function

$$\frac{dP}{dZ} \sim Z^2 + (1-Z)^2$$

Since heavy quark production in e^+e^- annihilation is important, the Field-Feynman model needs to be modified to give a good description of heavy quark fragmentation, because it only contains u, d and s production up to this point.

This has been done by replacing the fragmentation function of equation (2-2) by the function,

$$f_H(Z) = \frac{1}{Z\left(1 - \frac{1}{Z} - \frac{\epsilon_H}{1-Z}\right)^2} \qquad (2\text{–}4)$$

in the method proposed by Peterson et al [**25**]. The parameter ϵ_H in equation (2-4) is estimated to be approximately equal to the square of the ratio of light to heavy quark masses, i.e., $\epsilon_H \simeq (\frac{m_l}{m_h})^2$. Typical values for this parameter are $\epsilon_c = 0.05$ for charm quarks and $\epsilon_b = 0.018$ for bottom quarks.

There are, however, several intrinsic problems with the Field-Feynman parameterization, some of which are described below.

Energy is not conserved in this scheme, since the splitting algorithm of equation (2-1) conserves the sum $(E + p_L)$, but neither E nor p_L separately. This leads to energy conservation being introduced in a somewhat arbitrary manner. In the Ali model, for example, the event is boosted and then rescaled in energy to restore energy conservation.

The scheme is also not Lorentz invariant, since the hadrons obtained by fragmenting a boosted quark are usually different from the hadrons that arise from Lorentz-boosting the products of the quark fragmentation. Charge, colour and flavour are not automatically conserved because of the soft quarks that remain at the ends of the decay chains. There is also the problem that in both the Hoyer and Ali models the fragmentation is not continuous across the boundaries for resolvable jet configurations.

2.4.2 String fragmentation model

This model, which is usually called the LUND model, was first proposed by Andersson et al [**26**], and is Lorentz invariant and implicitly conserves energy and momentum.

In this scheme, colour force lines are arranged in narrow tubes connecting a quark to an antiquark of opposite colour, as shown schematically in figure 2.7. Inside these tubes the energy density per unit length is approximately constant. This leads to the property of linear confinement since the energy needed to separate the quark- antiquark pair is proportional to the distance between them. When the distance between the quark and the antiquark becomes too great the flux tube is expected to break, through the production of a quark-antiquark pair. Thus, individual colourless subsystems are produced when the newly created quark and antiquark join with the original quark and antiquark.

The splitting of the colour tubes continues until the invariant mass , M, of the remaining $q\bar{q}$ subsystem is less than some cutoff value, M_0, which is typically a few GeV. This subsystem is split into two mesons through the generation of a quark-antiquark pair if $M \leq M_0$.

A potential problem with this picture is that the string hadronization scheme is not symmetric, i.e., a different result is obtained by starting the splitting process from the quark end than by proceeding in the opposite direction from the antiquark. However, in practice the LUND Monte Carlo produces a hadron at either the quark or antiquark end in a random manner.

In order to produce transverse momenta and to conserve energy in the total system the $q\bar{q}$ pair is formed over some finite length of the confining string and not at a point.

The probability of producing a massive $q\bar{q}$ pair in this model is assumed to be

$$\frac{dP}{dp_T^2} \sim exp(-cm_T^2)$$

where $m_T^2 = m_q^2 + p_T^2$, and c is a constant.

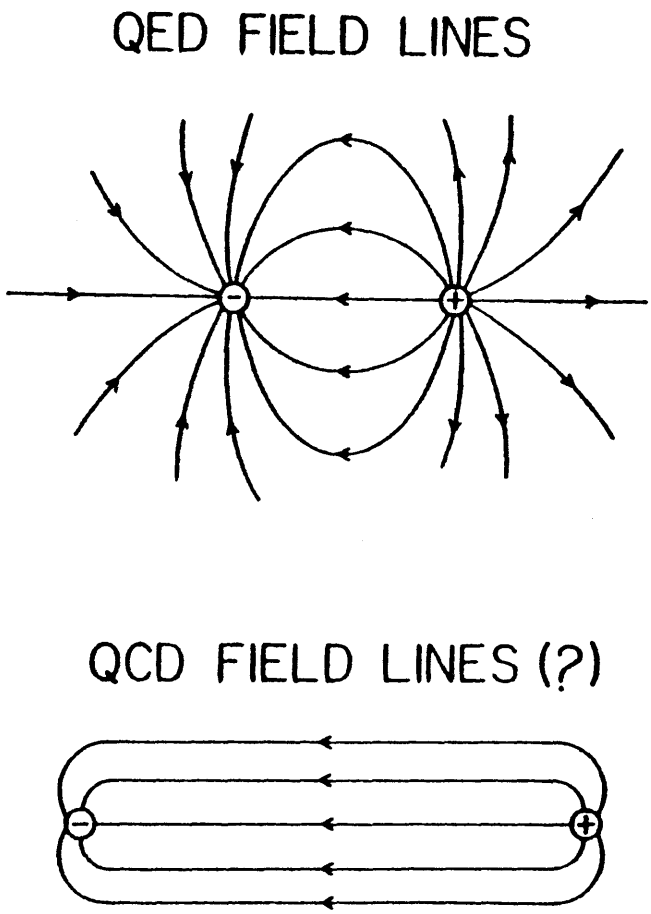

Figure 2.7 : A schematic representation of field lines between opposite charges in QED and QCD

This model uses a fragmentation function of the form

$$f(Z) = \frac{(1-Z)^a}{Z} exp(\frac{-bm_T^2}{Z})$$

with the constants a, b having the values 1 and 0.6 GeV^{-2} respectively.

In order to describe events with a hard perturbative gluon this picture needs to be modified. Thus, in an $e^+e^- \rightarrow q\bar{q}g$ event, the quark and antiquark are associated with the endpoints of the string and the gluon is represented as a kink on the string, which can carry energy and momentum. In an event of this type, the string is stretched from the quark to the antiquark via the gluon as shown in figure 2.8. This means that after fragmentation, the particles will lie along two hyperbolae as indicated schematically in figure 2.9. An important feature of the string model is that, unlike the independent jet model, the fragmentation of a $q\bar{q}g$ event approaches that of a $q\bar{q}$ event in a continuous fashion as the qg or $\bar{q}g$ invariant mass becomes smaller.

In summary, the basic conceptual difference between this model and the independent jet model is that instead of hadrons occurring from the independent fragmentation of isolated quarks they are created as a result of the interaction between a quark and an antiquark through a confining colour field.

2.4.3 Cluster fragmentation models

In these models, hadronization is described through the production and then decay of massive colourless objects called clusters. However, unlike the LUND string fragmentation scheme these cluster models do not require fragmentation functions. Hadron production from the decay of a collection of massive, colourless clusters is achieved through the use of a simple statistical phase space parameterization. This approach is based largely on the

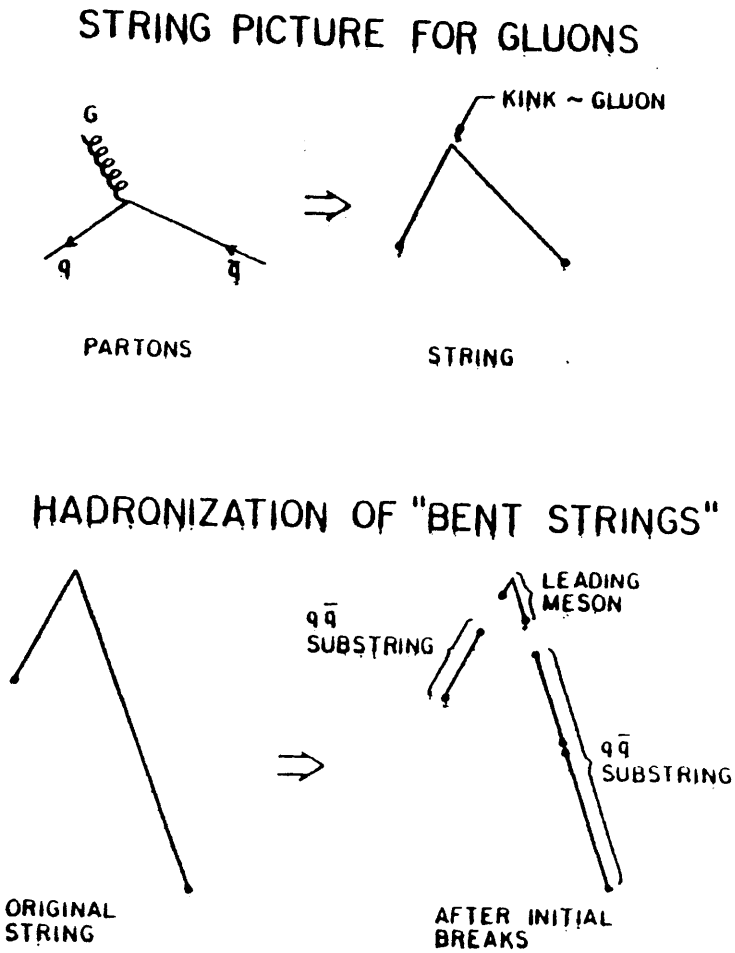

Figure 2.8 : The identification of a gluon with a kink in the string and the subsequent hadronization

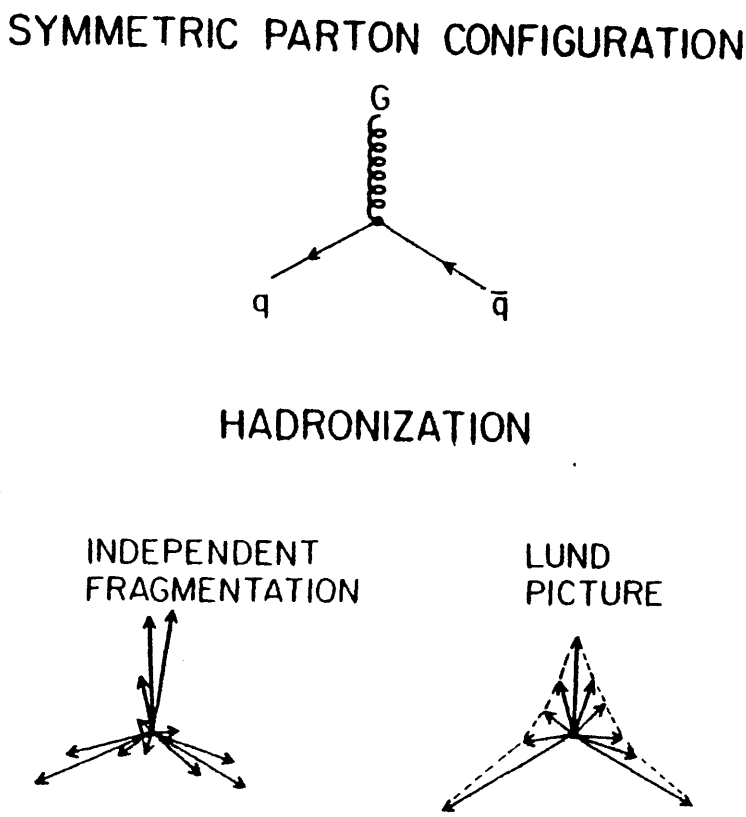

Figure 2.9 : The topologies for three-jet events expected in the independent fragmentation and LUND schemes

principle that colour separations must be screened before hadrons form. One example of a colour screening process is the radiation of a large number of perturbative gluons, which could produce a collection of low mass colourless clusters.

Field and Wolfram [**27**] proposed the first cluster model, which described the process $e^+e^- \rightarrow hadrons$ in three stages :

(1) A quark gluon shower is produced that conforms to leading-log perturbative QCD

(2) Clusters are formed through colour strings, which are associated with the initial shower

(3) Each cluster is hadronized independently using a simple phase space formula

A schematic representation of the structure of this model is given in figure 2.10.

A cluster decay into two primary hadrons H_1 and H_2 ,

$$C \rightarrow H_1 + H_2 \tag{2–5}$$

has a probability given by the product of three terms; a phase space term dependent on the cluster and hadron masses; a statistical factor based on the final state spins; and a flavour factor.

This cluster model has several problems, among which are a poor description of low mass hadronization and a large sensitivity to the treatment of soft gluons in the perturbative shower formation.

The Webber cluster model [**28**] tries to solve the latter problem by including soft perturbative singularities, associated with low energy gluon emission, in the shower formalism.

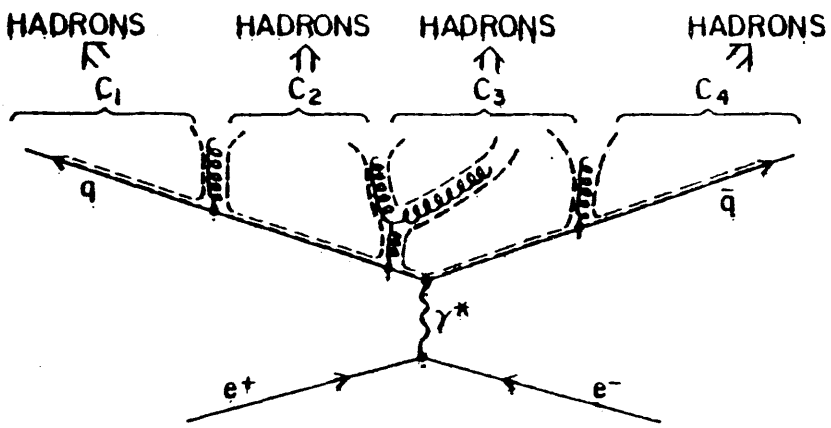

Figure 2.10 : The structure of the Field-Wolfram model, with the dashed lines indicating the strings

In the model of Gottschalk et al [**29**], the problem of describing low energy hadronization has been investigated by modifying equation (2-5) to allow the production of sublusters,C_i,

$$C \rightarrow H_1 + C_2$$

This modification leads to a better parameterization of the low energy data.

It should be noted that cluster models based on the leading log approximation do not contain the correct cross section for wide angle gluon radiation. This has the result that the three jet event rate is wrong e.g., for the Webber model this rate is half the observed experimental value.

2.5 Comparison of hadronization models

The three types of fragmentation model mentioned earlier have been extensively tested against the experimental data. In particular, the distribution of particles in three-jet events has been used for this purpose.

The first comparison between the LUND string fragmentation model and the independent fragmentation model was made by the JADE collaboration [**30**]. They selected planar three-jet events and then ordered the jets such that the first jet was opposite the smallest angle between the jet directions, and the third jet opposite the largest angle. It was found that the particle densities in the angular gaps between the jets were better reproduced by the LUND model. This finding was later confirmed in an extended analysis [**31**] using complete energy and particle flow distributions. The characteristic differences between the two fragmentation schemes can be seen clearly in the distributions of figure 2.11.

The conclusion that the independent fragmentation model does not provide a good description of the data has also been reached by the TPC collaboration [**32**]. In addition, they verified that the discrepancies between

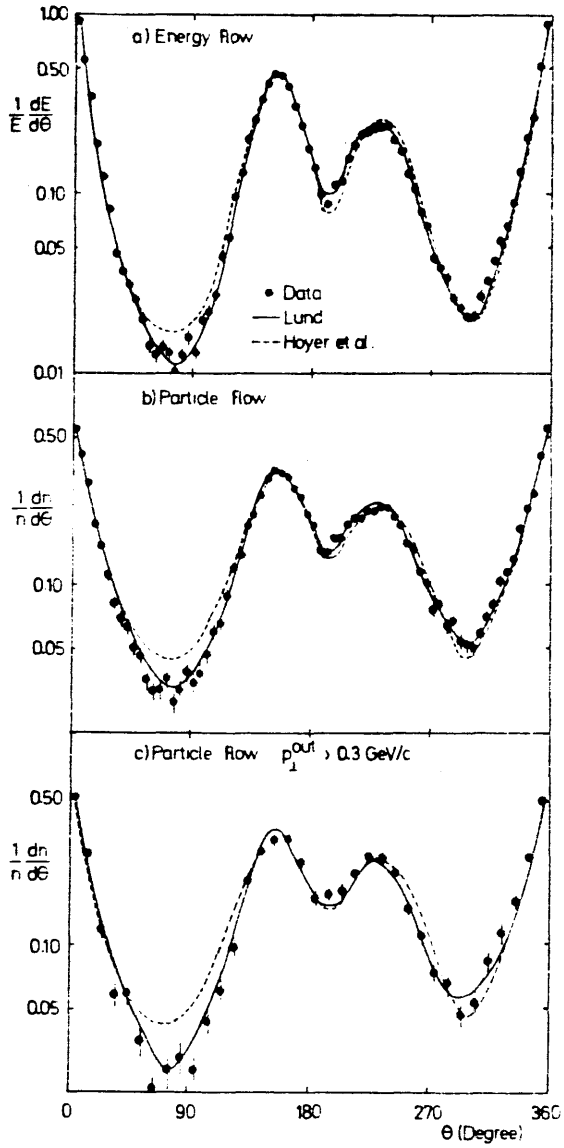

Figure 2.11 : The results of the JADE analysis comparing the LUND model and the independent jet fragmentation model with the data

the data and the independent fragmentation model were not a peculiarity of a particular model, by studying models with different energy-momentum conservation schemes. The results were also found not to be dependent on the tuning of the parameters used in the model. Thus the failure of the independent fragmentation model to describe the absolute three jet particle density is a fundamental characteristic of the model.

Recently, the TASSO collaboration [**33**] has found the same effect as JADE and TPC.

The cluster fragmentation model of Webber has also been investigated by both JADE [**34**] and TPC [**35**]. As has been mentioned earlier, the Webber model does not reproduce in detail the experimental data and in particular predicts fewer events with a three-jet structure than is observed. Hence, this model does not accurately describe the absolute particle densities between jets but, however, correctly predicts the ratios of these densities. This can be seen from figure 2.12, which shows the result of the JADE analysis.

2.6 Previous determinations of α_S

The general method that is used to determine α_S is to find an event measure which is sensitive to the production of gluons and then to fit a monte carlo to this, using α_S as one of the input parameters.

Initially, sensitive event measures could be divided into event shape measures and cluster techniques. The event shape measures were sensitive to the contribution of three jet events to the total cross-section and include such variables as thrust and sphericity, which are defined in chapter 1. The cluster technique was designed to calculate directly the ratio of three jet events to two jet events and hence determine α_S.

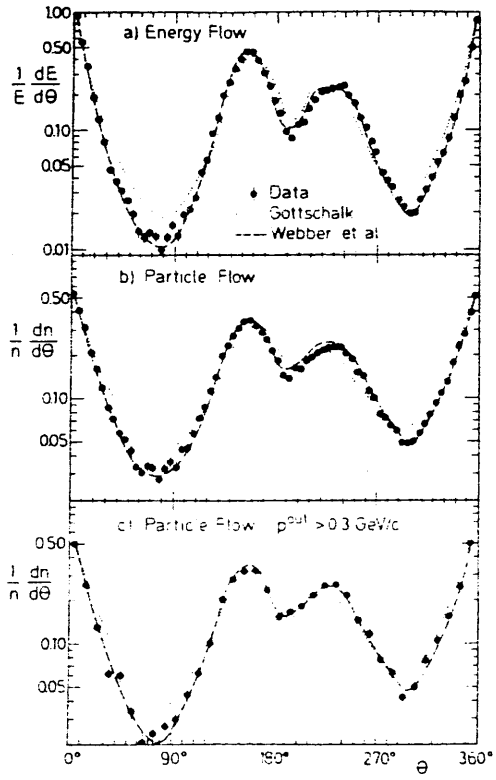

Figure 2.12 : The results of the JADE analysis comparing two cluster models with the data

There are several different methods of performing a cluster analysis but the one described here is the cluster search method of Daum et al [**36**], which is used by the PETRA experiments. Particles are first grouped into clusters, with a half-cone angle of typically $\sim 30°$, which are then ordered according to their energies. Low energy clusters are then grouped together and removed if their total energy is less than five percent of W, the centre of mass energy. The remaining clusters are kept only if their energy is greater than some cut-off energy, which is usually $\sim$ 2 GeV.

The first determinations of α_S from e^+e^- annihilation [**37**] were carried out in 1979/1980 and were based on a sample of approximately one thousand multihadrons per experiment at a centre of mass energy of W = 30 GeV. The results of these analyses are shown in table 2.1, which gives an average value at W = 30 GeV of

$$\alpha_S = 0.19 \pm 0.02 \pm 0.03 \qquad \text{in} \quad O(\alpha_S)$$

$$\alpha_S = 0.17 \pm 0.02 \pm 0.03 \qquad \text{in (incomplete)} \quad O(\alpha_S^2)$$

It should be noted that all these analyses used the independent jet model to describe the hadronization and either QCD formulae to leading order or the incomplete $O(\alpha_S^2)$ formulae based only on the four parton Born terms.

The first collaboration to investigate the sensitivity of the values of α_S to the hadronization scheme used was the CELLO group [**38**] in 1983. The study was based on $\sim$ 3000 hadronic events with the parton level cross section being calculated in first order QCD. The results of this study are shown in table 2.2 and indicate that the value of α_S is dependent on the fragmentation scheme involved.

However, the JADE group [**39**] using a sample of $\sim$ 4800 hadronic events found the value of α_S to be independent, within errors, of the fragmentation model used.

Group	QCD model	QCD correction	α_s
MARK J	Ali	incomplete $O(\alpha_s^2)$	$0.21 \pm 0.02 \pm 0.04$
TASSO	Hoyer	$O(\alpha_s)$	$0.19 \pm 0.02 \pm 0.03$
	Ali	incomplete $O(\alpha_s^2)$	$0.17 \pm 0.02 \pm 0.03$
JADE	Hoyer	$O(\alpha_s)$	$0.18 \pm 0.03 \pm 0.03$
PLUTO	Hoyer	$O(\alpha_s)$	$0.15 \pm 0.03 \pm 0.02$

Table 2.1 : Early determinations of α_S from the PETRA experiments. The first error is statistical, the second systematic

	TYPE OF FRAGMENTATION	
Distribution fitted	α_s independent	α_s string
fraction of events with $S > 0.25$, $A < 0.1$	0.19 ± 0.03	0.28 ± 0.045
fraction of events with $O > 0.2$	0.19 ± 0.02	0.26 ± 0.04
three cluster events	0.145 ± 0.02	0.235 ± 0.025
parton thrust x_1	0.155 ± 0.015	0.235 ± 0.025

Table 2.2 : Determination of α_S to leading order by the CELLO collaboration. The errors quoted above are statistical in nature.

Note:- The method of Daum et al. was used for the cluster analysis. The parton thrust x is defined as the normalised energy of the most energetic parton, i.e., $x_1 = \frac{2E_1}{W}$

They found,

$$\alpha_S = 0.20 \pm 0.015 \pm 0.03 \qquad \text{in} \quad O(\alpha_S)$$

$$\alpha_S = 0.16 \pm 0.015 \pm 0.03 \qquad \text{in} \quad O(\alpha_S^2)$$

The values of α_S found by these two groups are just compatible, within errors.

In 1984 the TASSO collaboration [**33**] published the results of an extensive investigation into the question of the fragmentation model dependence. The analysis was based on $\sim$ 16,000 hadronic events and the value of α_S was determined to both $O(\alpha_S)$ and $O(\alpha_S^2)$. The procedure that was followed was to use the published experimental inclusive cross sections on $\pi^+, \pi^0, K^+, K^0, \rho^0, K^\star, D^{\star +}, p, \Lambda \text{and} \Xi^-$ production to determine the various fragmentation parameters that occur within the fragmentation models. A simultaneous fit of α_S and these fragmentation parameters was then performed. The results support the view that the value of α_S is dependent on the fragmentation model. The average values from this analysis at W = 34 GeV are

$$\alpha_S = 0.16 \pm 0.015 \quad \text{for independent fragmentation}$$

$$\alpha_S = 0.21 \pm 0.015 \quad \text{for string fragmentation}$$

Energy-energy correlations and their related asymmetry have also been used to determine the value of α_S. The first two groups to use this method of determining α_S at a W of 34 GeV were CELLO [**40**] and MARK-J [**41**], the results of which are shown in table 2.3.

The CELLO collaboration found that their value of α_S depended strongly on the fragmentation model used in the Monte Carlo, whereas the MARK-J group only found a weak dependence of α_S upon the fragmentation model.

The findings of the CELLO collaboration were later confirmed by the JADE group [**42**] as can be seen from table 2.3. The variation in the value

	TYPE OF FRAGMENTATION	
GROUP	α_s independent	α_s string
CELLO	0.12 ± 0.02	0.19 ± 0.02
MARK J	0.12 ± 0.01	0.14 ± 0.01
JADE	$0.10 \rightarrow 0.15$	$0.165 \pm 0.01 \pm 0.01$

It should be noted in the above table that the treatment of errors is different in each case. The CELLO analysis only took statistical errors into account, whilst the MARK-J group added their systematic and statistical errors in quadrature. The JADE result is quoted with both a systematic and a statistical error.

Table 2.3 : Determination of α_S using the energy-energy correlation asymmetry

of α_S found by the JADE group when using the independent fragmentation models depended on the treatment of energy and momentum conservation and of the gluon splitting.

In a recent analysis, the MARK-J group [**43**] obtained the value

$$\alpha_S = 0.12 \pm 0.02$$

at a centre of mass energy of 44 GeV. This value is an average of the string and independent fragmentation models.

The sensitivity of the determination of α_S to the fragmentation model has recently been investigated by Sjostrand [**44**]. He confirmed the findings of the CELLO and TASSO analyses and suggested three reasons why the value of α_S depended on the fragmentation model :

(1) the methods used to correct for the non-conservation of energy and momentum which occurs in the independent jet models

(2) the procedure for fragmenting the gluons into hadrons

(3) the implementations of the QCD matrix element with particular regard to the parton resolvability criteria.

He found that the values of α_S obtained by fitting given data to the string model were systematically 40% higher than the values obtained using independent jet models.

This result can be understood qualitatively in terms of the different ways each model has of treating gluon fragmentation. In the independent jet models the momentum vectors of the jets reproduce, on average, the directions of the primary partons. This is not the case in the string model where the directions of the final hadron jets differ systematically from those of the original partons. The result of this is that the string scheme makes $q\bar{q}g$ events look more like two jet events since the particles lie along two

hyperbolae. Hence, the value of α_S in the string model needs to be higher to account for the observed number of three-jet events.

Therefore, it can be seen that all the previous determinations of α_S are subject to large systematic errors as a result of the wide range of possible fragmentation models. The approach of this study will be to try to eliminate this uncertainty by concentrating on the LUND string model. The reasons for this choice were given earlier in section 2.5. Thus, event shape measures and the energy energy correlation asymmetry will be used to determine α_S by fitting the LUND monte carlo to the corrected data. This analysis is presented in chapter 6.

CHAPTER THREE

THE CELLO DETECTOR

3.1 Introduction

The CELLO detector [45], a schematic diagram of which is shown in figure 3.1, has been operating at PETRA since March 1980 with a break between August 1981 and August 1982, when the PLUTO detector occupied the N.E. hall. A short description of the PETRA accelerator is now given, and then the essential details of the CELLO detector's operation are presented.

3.2 PETRA

The accelerator PETRA which is situated in DESY in Hamburg, W.Germany began producing collisions between electrons and positrons in September 1978. The basic structure of PETRA, as shown in figure 3.2, is that of eight straight sections and eight curved sections. The 2.3 km long pipe is evacuated to 5×10^{-9} Torr. Half of the straight sections are long, to house rf accelerating cavities, while the experiments are situated in the remaining four short straight sections. The identical curved sections contain quadrupole magnets, sextupole magnets and 5.5 meter bending magnets with a bending radius of 192 meters.

Production of positrons is achieved by directing electrons from a linear accelerator onto a target. These positrons are then accumulated in the small storage ring PIA (Positron Intensity Accumulator) and from there are fed into a larger storage ring DESY. Electrons are also injected into DESY from a linear accelerator (LINAC 1). DESY then accelerates the electrons and positrons to an energy of 6.5 GeV before they are transferred to PETRA.

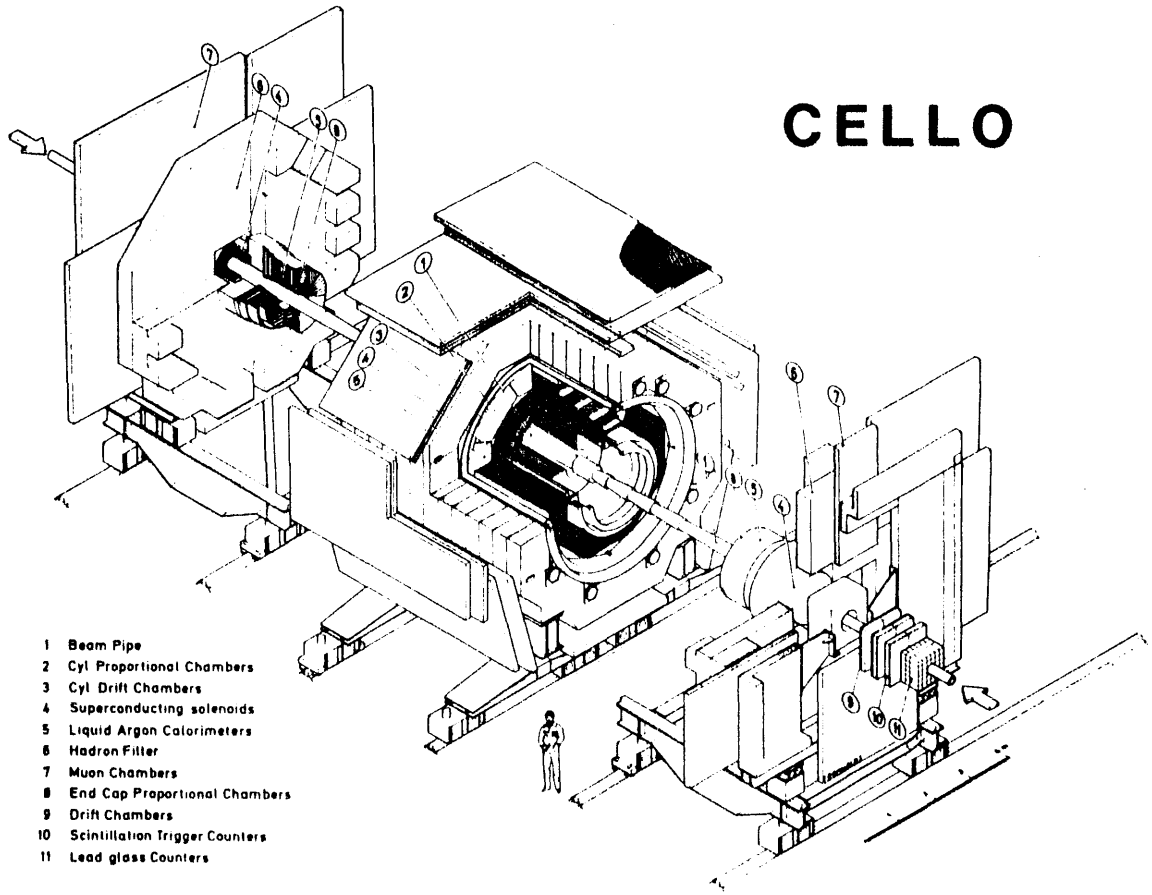

Figure 3.1 : Schematic diagram of the CELLO detector

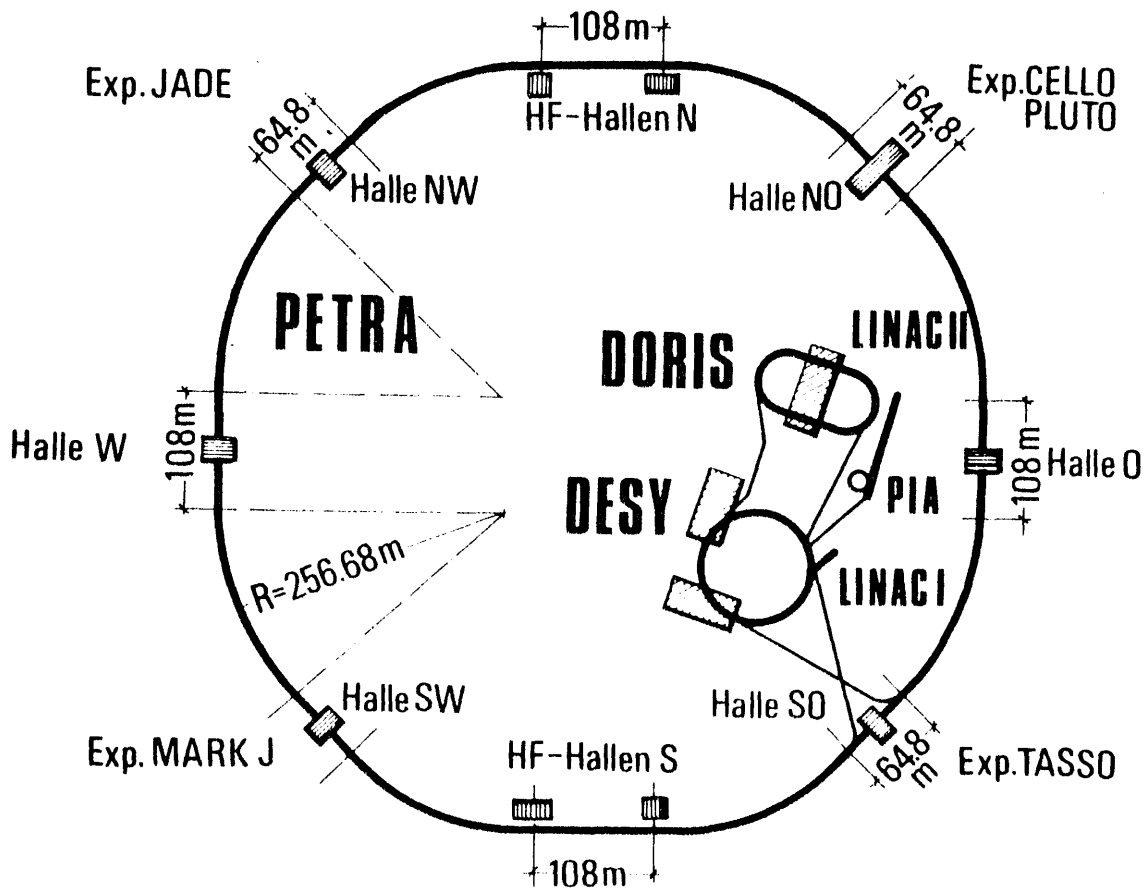

Figure 3.2 : Schematic diagram of PETRA

When the bunches of electrons and positrons are made to collide, head-on at the four experiments, they have been accelerated by the cavities in PETRA to an energy of around 20 GeV.

The event rate for a specific process can be calculated from the known cross-section, σ, and the luminosity, L, using the following formula;

$$\text{event rate} = \sigma \cdot L$$

An integrated luminosity of 200 nb^{-1} per day was achieved at a beam energy of 22 GeV. The total integrated luminosity used in this sample was 30 pb^{-1}. The mini-beta scheme, which was installed in March 1981, led to a gain in luminosity by a factor of three by reducing the space between the final focussing elements. This is achieved by removing the compensating magnets, which were thought to be necessary for solenoidal detectors, and using the three solenoidal detectors CELLO, JADE and TASSO to compensate each other.

3.3 The CELLO detector

The analysis of high energy e^+e^- collisions necessitates the detection of most of the leptons and hadrons produced in the interaction. This has led to CELLO having a large solid angle coverage and being optimized for electron and photon detection at the expense of extensive particle identification. The main features of the detector are now outlined, with the details of each detector component being presented in the subsequent sections.

The momentum of charged particles is measured over a solid angle of 97 % of 4 π steradians by a central tracking detector, which is enclosed in a superconducting solenoidal magnet of 1.3 T, and by a set of planar end cap drift chambers. A set of barrel and end cap lead liquid argon calorimeters outside the magnet coil allows the measurement of the energy

of photons and the identification of electrons over a solid angle of 96 % of 4 π steradians. The iron return yoke of the magnet acts as a hadron filter behind which muons are detected in planar proportional wire chambers with a solid angle coverage of 92 % of 4 π steradians. The angular range from 50 mrad to 100 mrad with respect to the beam axis is covered by forward detectors which are used to tag electrons in two photon collisions and to measure luminosity. Table 3.1 shows the important parameters of the various detector components.

3.4 Superconducting solenoid

The superconducting solenoid [**46**] is 4 m long and produces an axial field of 1.316 Tesla. The high current density superconducting coil of novel design has a wall thickness of only half a radiation length, including the cryostat and insulating material. This means that the detection of electrons and photons in the electromagnetic calorimeters is not seriously impaired.

3.5 Central tracking detector

The central detector [**47**] consists of five cylindrical proportional wire chambers arranged with seven drift chambers [**48**] concentrically around the beam axis with two layers of beampipe counters [**49**] to aid the vertex reconstruction (see figure 3.3). The detection of charged particles and a measurement of their momentum over a wide solid angle is possible. If at least 8 wire layers are used, then a solid angle coverage of 91 % of 4 π steradians can be achieved using the central tracking detector. The layer structure of the central tracking detector is shown in table 3.2.

The five proportional chambers each have axial anode wires and two cylindrical cathodes which are finely segmented in strips oriented at 90°

Detector Component	Constituent Parts	Solid Angular Coverage	Theta Range	Typical Dimensions	Properties and Resolutions (p_T, E in GeV)
Central Solenoid	—	—	—	length=4m radius=0.8m	superconducting, strength=1.316 T thickness=0.49 X°
Tracking Device	5 CPWC 7 CDC 2 BPC 4 ECPWC	99%	$8^\circ < \theta < 90^\circ$	length=2.2m radius=17-70cm radius=21-66cm	$\frac{\Delta p_T}{p_T} = 1.3\% \, p_T$ $\sigma_\theta = 3\text{mrad}/\sin$ $\sigma_\phi = 2\text{mrad}$
Electro-magnetic Calorimeter	16 LLACC 4 LLAEC	93%	$30^\circ < \theta < 90^\circ$ $8^\circ < \theta < 22^\circ$	length=2m depth=43cm width=85-121cm	$\sigma_\theta = 6\text{mrad}$ $\sigma_\phi = 4\text{mrad}$
Muon Chambers	30 MUCH	92%	—	surface area $7\text{m}^2 \rightarrow 12\text{m}^2$	$\sigma = 6\text{mm}$
Forward Detector	40 LGB 48 SC	0.4%	$50\text{mrad} < \theta < 100\text{mrad}$	—	$\frac{\Delta E}{E} = \frac{7\%}{\sqrt{E}}$
Hole Tagger	34 LSS	6%	$21^\circ < \theta < 30^\circ$	—	$\frac{\Delta E}{E} = \frac{65\%}{\sqrt{E}}$

KEY

CPWC : Central Proportional Wire Chambers
CDC : Central Drift Chambers
BPC : Beam Pipe Chambers
ECPWC : End Cap Proportional Wire Chambers
LLACC : Lead Liquid Argon Central Calorimeter Modules
LLAEC : Lead Liquid Argon End Cap Modulues
MUCH : Muon Chambers
LGB : Lead Glass Blocks
SC : Scintillators
LSS : Lead Scintillator Sandwiches

Table 3.1 : Properties of the CELLO detector

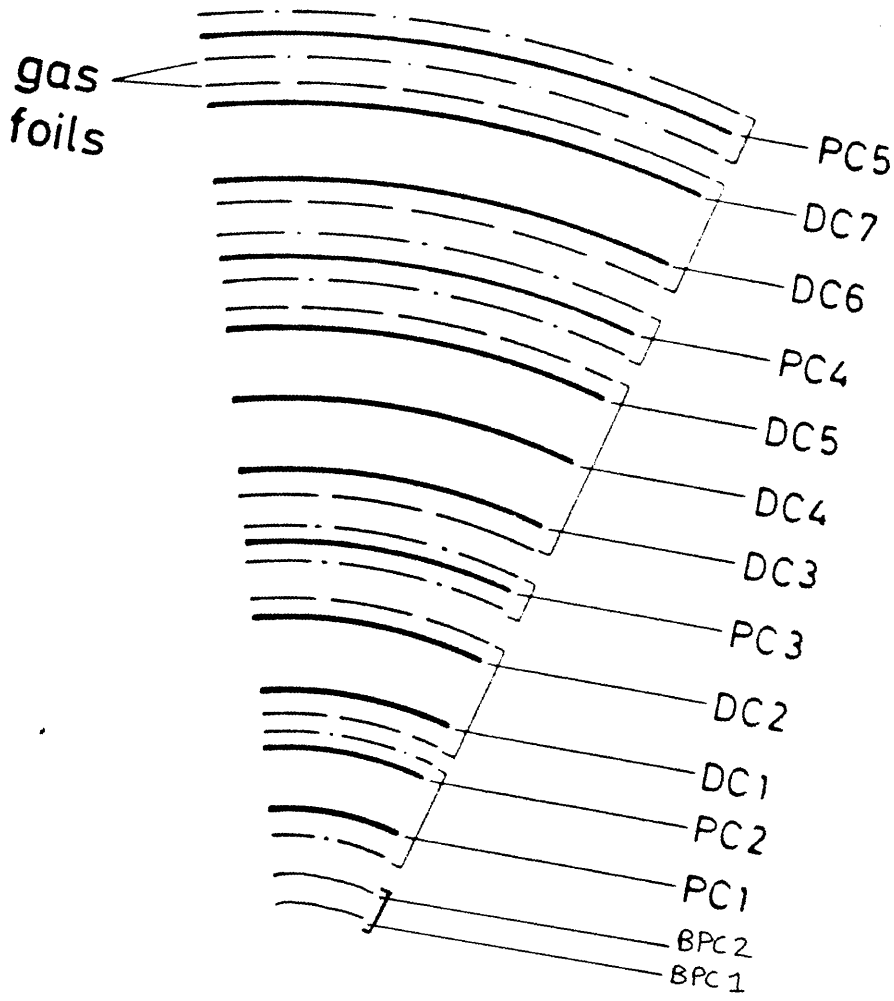

Figure 3.3 : Schematic diagram of central tracking detector

Layer Number	Chamber Type	Radius (cm)	Number of Anode wires, Drift Cells	Wire spacing, Drift cell width (mm)	Number of Cathodes 30	90
1	BPC	10.9	128	5.35	-	-
2	BPC	11.4	128	5.35	-	-
3	CPWC	17.0	512	2.09	256	252
4	CPWC	21.0	512	2.58	256	228
5	CDC	25.5	104	15.41	-	-
6	CDC	30.4	128	14.92	-	-
7	CPWC	35.7	1024	2.19	512	366
8	CDC	40.2	168	15.03	-	-
9	CDC	45.1	192	14.76	-	-
10	CDC	50.0	208	15.10	-	-
11	CPWC	55.3	1536	2.26	768	420
12	CDC	59.8	256	14.68	-	-
13	CDC	64.7	256	15.88	-	-
14	CPWC	70.0	1536	2.86	768	494

Table 3.2 : Layer structure of central tracking detector

and 30° with respect to the anodes. These cathode strips have analog readouts and give a very accurate Z determination. The charge correlation between the 90° and 30° cathode strips is used to separate overlapping cathode clusters from different tracks. All chambers have a wire length of 2.2 m with the anode wire layers being situated at radii between 17 and 70 cm thus giving a visible radial track length of 53 cm. There are 5120 anode wires each of diameter 20 μm with the anode wire spacing varying between 2.09 and 2.86 mm. The precision of the position determination in the longitudinal direction is on average $\sigma(z)$ =440 μm, whilst the spatial resolution averaged over all chambers is $\sigma(r\phi)$=0.24 $\times$ wire spacing.

The drift chambers enable a precise position measurement to be made in the plane of magnetic deflection (the $r\phi$ plane). The number of potential wires has been minimised by adopting an entirely open drift cell structure. A triplet of copper-beryllium potential wires separate adjacent gold plated tungsten sense wires electrostatically as can be seen from figure 3.4. In order to keep multiple Coulomb scattering as low as possible no futher field shaping electrodes were used. The required resolution of close tracks within jet events, which have a high local track density, led to small cell widths of about 15mm being used.

The electronics employed is of the single hit variety with an amplifier / discriminator hybrid mounted on the chamber, a TDC consisting of a low noise sample and hold amplifier and an 8-bit ADC which digitizes a maximum time interval of 810 ns. The chambers are filled with a gas mixture of 90 % Argon and 10 % Methane.

Systematic uncertainties such as wire displacement due to gravitational and electromagnetic forces, alignment errors and the quantization of time digitization (3.2ns) dominate the spatial accuracy of the chambers.

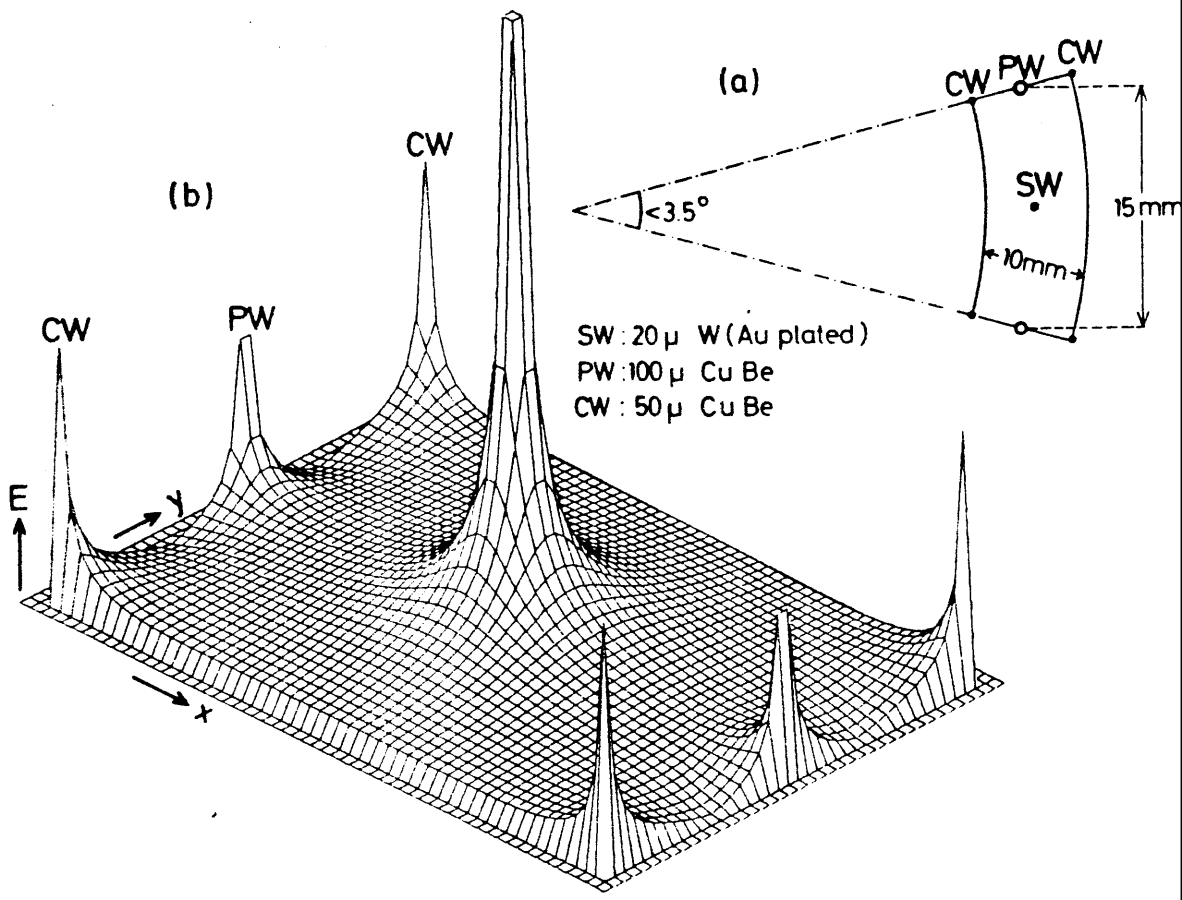

Figure 3.4 : (a) Drift cell geometry and (b) electric field distribution inside a drift cell

3.6 End cap proportional wire chambers

The CELLO detector has end cap multiwire proportional chambers placed at the ends of the cylindrical part of the central tracking detector. These chambers cover the acceptance region of $153 < \theta < 428$ mrad. Four identical planar units, which are semicircular in shape, make up this system. Two electrostatically separated chambers which are glued together at two of their cathode planes form each unit. One chamber of each unit measures the y coordinate, with wires parallel to the x axis, whilst the other chamber measures the x coordinate. One of the cathode planes of each chamber is divided into concentric rings about the beam pipe whereas the other cathode plane of each chamber is divided into sectors in ϕ of equal size $\frac{180^\circ}{32}$. The units are mounted on the front of the liquid argon end cap cryostats so that they form a circular disk perpendicular to the beam axis.

3.7 Lead liquid argon calorimeter

A barrel shaped lead liquid argon calorimeter [**50**] together with end cap calorimeters provides good electron-hadron separation and a good detection efficiency for low energy photons over 96 % of the solid angle. The central calorimeter consists of 16 stacks which have a trapezoidal cross section corresponding to a sector of an octagon. The stacks have a length of 2m, a depth of 43 cm and a width which varies from 85cm in the first layer to 121 cm in the last. The construction of the stacks is shown in figure 3.5. Continuous lead plates, which are 1.2mm thick, alternate with lead strips of equal thickness with a liquid argon gap of 3.6mm. The strips are maintained at a positive high voltage relative to the plates, and are oriented in three directions. There are thus strips at 0° to the beam axis, which measure phi; strips at 90° which measure theta and diagonal strips at 45°. The width

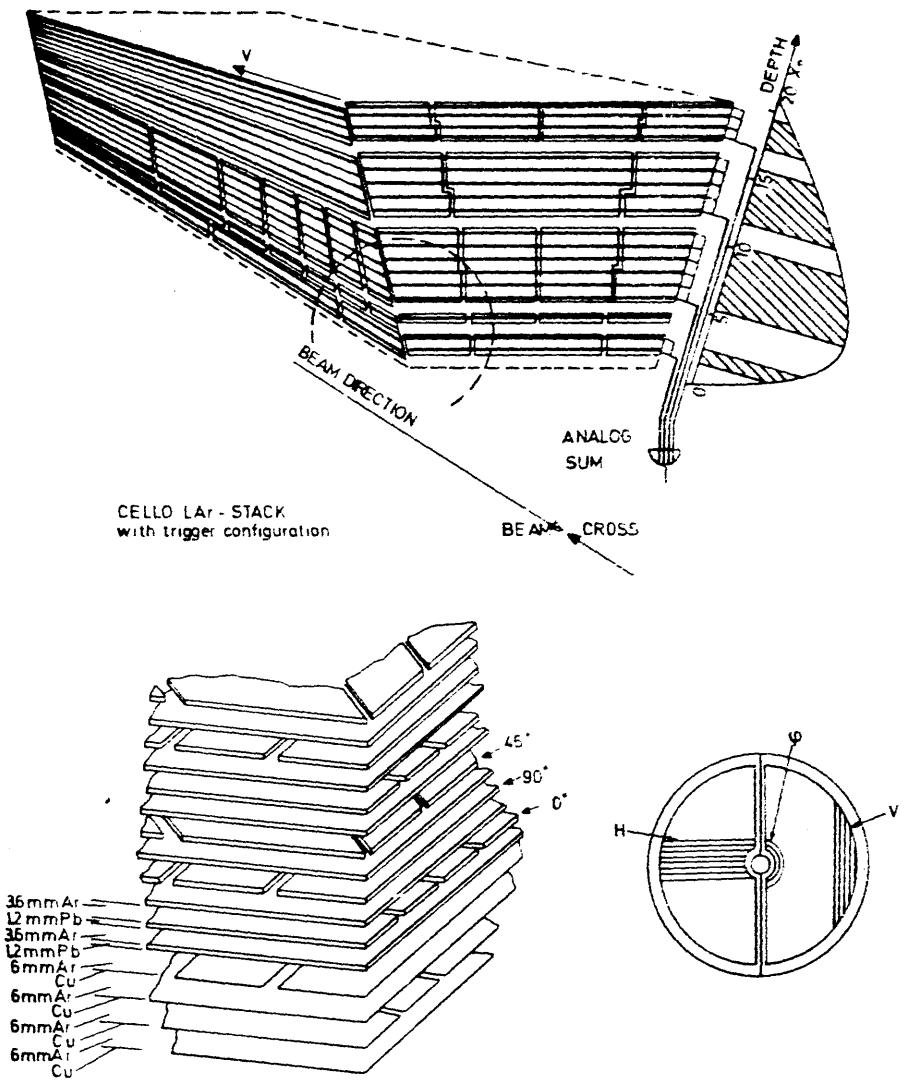

Figure 3.5 : Construction of the lead liquid argon calorimeter

of the strips which are oriented at 0° and 90° with respect to the beam axis, is 2.3 cm whereas the 45° strips are 3.25 cm wide. Two extra layers, consisting of copper foils glued on epoxy plates with an argon gap width of 6 mm, serve as $\frac{dE}{dX}$ gaps at the front of each stack. The lead modules are mainly supported from the rear to avoid structural material in front of the calorimeter and to minimize gaps between adjacent stacks. Thus, the overall dead area of the stacks is kept to less than 3.5 % of the total solid angle covered.

The number of electronic channels per stack is 576 and these are distributed between the three strip orientations as shown in table 3.3. Each stack is divided into seven layers which means that seven independent samplings in depth can be taken.

The end cap calorimeter consists of 42 layers of lead strips of thickness 1.2 mm interspersed with full plates of an identical thickness with an argon gap of 4 mm. Three planes of copper foils glued on epoxy in front of the lead calorimeter are used for $\frac{dE}{dX}$ measurement.

The analog signals from the 10688 electronic channels are processed by preamplifiers directly attached to the cryostat. The signals are transmitted to the main amplifiers and then digitized in a sample-and- hold circuit and a comparator. The final signals are organised on a readout card where channels with signals below a certain noise level can be suppressed. Minimum ionising particles can be safely detected since they deposit a charge which is approximately four times higher than the noise level.

3.8 Muon detector

The detection of muons is achieved using a hadronic filter and large proportional chambers [**51**] covering 92 % of the solid angle placed on the

Layer Number	Number of Electronic Channels 0°	45°	90°	Total Number of Channels	Thickness (X_0)
1	32	-	48	80	0.5
2	32	40	64	136	2.5
3	32	48	56	136	1.5
4	16	-	24	40	2.0
5	16	48	24	88	4.5
6	16	12	12	40	5.5
7	32	12	12	56	4.5
Total	176	160	240	576	21.0

Table 3.3 : Distribution of electronic channels in one module of the central calorimeter

outside of the detector. The iron return yoke of the magnet, which is 80 cm thick, is used as a hadronic filter and represents 5-8 absorption lengths for the hadrons. Multiple scattering of the muons in the lead liquid argon calorimeter and in the iron filter means that a higher precision than $\pm$ 9mm serves no useful purpose. The chambers have a drift cell structure but are read out as proportional chambers. The construction of the chambers is shown in figures 3.6 and 3.7.

Each chamber has a sense wire plane between two cathode strip planes with a gap of 8 mm. The wire plane consists of drift cells which have a 20 micron sense wire placed 6 mm from two 100 micron field wires. The cathode strips, which have a width of 10.6 mm and a separation of 2 mm are composed of flexible printed circuit (35 microns of copper on a 75 micron mylar sheet). The strips are glued onto a honeycomb structure which is 6 cm thick. The angle between the anode wires and the cathode strips is $34°16'$. The two cathode strip planes and the anode wires make it possible to reconstruct a hit in the chamber without any ambiguity. This arrangement gives a precision of 6 mm in the measurement of the position of an incident particle, which is less than the spread of a few centimetres caused by the iron filter.

3.9 Forward detector

This detector [**52**] is used to identify and measure electrons travelling at small angles with respect to the beam axis and thus to monitor the luminosity based on bhabha events and to help analyse two photon events. Small drift chambers, scintillators and lead glass blocks comprise the detector which has to tolerate a high background from synchroton radiation and beam gas interactions.

Situated nearest to the interaction point are three groups of two planar

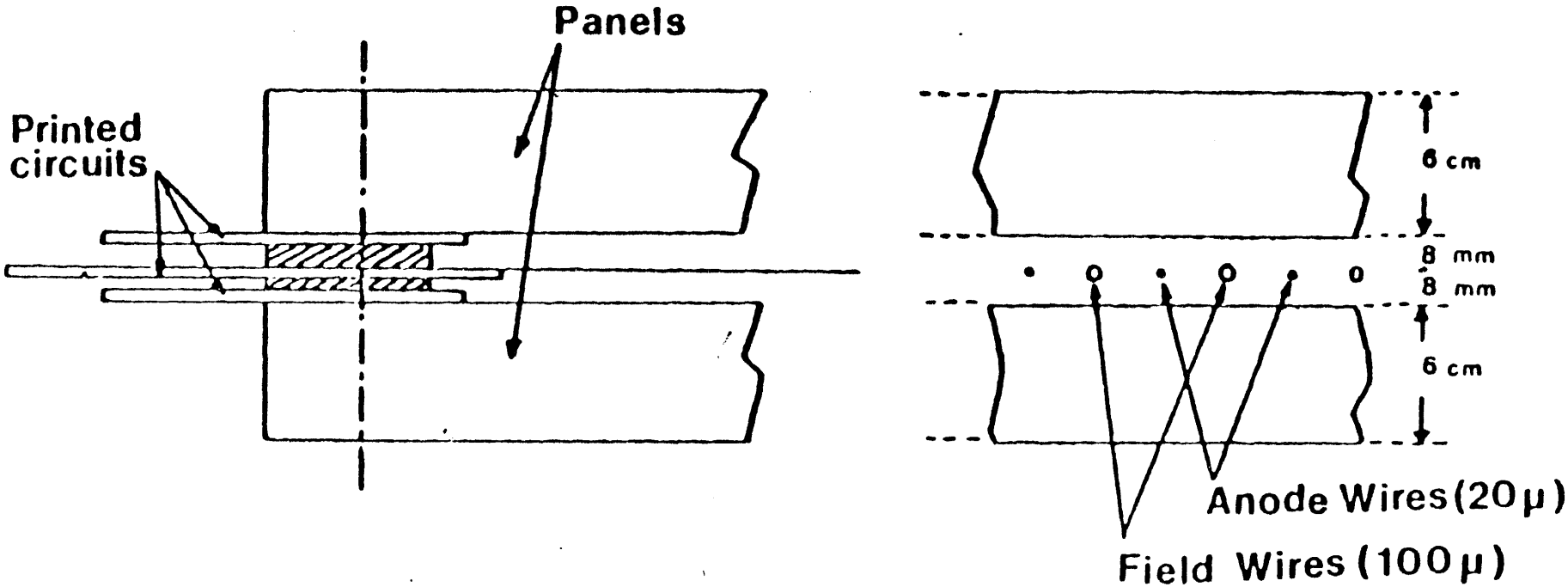

Figure 3.6 : Construction of the muon chambers

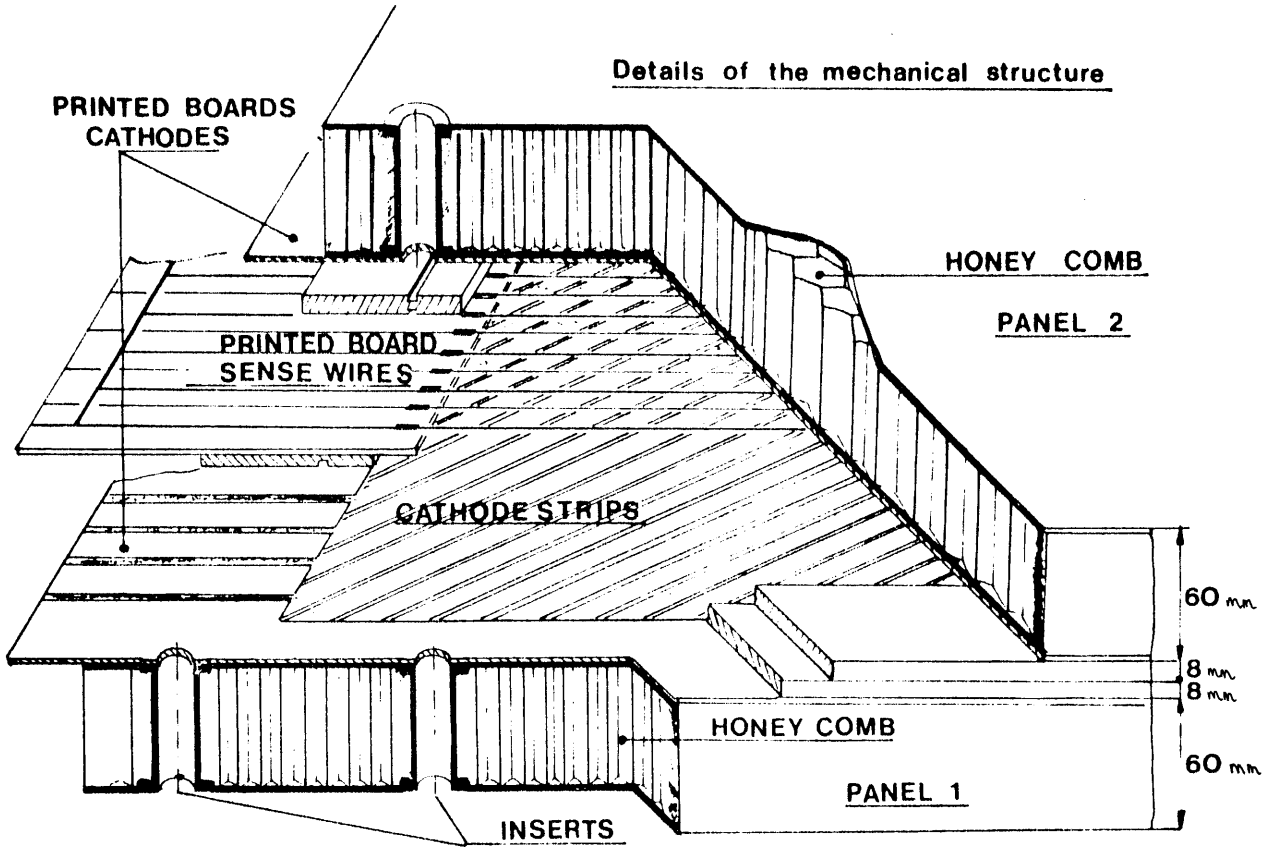

Figure 3.7 : Detailed construction of a muon chamber

drift chambers, with large scintillators covering the first and third group and two planes of finger scintillators in the middle group. Behind the arrangement of drift chambers is a lead glass shower counter which has 3 vertical, 3 horizontal and 4 longitudinal blocks of thickness 3, 3 and 14 radiation lenghts respectively. The energy resolution of the lead glass calorimeter is

$$\frac{\sigma(E)}{E} = \frac{0.05}{\sqrt{E}}$$

with E in GeV, and the spatial resolution of the drift chambers is 300 μm. The detector covers the polar angular range from 50 to 100 mrad.

3.10 The trigger

The trigger system [**53**] is used to keep the data acquisition rate at a low enough level for the computers to manage, by distinguishing the interesting events from noise caused by synchrotron radiation and beam gas and beam wall interactions. Charged particle triggers from the tracking device and energy triggers from the lead liquid argon calorimeters and the forward detector lead glass counters make up the system. Various combinations of these triggers can be chosen using an online computer.

3.10.1 Charged particle trigger

This device is a software programmable hardware track finding processor which acts in less than 1.5 μs on the chamber signals after each bunch crossing. It uses information from the anodes and 90° cathodes of the proportional chambers and from two of the drift chambers. This information is grouped in 64 azimuthal ($r\phi$) and 37 polar (rz) sectors which allows masks of various sector combinations to be defined. The masks are chosen so that curved charged tracks (in the $r\phi$ projection) have to have a transverse momentum of more than 350 MeV/c and straight tracks (in the rz projection)

are found close to the interaction point. Possible chamber inefficiencies can be avoided by using different masks which require five, six or seven chambers out of a possible seven to be fired. The trigger condition that was usually used for charged tracks was $r\phi$ ($\geq$ 2 sectors)$\cdot$ rz ($\geq$ 1 sector). Another condition which is less stringent on the central detector is $r\phi$ ($\geq$ 1 sector)$\cdot$ rz ($\geq$ 1 sector). and is used for combined triggers with the liquid argon and forward detector

3.10.2 Neutral particle trigger

Information on the energy deposition in the cylindrical or end cap liquid argon modules is utilised by this trigger. Three energy sums are made for each module (see table 3.4) :-

sum$A$ this covers the region between 1 - 17 X^0 and is essentially a sum of the calorimeter energy.

sum$B$ this covers the region between 3.5 - 7 X^0 and measures the electromagnetic energy at the position of its maximum.

sum$C$ this covers the region between 1 - 7 X^0 and measures the electromagnetic energy with different electronic channels from those used in sum$B$.

From these three sums four discriminator thresholds are formed : SAL (sum$A$, low threshold), SAH (sum$A$, high threshold), SB and SC. Out of these logical signals the following triggers are formed :-

$LA1$ a one module trigger.

$LA2$ two modules which are non-adjacent in ϕ.

$LA3$ one module as coincidence with other triggers such as $r\phi(1)\cdot rz(1)$.

Layer Number	Orientations used for trigger sums sum A	sum B	sum C
1	-	-	-
2	32 0°	-	32 0°
3	-	32 0°	-
4	16 0°	24 90°	16 0°
5	16 0°	-	-
6	16 0°	-	-
7	-	-	-
Total	80	56	48

Table 3.4 : Electronic channels used to calculate trigger sums

This liquid argon calorimeter trigger allows a precise measurement of Bhabha scattering (without using any track information) and gamma pair production.

3.11 Hole tagger

This is a device [**54**] which is designed to cover the gap in acceptance of the lead liquid argon calorimeter between the central region and the end caps. It consists of 2 cm of lead sandwiched between two 1 cm thick scintillators.

CHAPTER FOUR

DATA ACQUISITION AND EVENT SELECTION

4.1 Introduction

In e^+e^- annihilation experiments, many background events occur in addition to the interesting physics events. These background events can originate from several processes, such as the interaction of the electron or positron with a residual gas molecule in the vacuum pipe (called a beam gas event) or the interaction of one of the beams with the material of the beam pipe wall (called a beam wall event). Spurious events can also be caused by cosmic rays passing through the detector and interacting with the residual gas in the beam pipe. Electronic noise generated by some of the various pre-amplifiers and amplifiers can cause detector components to trigger prematurely and so produce events that need not be further analysed. The online data acquisition system and the offline filter programs are designed to separate the background processes from the events that originate from the fundamental forces under study.

This selection procedure, from the initial data acquisition to the final sample of events, is now described. The main features of the data acquisition system are shown in figure 4.1.

4.2 Data acquisition system

The detected signals from the different components of the detector are read by a CAMAC [**55**] system and several dedicated computers monitor the performance of the detector and ensure that the collected data is transferred smoothly to the DESY computer centre.

The CAMAC modules are arranged in ROMULUS branches, with each

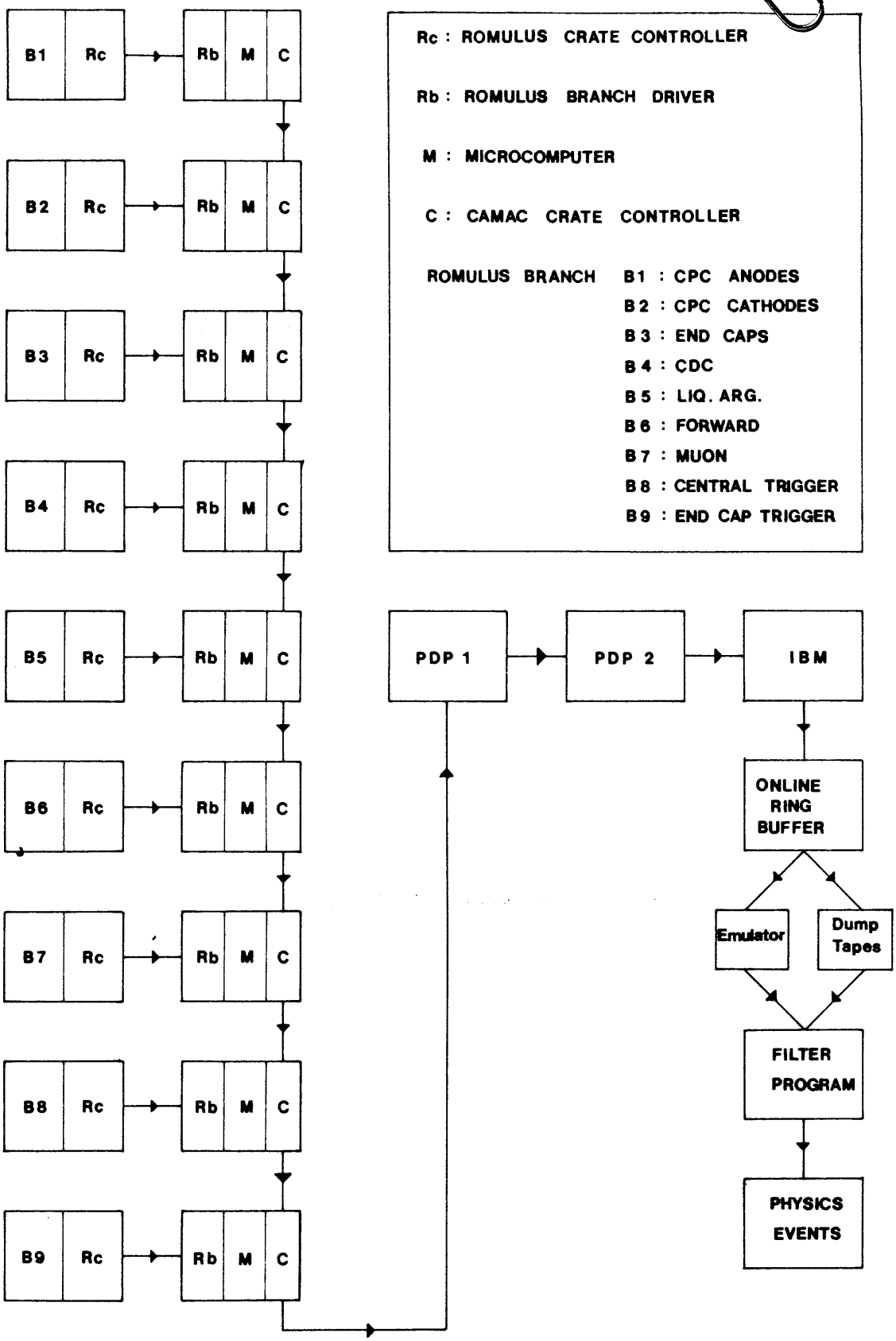

Figure 4.1 : Schematic representation of the data acquisition system showing the hardware configuration and the data flow diagram

branch corresponding to a detector component. After each beam crossing, a logic programmable TRIGGER verifies that the signals are compatible with an event occurring at the interaction point. This process produces a data acquisition rate of 2 or 3 events per second, that is, one event every 100 000 beam crossings.

As described in the previous chapter, the trigger performs a fast pattern recognition, using the momentum measurements of charged particle tracks in the central detector and the energy deposited in the calorimeter modules. The most important trigger requirement relevant to this study has been that:

(a) there be at least one charged track in the inner central tracking detector in coincidence with an energy deposition of at least 1.5 GeV in any of the sixteen lead liquid argon calorimeter modules.

Two other triggers that have been used are:

(b) a trigger that requires at least two charged tracks in the central detector with a transverse momentum with respect to the beam axis such that $p_T > 200 MeV/c$. At beam energies greater than 19 GeV, the background conditions became worse, and so a tighter trigger requirement had to be made. Thus, at the highest running energies, there had to be a minimum opening angle between any two tracks of 135° and the p_T condition became $p_T > 650 MeV/c$

(c) a trigger that requires at least 1.5 to 4 GeV shower energy deposited in any of the sixteen modules. The choice of the energy level depended on the background conditions.

Once the trigger has indicated a possible interesting event, a first computer, the PDP1, examined the signals from the various CAMAC branches and made an initial selection from the reconstruction of tracks in the cen-

tral detector. This procedure, which is described in detail in section 4.4, eliminates 50 % of the events and the remainder were passed onto a second computer, the PDP2. This computer controls the data acquisition by starting and finishing data taking through means of a touch panel and also provides rapid information on the status of the various detector components through histograms. The PDP2 also performs an initial selection of bhabha events and multihadronic events, in order to obtain a quick determination of the ratio R. This fast calculation was intended to provide an early indication of the existence of a sixth quark when PETRA was running at a series of centre-of-mass energies. The events are then transmitted to the DESY computer centre, where an IBM computer stores the events on a disk file, which is organised as a large ring buffer. A DUMP job is run automatically to transfer the data onto an RDT (Raw Data Tape), when the space in the buffer is nearly exhausted.

The second stage in the data processing chain uses the RDT, which contains the signal information from each part of the detector. An event filter now acts on the RDT and rejects about 90 % of the events. This is achieved through reconstructing charged tracks in the central detector and calculating the energy deposited in the liquid argon calorimeter.

4.3 Use of the emulator

The above procedure for filtering the data was used for the first half of the time in which the data used in this study was collected. In the second half of the relevant data-taking period, neither PDP1 nor PDP2 performed any filtering, although PDP2 still made a fast selection of bhabhas and multihadrons. This was because a new component was introduced into the data acquisition chain, a 370/E emulator [**56**], which examined the events on the IBM online disk by running them through the filter program.

The 370/E emulates an IBM 370/168 mainframe computer and can process 1 megabyte sized programs with a speed which is a quarter that of an IBM 3081 D mainframe. The advantage of this emulator over the earlier 168/E, as used at SLAC, is that its architecture is similar to the IBM architecture. The data and instructions are stored in a combined memory and there is direct emulation of the IBM instructions. This means that the programs do not need to be translated before they are run on the emulator, thus leading to simpler operation. The filter program is linked with the 370/E system and the FORTRAN I/O routines and then downloaded.

The main advantage of running the filter program on the emulator are that it saves running time on the IBM mainframe computer at DESY and the computers at the other collaborating institutions, and hence cuts computing costs.

The emulator acts on the IBM online disk and is supposed to analyse every event that is triggered. This is not possible, however, if the trigger rate becomes too high since the emulator does not have enough time to process the events. An identical filter program to that used on the emulator is run offline on the events which have not been analysed by the emulator. Typically, the emulator processes around 60 % of the events. The basic purpose of the emulator is to designate events as GOOD or BAD. The offline filter program analyses the remaining 40 % of events, then throws away the BAD events after checking that the emulator is working correctly.

The general procedure for flagging events is outlined below.

4.4 Filter program

The filter program uses three main groups of event data :

(1) the coordinates of hits in the inner detector wire chambers

(2) the total energy deposited in the liquid argon calorimeter

(3) the coordinates of single channels in the central liquid argon calorimeter that indicate an energy deposition

The first step in the program is to decode the raw data into a simple format and equate the data with the appropriate detector component. The wire chamber coordinates are then calculated for the inner detector in the $r-\phi$ projection, along with the corresponding z coordinates. The calculation of the z coordinates begins by employing a clustering algorithm on the cathode strips, with this operation being performed separately for the 30° and 90° strips of each proportional chamber. The lower and upper values of z can then be calculated for each cluster, and from this information, the program looks for overlaps between the 30° and 90° clusters for a given ϕ - coordinate. The z coordinate is then determined if the overlap is greater than some specified value. The program then tries to reconstruct tracks which can be forced through the point $r = 0$ (assumed to be the interaction point). The track must have at least nine points on it, and these two conditions mean that beam-wall events and cosmics are often not reconstructed. The track recognition in the $r - z$ projection is performed in a similar manner, but with the required number of points on the track reduced to four. If at least two tracks are found in the $r - \phi$ projection, a track opening angle, $\Delta(\phi_0)$, is calculated, which is the maximum of all opening angles between any two tracks.

The energy deposited in each stack of the liquid argon calorimeter is calculated from the sum of the ADC counts, which is converted into an energy by a set of calibration constants. The stack energies are then classified into various energy levels according to table 4.1, and an energy

CLASS	LEVEL L_E	ENERGY RANGE
junk	-1	$E_s \leq$ -800 MeV
zero	0	-800 MeV $< E_s \leq$ 800 MeV
low	1	800 MeV $< E_s \leq$ 1500 MeV
medium	2	1500 MeV $< E_s \leq$ 2000 MeV
high	3	2000 MeV $< E_s$

Table 4.1 : The classification of the total energy deposited in a stack of the lead liquid argon calorimeter

spread parameter, S_E, is calculated

$$S_E = \max_{i,j} \Omega_{ij} \times (L_i + L_j)$$

where Ω_{ij} is the opening angle between any two stacks i and j, and L_i, L_j are their respective energy levels. The opening angle between the two stacks that maximise S_E is called Θ_S. A bhabha event, for example has values for S_E and Θ_S of 6π and π respectively. A stack is designated "in time" if the timing of the energy sums occurs within 300 nsec of the interaction time. The last stage of the filter program is to try to find clusters in the liquid argon stack projections u, v, w and then to merge them.

The filter criteria are defined by strings of numbers of basic conditions, which all have to be fulfilled. Two types of string are used: ACC strings to accept events for which the conditions are true and REJ strings to reject events if the conditions are true. A condition is inverted if its negative number is written into the string.

Thus, the decision process proceeds as follows. The reconstruction in $r - \phi$, the liquid argon energy sums and the timing calculations are carried out first. The events are then examined to see if they pass a number of strings of conditions. An example of a set of these strings is given in table 4.2. The events that fail this initial selection are marked BAD and are not further processed. The reconstruction in $r - z$ is then done for the GOOD events, which will for some events change their event parameters. Hence, when the events are passed through the series of condition strings, some will fail and are marked BAD. The remaining GOOD events have their liquid argon clusters reconstructed and are checked for the last time against the selection criteria.

The filter program also checks that the trigger conditions are consistent, i.e., a particular trigger is accepting events with the specified properties.

Criteria Banks	Basic Conditions and Explanation				
$ACC 0 /	4 $N_{tracks} \geq 4$	13 $\Delta(\phi_0) > \frac{2\pi}{8}$	118 $\|\Sigma q\| < N_{tracks}$		
$ACC 1 /	3 $N_{tracks} \geq 3$	13 $\Delta(\phi_0) > \frac{2\pi}{8}$	118 $\|\Sigma q\| < N_{tracks}$		
$ACC 2 /	2 $N_{tracks} \geq 2$	17 $\Delta(\phi_0) > \frac{6\pi}{8}$	118 $\|\Sigma q\| < N_{tracks}$		
$ACC 3 /	2 $N_{tracks} \geq 2$	13 $\Delta(\phi_0) > \frac{2\pi}{8}$	118 $\|\Sigma q\| < N_{tracks}$		
$ACC 4 /	1 $N_{tracks} \geq 1$	51 $N_{st,med} \geq 1$			
$ACC 5 /	1 $N_{tracks} \geq 1$	61 $N_{st,hi} \geq 1$			
$ACC 6 /	53 $N_{st,med} \geq 3$				
$ACC 7 /	-25 $N_{st,junk} < 5$	52 $N_{st,med} \geq 2$	61 $N_{st,hi} \geq 1$	75 $S_E > 10$	-83 $\Theta_S \geq \frac{5\pi}{16}$
$ACC 8 /	-25 $N_{st,junk} < 5$	51 $N_{st,med} \geq 1$	62 $N_{st,hi} \geq 2$	75 $S_E > 10$	-83 $\Theta_S \geq \frac{5\pi}{16}$
$ACC 9 /	-25 $N_{st,junk} < 5$	63 $N_{st,hi} \geq 3$	74 $S_E > 8$	-83 $\Theta_S \geq \frac{5\pi}{16}$	
$ACC 10 /	-25 $N_{st,junk} < 5$	52 $N_{st,med} \geq 2$	75 $S_E > 10$	-83 $\Theta_S \geq \frac{5\pi}{16}$	
$ACC 11 /	-25 $N_{st,junk} < 5$	51 $N_{st,med} \geq 1$	61 $N_{st,hi} \geq 1$	75 $S_E > 10$	-83 $\Theta_S \geq \frac{5\pi}{16}$
$ACC 12 /	-25 $N_{st,junk} < 5$	62 $N_{st,hi} \geq 2$	74 $S_E > 8$	-83 $\Theta_S \geq \frac{5\pi}{16}$	
$ACC 13 /	61 $N_{st,hi} \geq 1$	78 $S_E > 16$	81 $\Theta_S < \frac{\pi}{16}$		
$ACC 14 /	-25 $N_{st,junk} < 5$	62 $N_{st,hi} \geq 2$	77 $S_E > 14$		
$ACC 15 /	-23 $N_{st,junk} < 3$	51 $N_{st,med} \geq 1$	91 $N_{st,timed} \geq 1$		
$ACC 16 /	-23 $N_{st,junk} < 3$	61 $N_{st,hi} \geq 1$	91 $N_{st,timed} \geq 1$		
$REJ 0 /	REJECT ALL THE REST				

Table 4.2 : A set of condition strings for the filter program , where, for example, $N_{st,hi}$ means the number of stacks which have a high energy level, as defined in table 4.1

4.5 Reconstruction program

The events that successfully pass through the filter program are then processed by the main reconstruction program, called OFFRAM . This consists of a number of semi-independent programs that reconstruct the events and perform other event analyses. These programs can be run on any type of computer available within the collaboration (IBM, CDC or UNIVAC).

CELPAT is the processor concerned with the central detector and it performs its pattern recognition by correlating the charge deposited on the 30° and 90° cathodes of a chamber or by matching anode hits with cathode hits. Circular bands are searched for tracks in the $r - \phi$ projection.

The processor FITT then uses the information from CELPAT to set the reconstructed tracks within the CELLO coordinate system and to obtain geometrical information such as the position of the interaction point. The exact value of the magnetic field is calculated by the program CGDT, which is then used by FITT to improve the track reconstruction.

The liquid argon calorimeter data is analysed by the program LATRAK, which uses the geometrical correlations between the u, v and w strips to decide which channels have been fired. The program starts by correlating hits from the three orientations in seven layers and building up two dimensional cells. The cells are then grouped into layer clusters, each of which has a principal axis. Three dimensional clusters are then formed by combining clusters at different depths. The axis of the cluster is determined by fitting a straight line through the cluster centres.

The program concerned with data from the muon chambers is MUCH, which reconstructs the point of impact in the chambers. This is done unambiguously using information from the anode wires and the two cathode

strip planes.

The LINKJOB program combines the track information from the various parts of the detector.

The output from OFFRAM is read onto a DST (Data Summary Tape) which contains for each event, information from each of the processors, the raw data and the reconstructed tracks and their vertices.

4.6 Event selection

Once the GOOD filtered events have been fully reconstructed, they can then be passed through various selection processes to yield interesting physics events. The work described in this study is concerned with multihadronic events, which undergo selection in two stages. Firstly, bad tracks within an event are rejected and then the event as a whole is subjected to selection criteria.

Charged tracks are rejected if they fulfil any of the following conditions:

(a) $|cos(\theta_T)| > 0.86$, where θ_T is the angle the reconstructed track makes with the beam axis

(b) number of central detector hits < 8

(c) momentum, $p < 200$ MeV

(d) momentum, $p > 10 \cdot E_{beam}$

(e) distance to the vertex in the $r - \phi$ plane $Z_V > 1.95$ cm

Neutral showers detected in the liquid argon calorimeter are rejected if they fulfil either of the following two conditions :

(f) $|cos(\theta_T)| > 0.86$

(g) $E_{Shower} < 200$ MeV

The cuts (a) and (f) on the angular range of accepted charged tracks and neutral showers were made for two main reasons. In the endcap region of the detector, i.e., $|cos\theta| > 0.89$, the background from photon-photon interactions is large, and also in this region efficiency calculations are made difficult because of the smaller number of chambers in this area. Cut (b) ensured that the charged tracks were reconstructed well and hence their position was determined accurately. The rejection of low energy showers (g) and charged particles (c) means that the remaining tracks and showers have an energy or momentum above the energy threshold of the various detector components. This energy threshold exists because of inherent electronic noise in the amplifiers and renders an energy measurement below this level unreliable. Cut (d) is applied, since for tracks with $p > 10 \cdot E_{beam}$ the resolution of the central detector becomes bad. The distance to the vertex should be small (e) to eliminate beam wall events.

A final selection of multihadronic events was then made based on both the charged particle and the neutral shower information.

The events were accepted if they obeyed the following conditions :

(1) the number of charged tracks had to be at least 5

(2) the number of negatively charged tracks had to be at least 1

(3) the total visible charged energy $\sum |p_i| > 0.20W$

(4) the total neutral shower energy $\sum E_{Shower} > 0.02W$

(5) the total visible energy $\sum |p_i| + E_{Shower} > 0.4W$

(6) the maximum angle between any two charged tracks in the $r - \phi$ plane, $\phi_O > 130°$

Events arising from beam-gas interactions are eliminated by cuts on the momenta (c), the vertex (e), the charge(2) and on the total event energies

(3)-(5). Condition (6) rejects events which have a cone-like structure such as those that occur from off-momentum electrons, which initiate a large shower in part of the central detector. A visual scan of a large fraction of the data gave an upper limit of 0.1% for remaining background events of this type. Events of the type $e^+e^- \rightarrow \tau^+\tau^-$ have a small number of charged tracks and a low visible energy and are hence rejected by conditions (1) and (3)-(5). A Monte Carlo simulation of this process found that the remaining background from this process was less than 0.1%. Radiative bhabha events can lead to several particles in the central detector arising from the conversion of a photon in the beampipe, but are reduced to a negligible amount by condition (1).

Events in which the hadrons result from a photon-photon interaction are rejected by imposing the conditions (3)-(5). In this process, only a small fraction of the visible energy is measured in the central detector since most of the energy is carried off by the electron and positron at small angles. Figure 4.2 shows that applying the cut on the total visible energy removes the background events that this process produces. A background of 0.9% from two photon scattering remained after the application of these cuts.

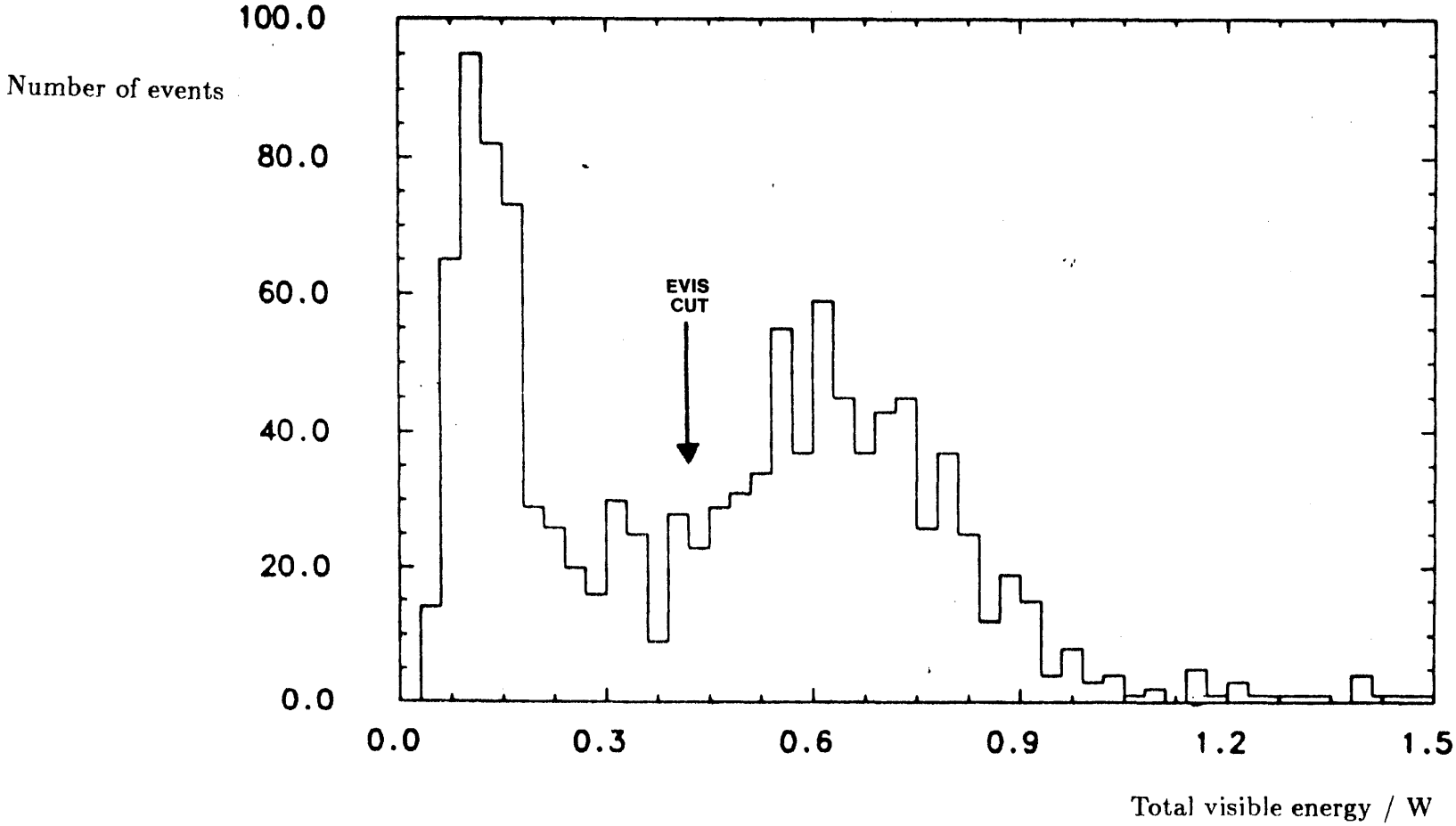

Figure 4.2 : Distribution of the total visible energy before event energy cuts showing the $\gamma\gamma$- background

CHAPTER FIVE

STUDY OF HADRONIC FINAL STATES

5.1 Introduction

In this chapter, general properties of jets produced by e^+e^- annihilation are presented. The production of jets and their subsequent fragmentation have been studied by using charged and neutral particles at a centre-of-mass energy of around 44 GeV. At this energy, the process $e^+e^- \rightarrow hadrons$ is dominated by the production of the quark pairs $u\bar{u}, d\bar{d}, s\bar{s}, c\bar{c}$ and $b\bar{b}$, with a small fraction of events originating from hard gluon bremsstrahlung,i.e., $e^+e^- \rightarrow q\bar{q}g$.

As has been mentioned in chapter 2, the events produced by the fragmentation of a $q\bar{q}$ pair show a two jet structure, whilst a small number of three jet events occur from initial state gluon radiation. Contributions from both these event types are included in the data described in this chapter.

In this analysis, the results represent the sum of the contributions from the different quark flavours. The ratio of the cross-sections for the different quark flavours produced in e^+e^- annihilations, to lowest order, is the ratio of the quark charges squared;

$$u\bar{u} : d\bar{d} : s\bar{s} : c\bar{c} : b\bar{b} = 4 : 1 : 1 : 4 : 1$$

5.2 Variables used

The variables used in this analysis are based on the measurement of the momentum of charged tracks and of the energy deposited by neutral particles.

The momentum of a charged particle, or energy of a neutral particle in

an event with N particles is denoted by

$$p_i \qquad \text{where} \quad i = 1, \ldots, N$$

This is used in the definition of the sphericity tensor and its associated normalized eigenvalues Q_1, Q_2 and Q_3, given in chapter 1. Two other event measures can be defined using these eigenvalues. These are $\langle p_{Tin}^2 \rangle$ and $\langle p_{Tout}^2 \rangle$, the average squared transverse momenta 'in' and 'out' of the plane, respectively. These two quantities are defined as

$$\langle p_{Tin}^2 \rangle = \frac{1}{N} \sum_i (\vec{p}_i \cdot \hat{n}_2)^2 = Q_2 \frac{\sum p_i^2}{N}$$

$$\langle p_{Tout}^2 \rangle = \frac{1}{N} \sum_i (\vec{p}_i \cdot \hat{n}_1)^2 = Q_1 \frac{\sum p_i^2}{N}$$

where $\hat{n}_1, \hat{n}_2$ are the eigenvectors associated with the eigenvalues Q_1 and Q_2. Thus, $\langle p_{Tin}^2 \rangle$ is the square of the momentum component perpendicular to the jet (sphericity) axis in the event plane , and averaged over all the particles in an event, whilst $\langle p_{Tout}^2 \rangle$ is the square of the momentum component normal to the event plane, similarly averaged.

In addition to the momentum of a particle, two other particle properties can be calculated. The particle transverse momentum, p_T, and the longitudinal particle momentum, p_L, are defined relative to the jet axis. For example, the p_T of a particle is the component of its momentum perpendicular to the jet axis. The event measure thrust as shown in equation 1-5 is calculated using longitudinal particle momenta.

The angles that the thrust and sphericity axes make with the beam axis (in the CELLO coordinate system, this is defined as being in the z-direction) are denoted by Θ_T and Θ_S, respectively

The particle production along the jet axis was also analysed using the rapidity y, defined by

$$y = \frac{1}{2} ln \frac{E + p_L}{E - p_L}$$

where E is the energy of the particle. In calculating the energy of the charged particle, its mass was taken to be the pion mass.

5.3 Energy-energy correlations

Energy-energy correlations were first proposed by Basham et al [**57**], as a method to investigate the angular distribution of the partons and the emission of both hard and soft gluons. The energy-energy correlation is defined as

$$\frac{1}{\sigma}\frac{d\Sigma^{EEC}}{d\chi} = \frac{1}{Ns\Delta\chi}\sum_{n=1}^{N}\sum_{i,j} E_i E_j$$

where E_i, E_j are the energies of two particles i and j, which are separated by an angle χ, N is the number of events and $\Delta\chi$ is the bin width in χ. Thus, it is the energy weighted sum over all two-particle combinations whose angular separation is between χ and $\chi+\Delta\chi$. The normalisation is such that

$$\int_0^{180}\frac{1}{\sigma}\frac{d\Sigma^{EEC}}{d\chi}d\chi = 1$$

when self combinations at $\chi = 0°$ are included. The asymmetry of the energy-energy correlation can also be calculated,

$$A(\chi) = \frac{d\Sigma^{EEC}}{d\chi}(180° - \chi) - \frac{d\Sigma^{EEC}}{d\chi}(\chi)$$

Schematic representations of the energy-energy correlation and its related asymmetry are shown in figure 5.1, for several event configurations. In the process $e^+e^- \rightarrow q\bar{q}$ two back-to-back partons are produced, which give two delta functions at $\chi = 0°$ and $\chi = 180°$. However, because of the finite resolution of the calorimeter in χ, the energy-energy correlation becomes like figure 5.1(a), i.e., with finite bin width. When the fragmentation process is taken into account, the shape of the energy-energy correlation becomes dependent on the transverse momenta of the hadrons. For example, figure 5.1(b) shows the result if only collinear hadrons are produced, whilst figure

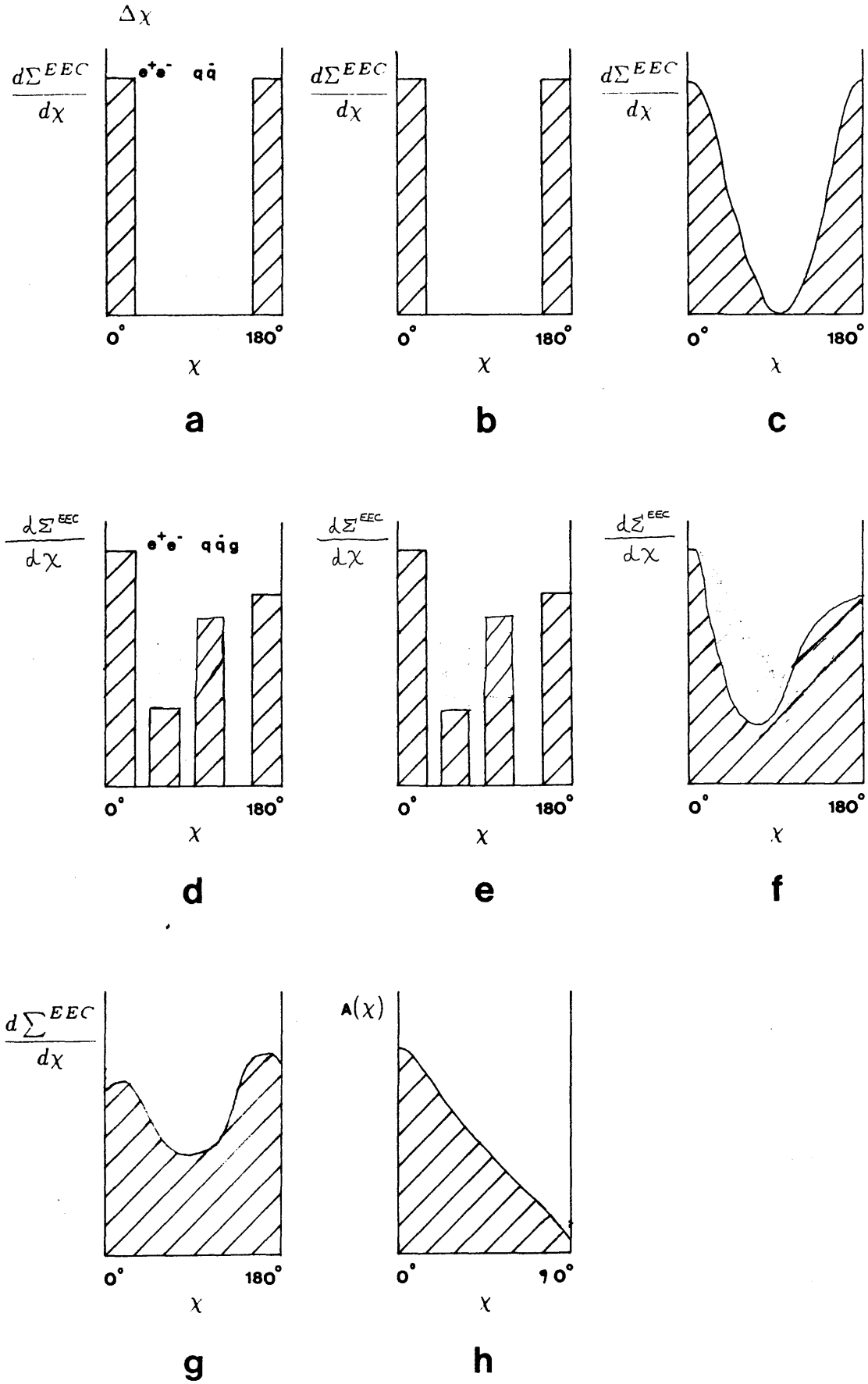

Figure 5.1 : Schematic representation of the energy energy correlation and its asymmetry

5.1(c) shows the effect of limited hadron transverse momenta, smearing the forward and backwards peaks.

A particular process $e^+e^- \rightarrow q\bar{q}g$ leads to a gluon being emitted at a given angle with finite energy, thus giving the parton distribution of figure 5.1(d). The three peaks in this diagram outside the $\chi = 0°$ region correspond to the three angles between the quark, antiquark and the gluon. If the hadrons are produced collinear to the partons then the picture remains unchanged (figure 5.1(e)) but the inclusion of transverse momenta produces the smeared distribution of figure 5.1(f). Figures 5.1(g) and 5.1(h) show the energy energy correlation and its related asymmetry for the case where a hard gluon is emitted in the initial state, thus leading to a broad third jet of hadrons. It can be seen from figure 5.1(h) that the asymmetry enhances the contribution from hard gluon radiation relative to the quark pair production contribution. Thus, the use of the energy-energy correlation asymmetry increases the sensitivity to α_S.

5.4 Further track and event Selection

Before a final selection of multihadronic events was made, several additional track cuts were made. This was to ensure, in particular that the neutral component of the events consisted of well measured photons. These cuts and the rationale behind them are described below.

In the shower reconstruction program, LATRAK, clusters of deposited energy are reconstructed in each of the seven layers of each lead-liquid argon module. This is achieved by using the geometrical correlations between the three channel orientations u, v and w and between adjacent channels in depth. The clusters are formed in two dimensions and then combined longitudinally into three-dimensional showers. The topology of these showers i.e., whether they result from single or overlapping photons is then determined.

This is done by determining the two principal axes and the corresponding sigmas of each two dimensional cluster. The clusters are then separated into single and double shower candidates by checking these sigmas.

The LINKJOB extrapolates tracks found in the inner detector into the liquid argon calorimeter. The position of the extrapolated tracks are then used in the reconstruction of the two-dimensional clusters. This leads to the separation of the final reconstructed showers into two types :

(a) charged showers - those showers that can be linked to charged tracks

(b) neutral showers - those showers for which no link to charged tracks can be found.

It should be noted that this technique of linking tracks with showers is not 100% efficient. Hence, cuts on the longitudinal development of the shower have to be employed to distinguish photons from charged particles where the linking procedure has failed. These cuts also help to distinguish photons from neutrons and K^0's.

The following criteria are used to select well measured photons:

(1) photons that result from two or more overlapping showers are rejected

(2) neutral showers are rejected if the total charge deposited in the second and third layers is less than 20 % of the total deposited charge

(3) neutral showers are rejected if more than 5% of the total charge is deposited in the seventh layer

(4) photons that do not extend in depth over at least three layers are rejected

(5) photons have to be in the angular range $0.05 < |cos\theta| < 0.84$, where θ is the angle the photon makes with the beam direction

(6) photons that have an energy less than 500 MeV are rejected

The shape of an electromagnetic shower in the lead-liquid argon calorimeter is essentially that of a large deposition of energy near the front of the calorimeter, that is, within layers two and three, followed by a rapid decrease in energy deposition until at the back of the calorimeter only a small amount of energy is deposited. Thus, conditions (2) and (3) ensure that the distribution of the energy deposited in the calorimeter modules is approximately in the shape of an electromagnetic shower. Condition (4) removes showers that are a result of noise within the calorimeter system. This problem became worse at high beam energies of around 22 GeV. The introduction of cut (6) was also found to be necessary at high beam energies and meant that showers which were a result of background were rejected. At a beam energy of 17 GeV, a minimum photon energy of 300 MeV was found to be a sufficiently hard cut. The use of condition (5) meant that the photon was contained within the central part of the calorimeter, and was away from the module edges.

The above cuts were extensively checked using multihadronic events and single photon events generated by Monte Carlo, and with Bhabha events. The background due to charged particles where the linking procedure failed, or the misidentification of neutrons or K_L^0 's is less than 1 %, as determined from Monte Carlo studies.

In addition to the cuts on neutral showers, a further constraint was put on the charged tracks. This was done to ensure that all the tracks were well-measured, and so facilitate the agreement between the data and the Monte Carlo. Thus, charged tracks were rejected if less than three of the multiwire proportional chambers in the inner detector fired.

Hence, after these more sophisticated cuts have been made on the charged tracks and neutral showers, the agreement between data and Monte Carlo is better, and therefore, a better understanding of the data is gained. An example of the agreement between the data and the Monte Carlo is shown in figure 5.2 for the momentum distribution.

5.5 Correcting the data

The data, which are obtained from the DST's, need to be corrected by the use of Monte Carlo techniques. This procedure enables the data to be compared directly with other experimental groups' data, provided it too has been corrected. Theoretical predictions can also be investigated by using the corrected data, as for example, in the determination of α_S presented in chapter 6.

Corrections to the data are required for the following reasons.

(1) Initial state radiation; this causes the initial quark- antiquark pair to have less energy than usual and so the visible energy is correspondingly lower. The event is also boosted with respect to the detector, which can lead to the particle momenta being incorrectly measured.

(2) Detector inefficiency; although the CELLO detector has a very good angular coverage, it is sometimes possible that a particle could enter one of the gaps between the modules of the liquid argon calorimeter. Some particles such as the neutron, neutrino and K_L^0 are also not detected, and hence lower the total visible energy. The possibility of particles escaping undetected down the beampipe needs also to be taken into account. Non-functioning components of the detector, such as broken wires, can also lead to inefficiencies as can the cuts used to select well measured photons and charged tracks.

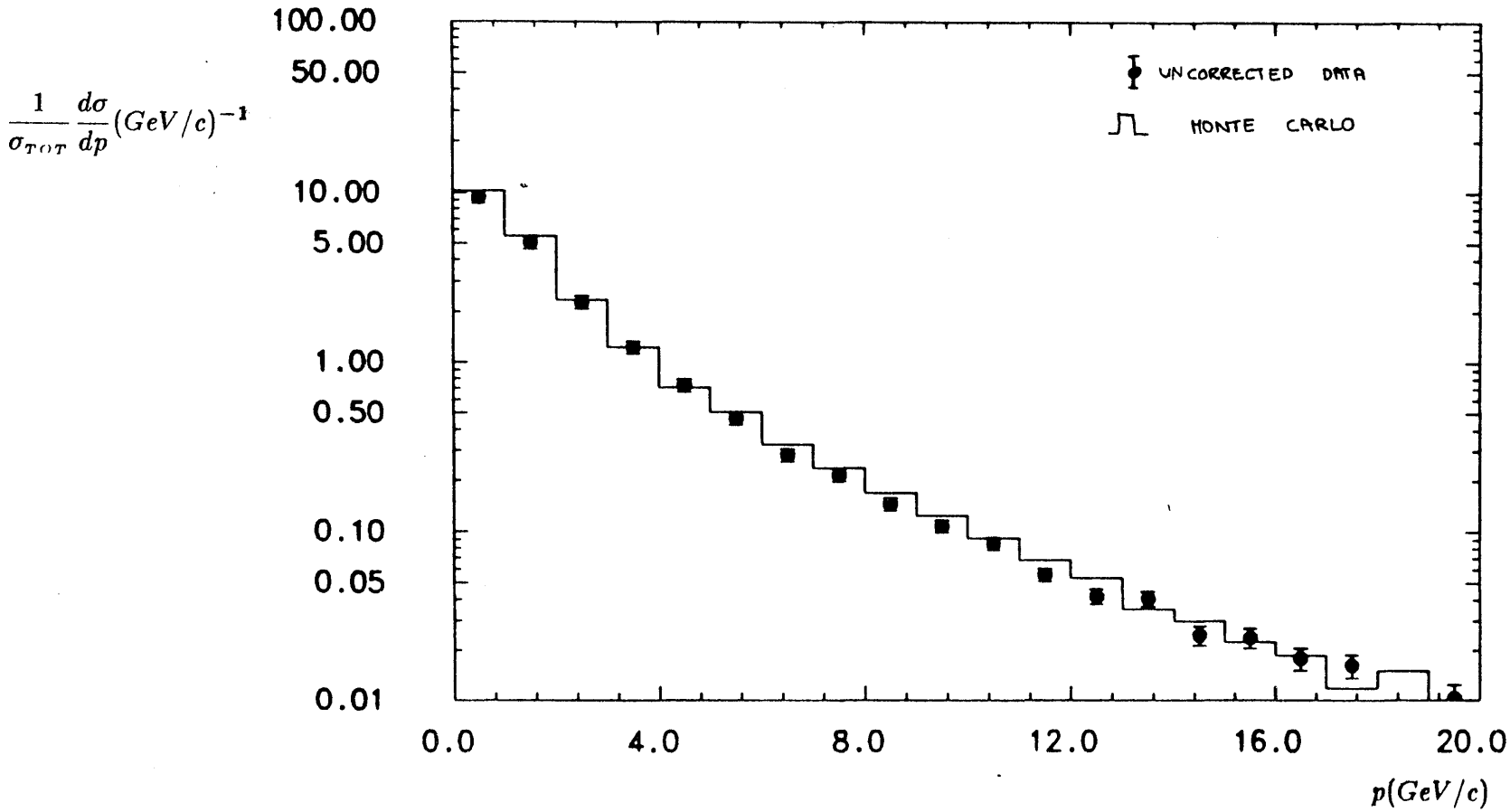

Figure 5.2 : Comparison between the CELLO Monte Carlo and CELLO uncorrected data for the particle momentum spectrum

(3) Reconstruction inefficiencies; these can occur when two particles are nearly collinear, which can lead to one of the particles not being detected. There is also the problem of charged tracks being misidentified as neutrals, because of the failure of the linking procedure. These inefficiencies lead to a reduction in the event multiplicity and in the total detected energy.

(4) Triggering inefficiency; this is as a result of the online trigger system wrongly classifying an event. However, this effect is expected to be very small in this analysis because of the selection cuts imposed on the events.

(5) Resolution inefficiency; the corrections need to take into account the finite resolution of the detector, and also the fact that the mass of the charged particles is assumed to be that of a charged pion.

The procedure for correcting the data involves the generation of two sets of Monte Carlo events. The first set includes a full simulation of the detector and is passed through the complete reconstruction chain, whilst the second set is generated independent of the detector and the reconstruction process.

The first stage in generating the first set of Monte Carlo events was to generate the initial state partons using the LUND Monte Carlo [**58**] - JETSET version 5.2. Initial state radiation was taken into account up to order α_{em}^3 through the program by Berends and Kleiss [**59**] . The LUND program uses the second order approximation of perturbation theory to generate a parton configuration, which can consist of $q\bar{q}$, $q\bar{q}g$, $q\bar{q}gg$ and $q\bar{q}\bar{q}q$ final states. Since the theoretical expressions for the last three of these configurations diverge as a result of infrared and collinear singularities, an invariant mass cut-off Y_{min} is introduced. The squared parton-parton invariant mass is defined by

$$Y_{ab} = \frac{(P_a + P_b)^2}{W^2}$$

where W is the center-of-mass energy and P_a, P_b are the four-momenta of any two partons a and b.

Thus, if a three parton final state event contains a parton pair with $Y_{ab} < Y_{min}$, then this event is removed from the three parton sample and treated as a two parton event. The addition of these events to the two parton cross section cancels its divergences, as discussed earlier, which leads to a finite expression. This procedure also removes explicitly the divergences from the three parton cross section, and gives individually finite two, three and four parton final state cross sections.

The next stage is the hadronization of the partons, which takes place according to the prescription of the LUND string fragmentation model, given in section 3-4.

A description of the various parameters that are used by the LUND Monte Carlo, and the way in which the values of these parameters were determined is now given.

Quark or diquark pairs are produced in the colour force fields of the initial partons, with a ratio $R_q = \frac{P(qq)}{P(q)}$. The probability for creating s quarks relative to u or d quarks is given by the ratio $R_f = \frac{P(s)}{P(u)}$. The fraction of primary mesons that have spin one, as opposed to spin zero, is dependent on whether the meson contains heavy (c or b) or light quarks. This gives rise to two numbers, r_H and r_L, the vector meson probabilities for heavy and light mesons, respectively.

The longitudinal fragmentation of the initial quarks is governed by two fragmentation functions. For u, d and s quarks the LUND symmetric function of equation 2-4 is used, the nature of which depends on the two parameters a and b described earlier. The Peterson fragmentation function of equation 2-5 is used for c and b quarks, which introduces the parameters

ϵ_C and ϵ_B.

The transverse momentum q_t given to the quarks and antiquarks determines the transverse momentum of the primary hadrons. The quark transverse momentum distribution is a Gaussian of the form $exp(\frac{-q_t^2}{\sigma_q^2})$, where σ_q is $\sqrt{2}$ times the usual definition of Gaussian width. The longitudinal and transverse momentum components discussed above, are defined with respect to the string directions. A quantity E_J is used together with quark masses to define the remaining energy below which the fragmentation of a jet system is stopped. The value of α_S at a specific Q^2 is determined to second order using $\Lambda_{\overline{ms}}$, as defined earlier. Finally, in this stage unstable primary hadrons were allowed to decay according to known branching ratios to produce the final particle configurations from the LUND Monte Carlo.

The values of the above parameters were determined using a Monte Carlo technique. Events were generated by the LUND Monte Carlo without any initial state radiation, and then compared with corrected data. This was done at a centre-of-mass energy of 34 GeV, since several experiments have published corrected data at this energy. In particular, the energy-energy correlation data and its related asymmetry as presented by the JADE Collaboration [**60**] and the properties of jets data as analysed by TASSO [**61**] were used. Thus, through an extensive tuning of the aforementioned parameters, the LUND Monte Carlo was able to describe the available corrected data at a W of 34 GeV. The values of these parameters which were found to give the best fit to the data are given in table 5.1. Comparisons of the LUND Monte Carlo generated with this set of parameters, and the corrected data of TASSO and JADE are shown in figures 5.3 and 5.4.

The third stage in generating the first set of Monte Carlo events was to pass the LUND Monte Carlo final state particles through a series of programs, which simulate the CELLO detector.

PARAMETER	VALUE
R_q	0.09
R_s	0.30
r_H	0.75
r_L	0.50
a	1.0
b	0.6
ε_c	0.0025
ε_b	0.0035
σ_q	0.21 GeV/c
$\Lambda_{\overline{MS}}$	0.5 GeV
Y_{min}	0.010
E_γ	2 GeV

Table 5.1 : The values of the most important parameters used in the LUND Monte Carlo

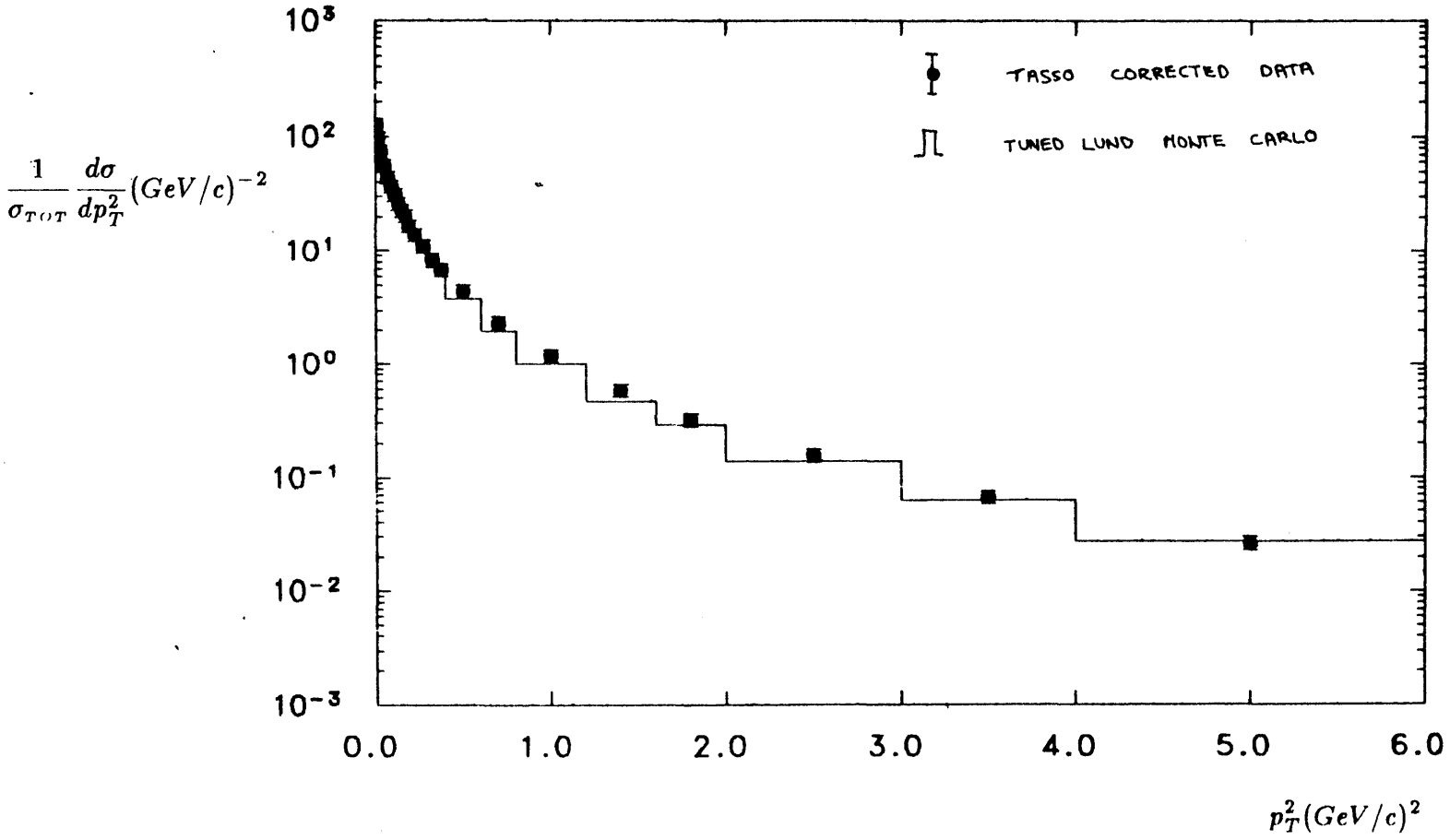

Figure 5.3 : Comparison between TASSO corrected data and the tuned LUND Monte Carlo for the transverse momentum squared spectrum (using the sphericity axis)

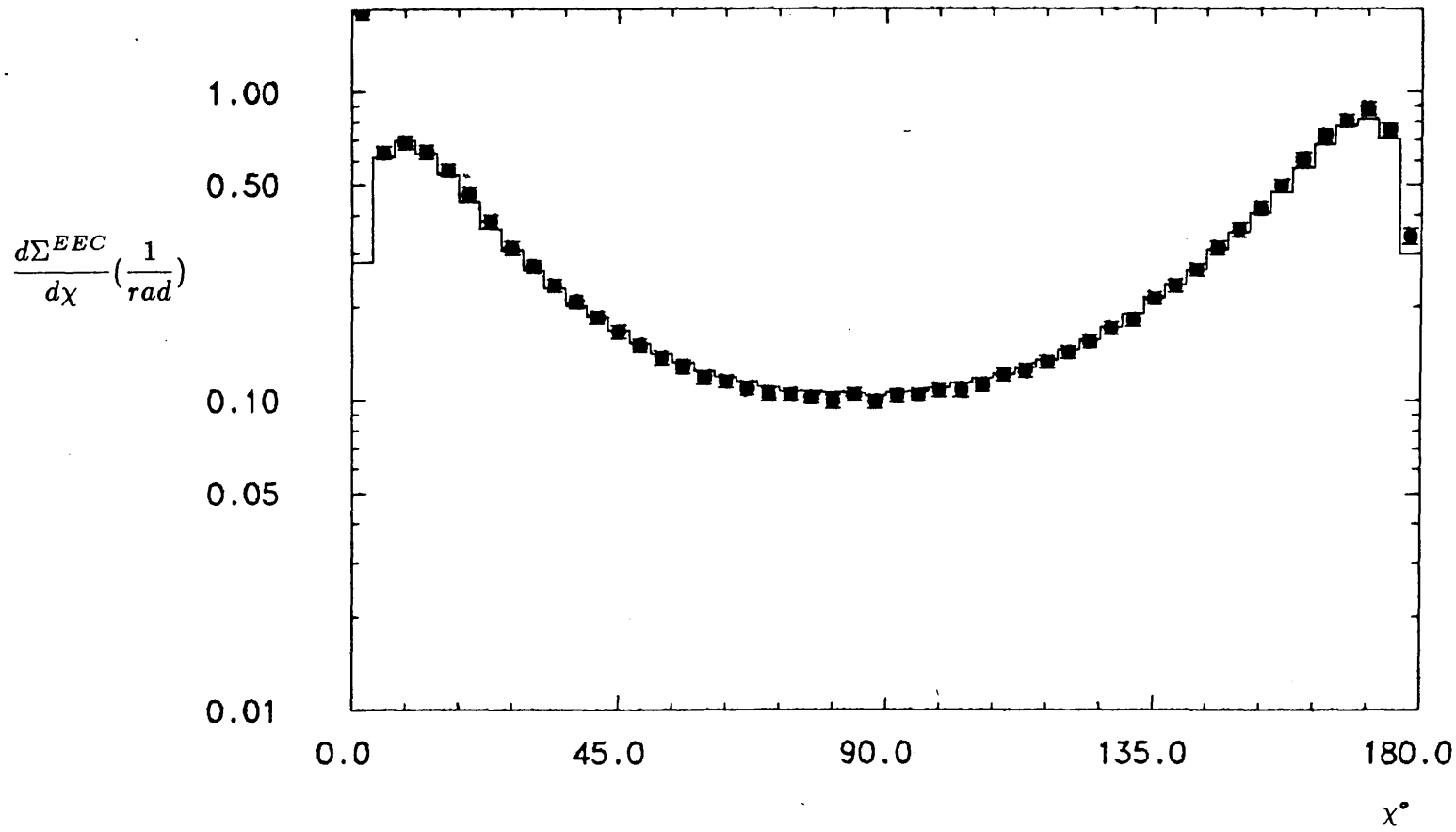

Figure 5.4 : Comparison between JADE corrected data and the tuned LUND Monte Carlo for the energy-energy correlation

The first of these programs is CELLOUT, which reformats the four vectors of the generated particles into a form suitable for the CELLO Monte Carlo. The particles are then analysed by PTRAK, which tracks the particles from the interaction point and then through the beampipe. Particles with a short lifetime, such as K^0's and Λ's, which have not decayed in the LUND program, are allowed to decay and their daughter products are tracked through the detector. After the beampipe, particles are tracked through the inner detector and the liquid argon calorimeter. The program package EGS simulates electromagnetic reactions; both in the beampipe and in the liquid argon calorimeter. Hadronic reactions are dealt with by the HETC program. A simulation of the response of the detector is incorporated in the program CELINT, which uses as input the particles tracked through PTRAK. The finite resolution of the detector is thus taken into account as is noise, through the use of random noise generators. CELINT also uses the information contained in the calibration constants for each detector component. The track information is then put into a raw data format, which means it can then be processed by the reconstruction program OFFRAM.

The reconstructed Monte Carlo events are then subjected to the same trigger conditions and event selection procedure as is applied to the data. Thus, this first set of Monte Carlo events should be similar to the data measured in the CELLO detector.

The second set of Monte Carlo events were generated, as in the first case, using the LUND Monte Carlo. However, initial state radiation was not included although all the other input parameters were identical. These events were not passed through a simulation of the detector, nor were they reconstructed.

Thus, for any given variable, x, such as sphericity, three distributions

now exist :

(a) $d(x)$ - the uncorrected data

(b) $m_1(x)$ - the detector simulated Monte Carlo

(c) $m_2(x)$ - the Monte Carlo independent of the detector

From distributions (b) and (c), a correction factor $C(x)$ is obtained for the effects of the detector on each bin in the histogram of the variable x

$$C(x) = \frac{m_2(x)}{m_1(x)}$$

The division in the above equation is carried out bin by bin for each variable x. The error on the correction factor $\Delta C(x)$ is also worked out on a bin by bin basis ;

$$\Delta C(x) = (\Delta m_1^2(x) + \Delta m_2^2(x))^{\frac{1}{2}}$$

where $\Delta m_1(x)$ and $\Delta m_2(x)$ represent the standard errors on the two respective sets of Monte Carlo events. The corrected data distribution, $d_C(x)$ for a given variable, x, can then be obtained;

$$d_C(x) = d(x)C(x)$$

This procedure was followed for the variables defined earlier in this chapter, thus giving a set of corrected data distributions which could be compared with theoretical predictions. This comparison is valid since the effects of smearing are correctly evaluated because a good approximation to the underlying physics has been used as a result of the tuning procedure described earlier.

5.6 The distributions

Corrected data distributions obtained with the CELLO detector at a centre-of-mass energy of 44 GeV are now presented.

(a) Sphericity. The sphericity distribution shown in figure 5.5 was determined using both charged and selected neutral particles. It can be seen from this figure that most of the analysed multihadronic events have a sphericity less than 0.15, which corresponds to the event having a two-jet structure. This confirms the findings of the TASSO Collaboration [**61**] who found that as the centre-of-mass energy increased the events became more strongly collimated.

(b) Thrust. This distribution was calculated using the same group of particles as in (a). Since the thrust maximises the sum of the longitudinal momentum, a high value of thrust indicates a two-jet structure. Thus, figure 5.6 confirms the observation obtained from the sphericity distribution, that most of the events are two-jet like.

(c) Angular distribution of sphericity axis. The shape of this distribution is well described by the form

$$\frac{1}{N}\frac{dN}{dcos\Theta_S} \propto 1 + cos^2\Theta_S$$

and therefore confirms the theory that the dominant process in the production of multihadronic events is $e^+e^- \rightarrow q\bar{q}$, where the quarks are massless and have spin $\frac{1}{2}$. A fit to the data of the form

$$\frac{1}{N}\frac{dN}{dcos\Theta_S} \sim 1 + acos^2\Theta_S$$

as shown in figure 5.7, gave the value $a = 1.20 \pm 0.13$.

(d) Angular distribution of thrust axis. This is shown in figure 5.8 and is essentially the same shape as that described above for the sphericity

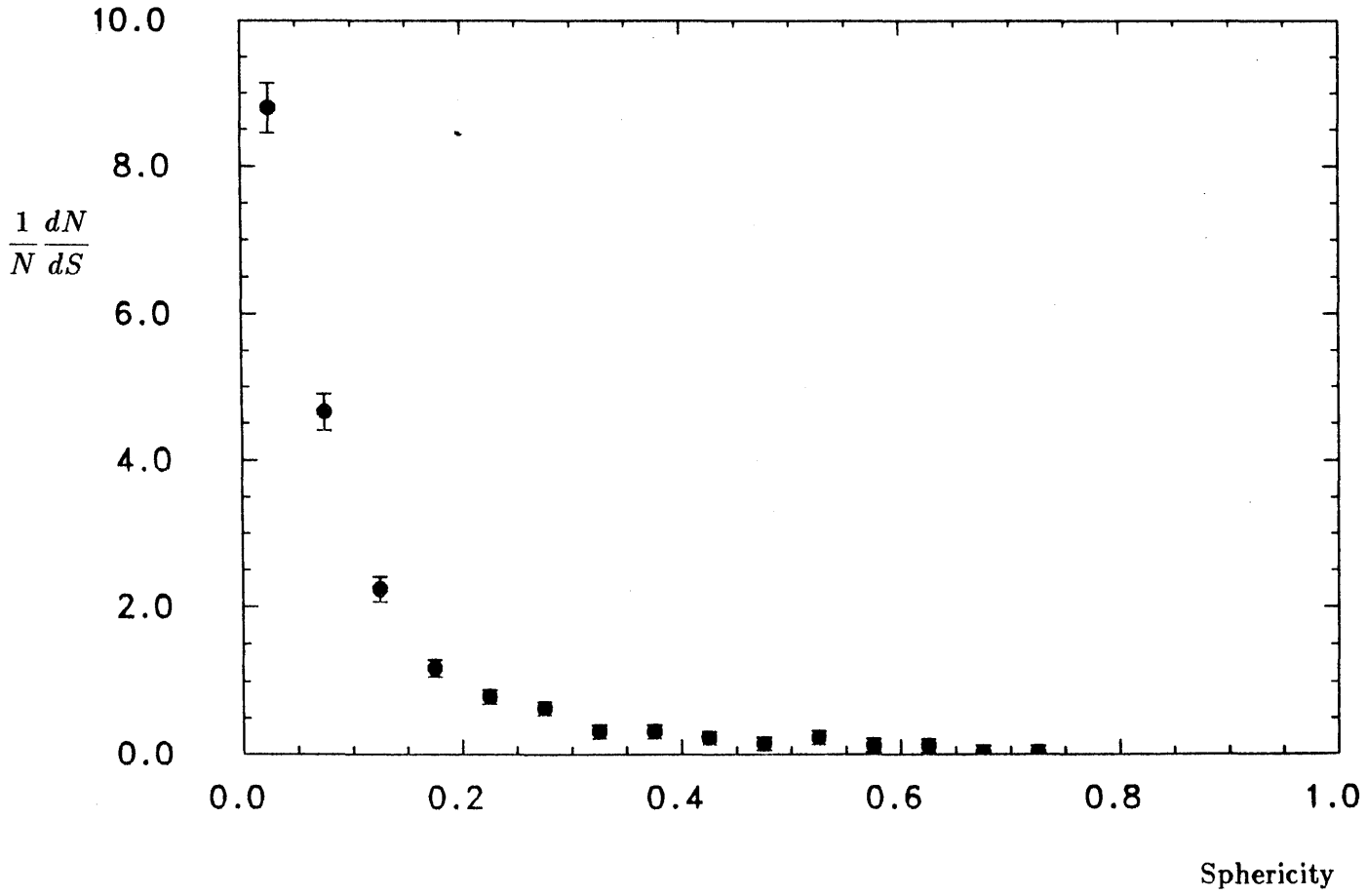

Figure 5.5 : The normalised sphericity distribution

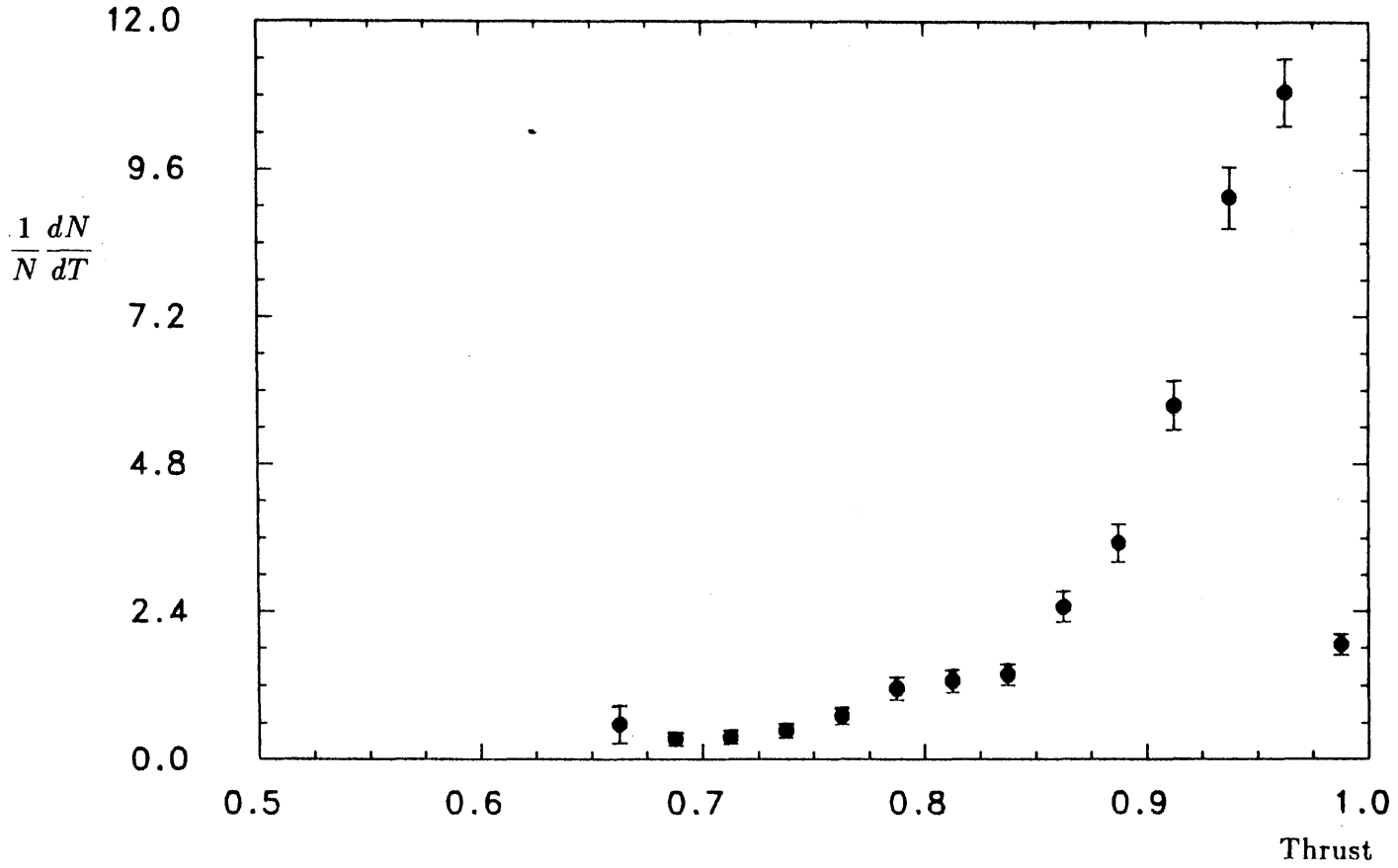

Figure 5.6 : The normalised thrust distribution

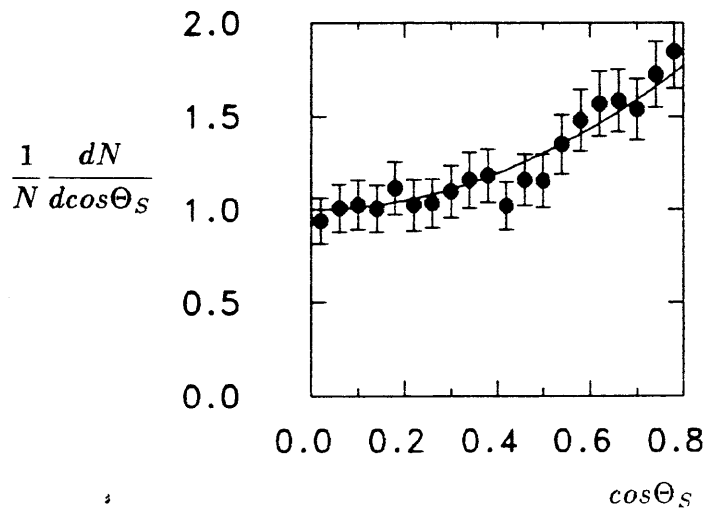

Figure 5.7 : The angular distribution of the jet axis determined by sphericity. The curve is a fit to the data of the form $1 + acos^2\Theta$

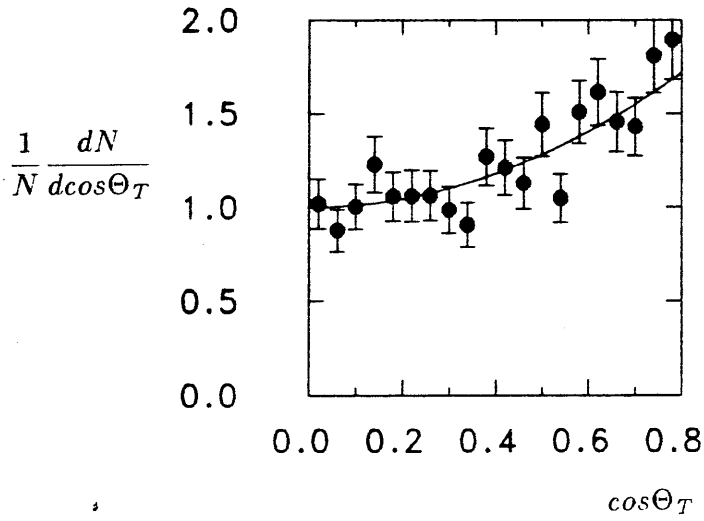

Figure 5.8 : The angular distribution of the jet axis determined by thrust. The curve is a fit to the data of the form $1 + acos^2\Theta$

axis. A similar fit to the data yielded the value $a = 1.12 \pm 0.13$, where a is the coefficient of the $cos^2\Theta$ term. Thus, within errors the two angular distributions are equal and give compatible values of a. This means that the basic physics results are not dependent on the choice of jet axis.

(e) Particle momenta. The differential cross section for charged and neutral particles is given in figure 5.9. The distribution shows a sharp decrease with momentum, although the distribution is broader than the TASSO figure at 34 GeV. Figure 5.10 shows the normalised cross section for the fractional particle momentum, which falls steeply with x_P.

(f) Particle production with respect to the jet axis. The study of the longitudinal and transverse momentum distributions was carried out with respect to the jet axis as determined by both the thrust and sphericity axes. As can be seen from figures 5.11 and 5.12, these distributions are independent of the choice of jet axis. The two figures 5.9 and 5.12 show that the p_L distribution is similar to the momentum distribution. This would be the case if most of the events were two-jet like, since any three jet structure would increase the relative number of tracks with a small value of p_L. The p_T distribution also indicates the jet like nature of the events, since this distibution is highly peaked towards low values of p_T, whereas isotropic events would give a flat distribution in p_T. The long tail of this distribution can be understood as being the result of hard gluon bremsstrahlung, which will produce a third jet of hadrons with non-negligible transverse momenta with respect to the jet axis.

The dependence of $\langle p_T \rangle$ on x_L was also investigated, with both the thrust and the sphericity axes being used as the jet axis. The distributions are shown in figures 5.13 and 5.14, with slight differences apparent, especially at high values of x_L. These differences arise when the two axes are pointing in slightly different directions. For example, at a W of 44 GeV, a

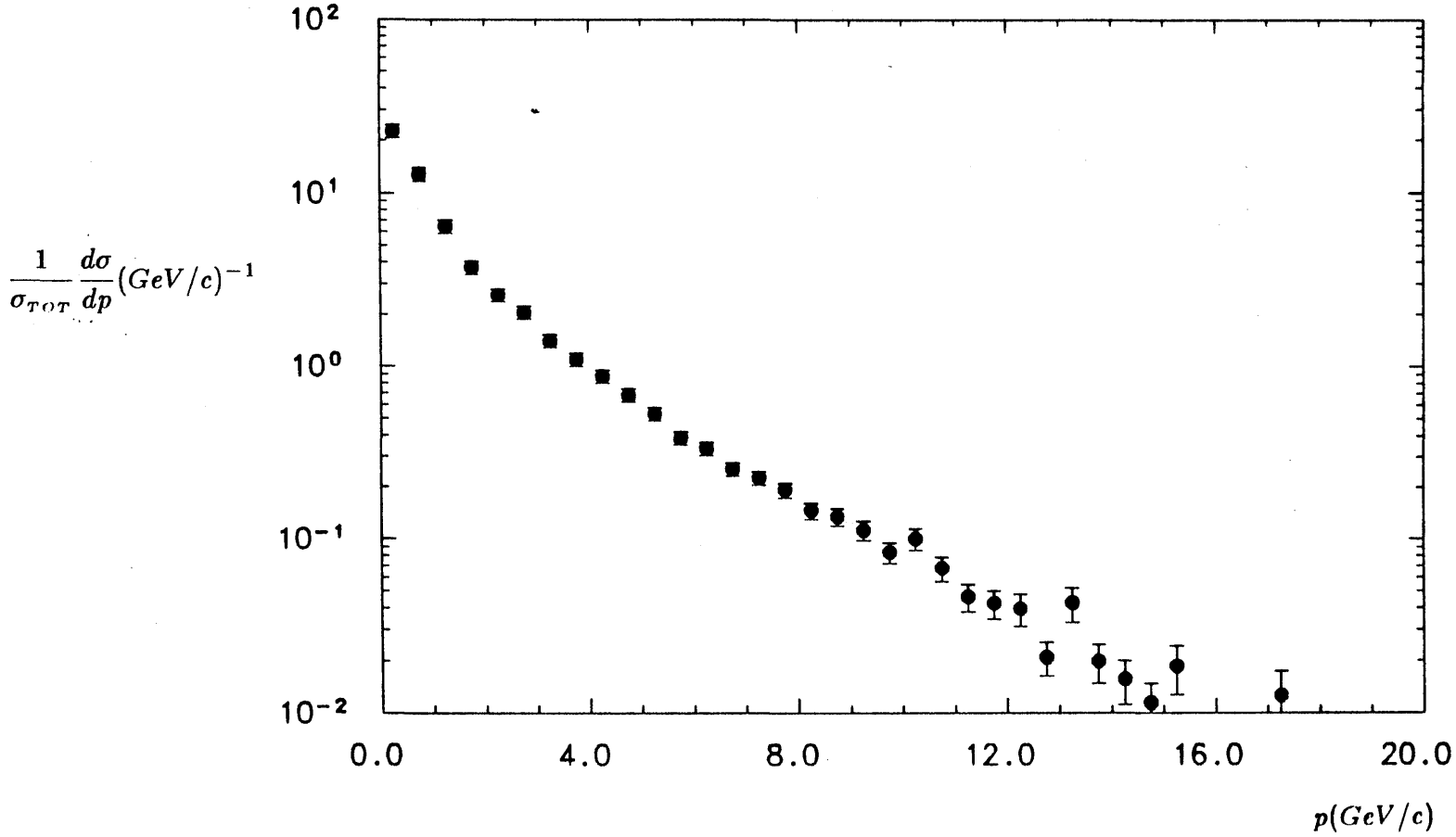

Figure 5.9 : The particle momentum spectrum

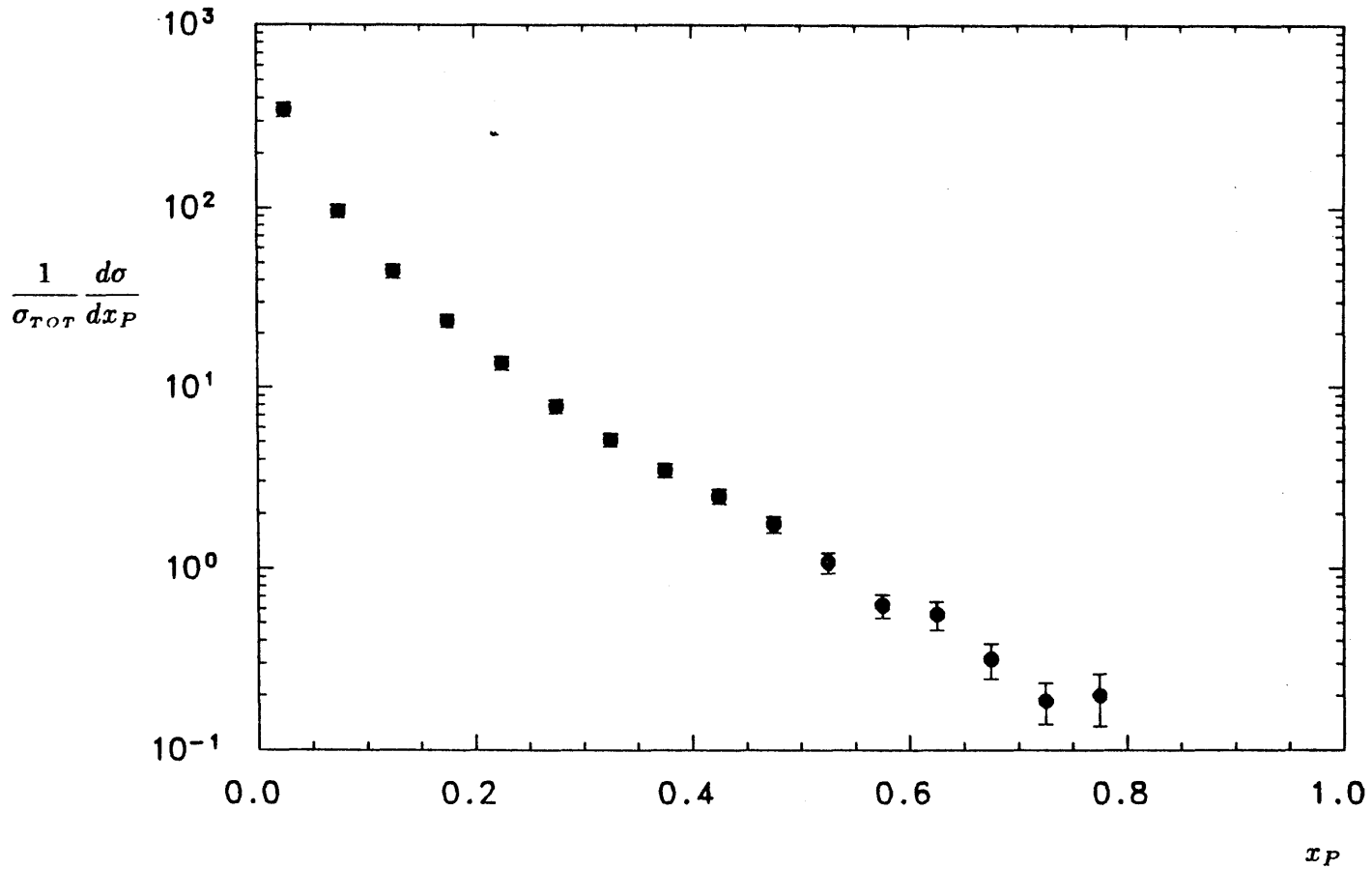

Figure 5.10 : The fractional particle mometum spectrum

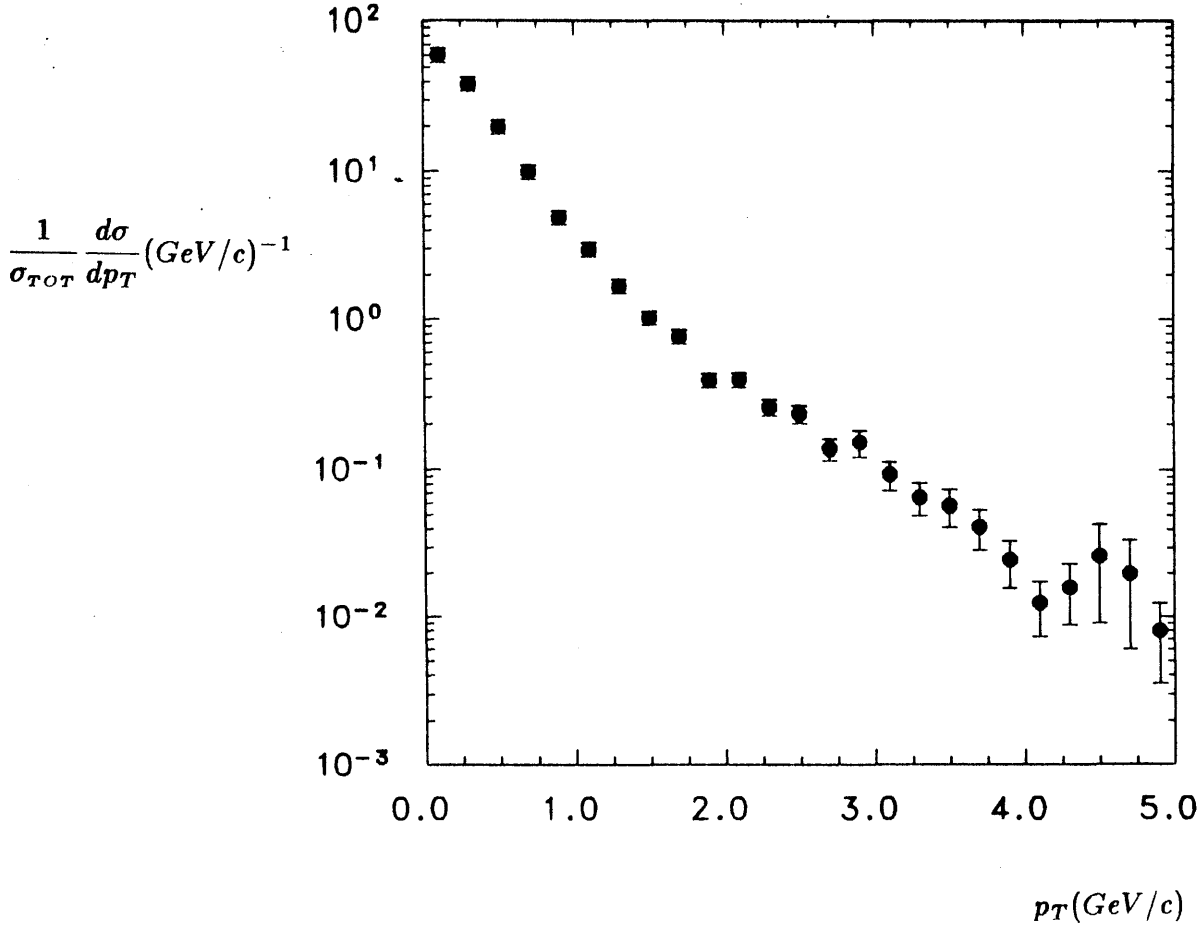

Figure 5.11 (a) : The transverse momentum spectrum with respect to the sphericity axis

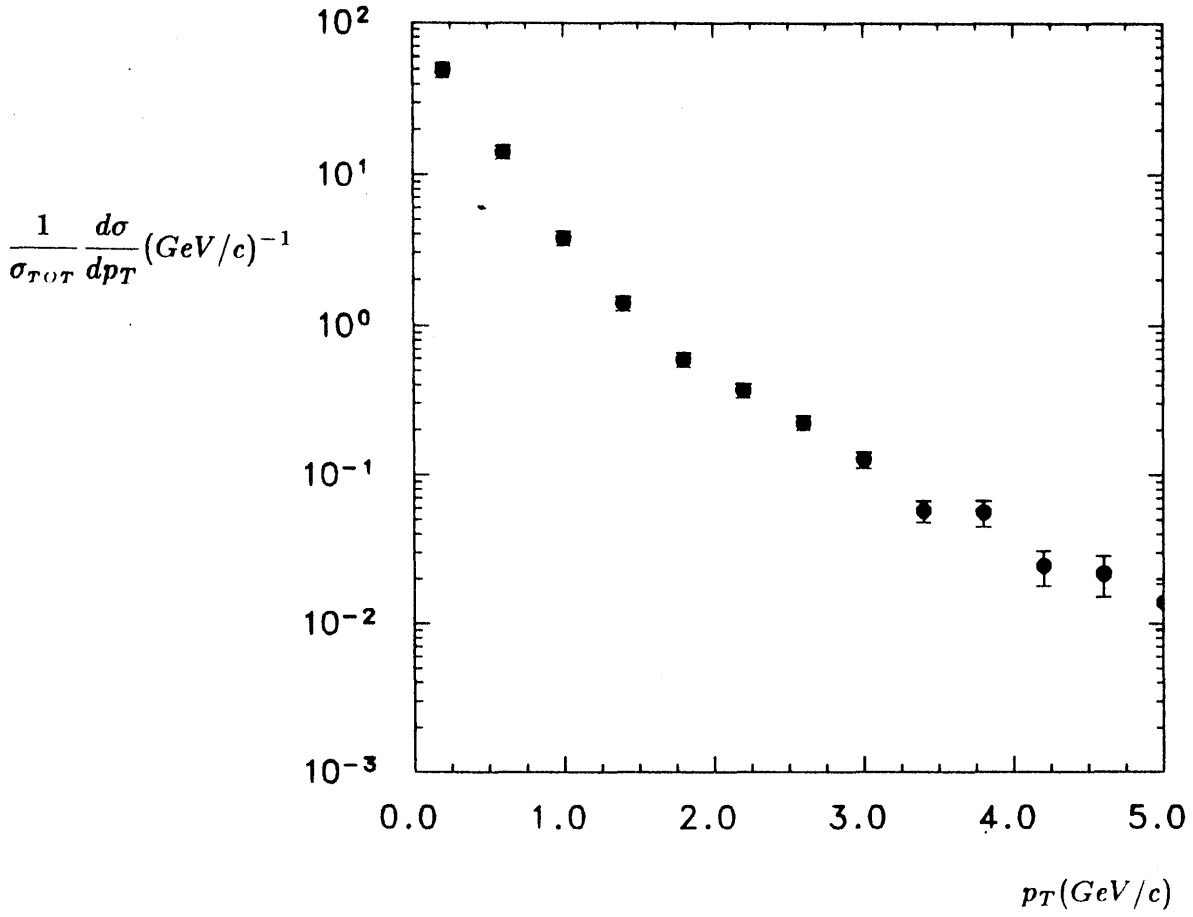

Figure 5.11 (b) : The transverse momentum spectrum with respect to the thrust axis

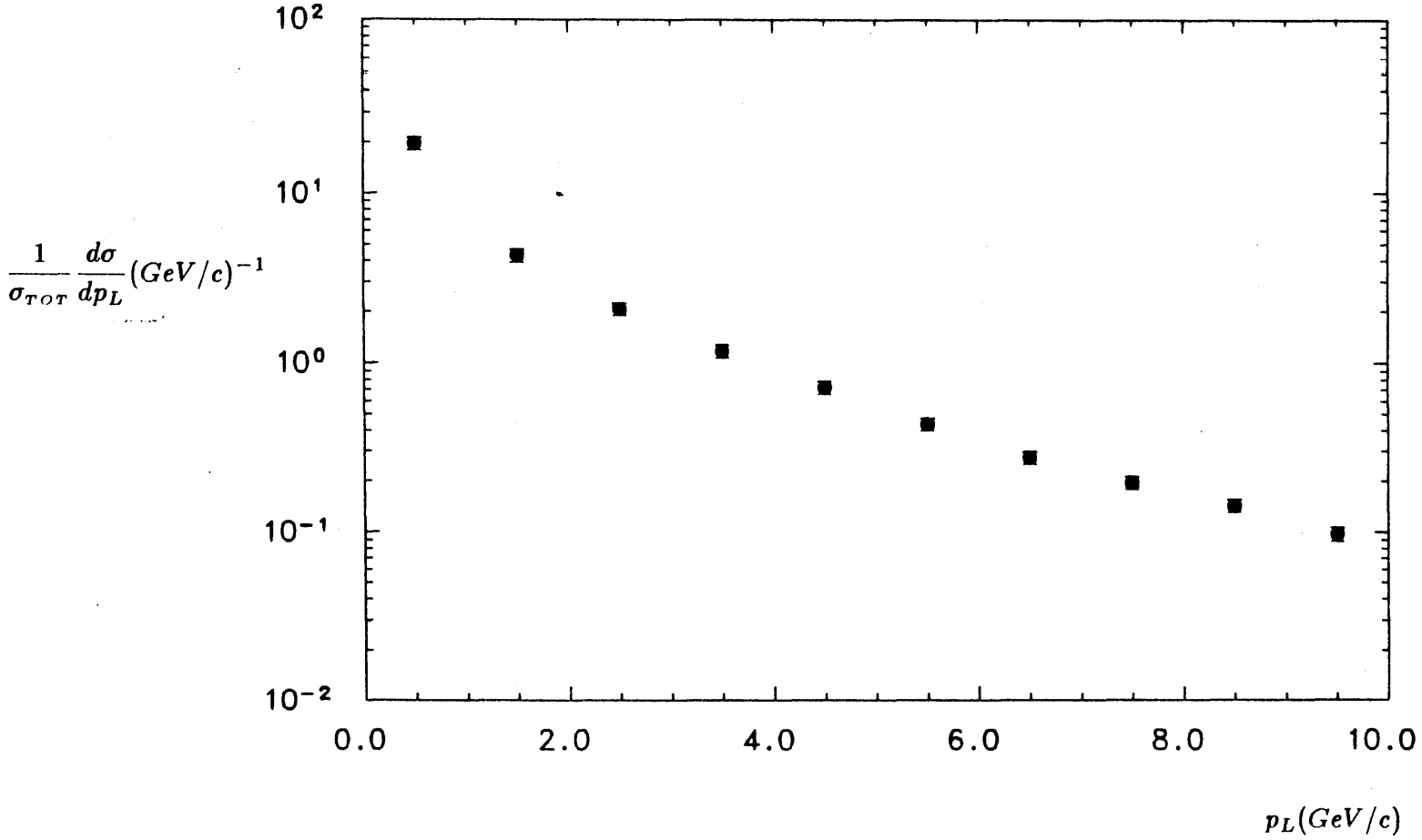

Figure 5.12 (a) : The longitudinal momentum spectrum with respect to the sphericity axis

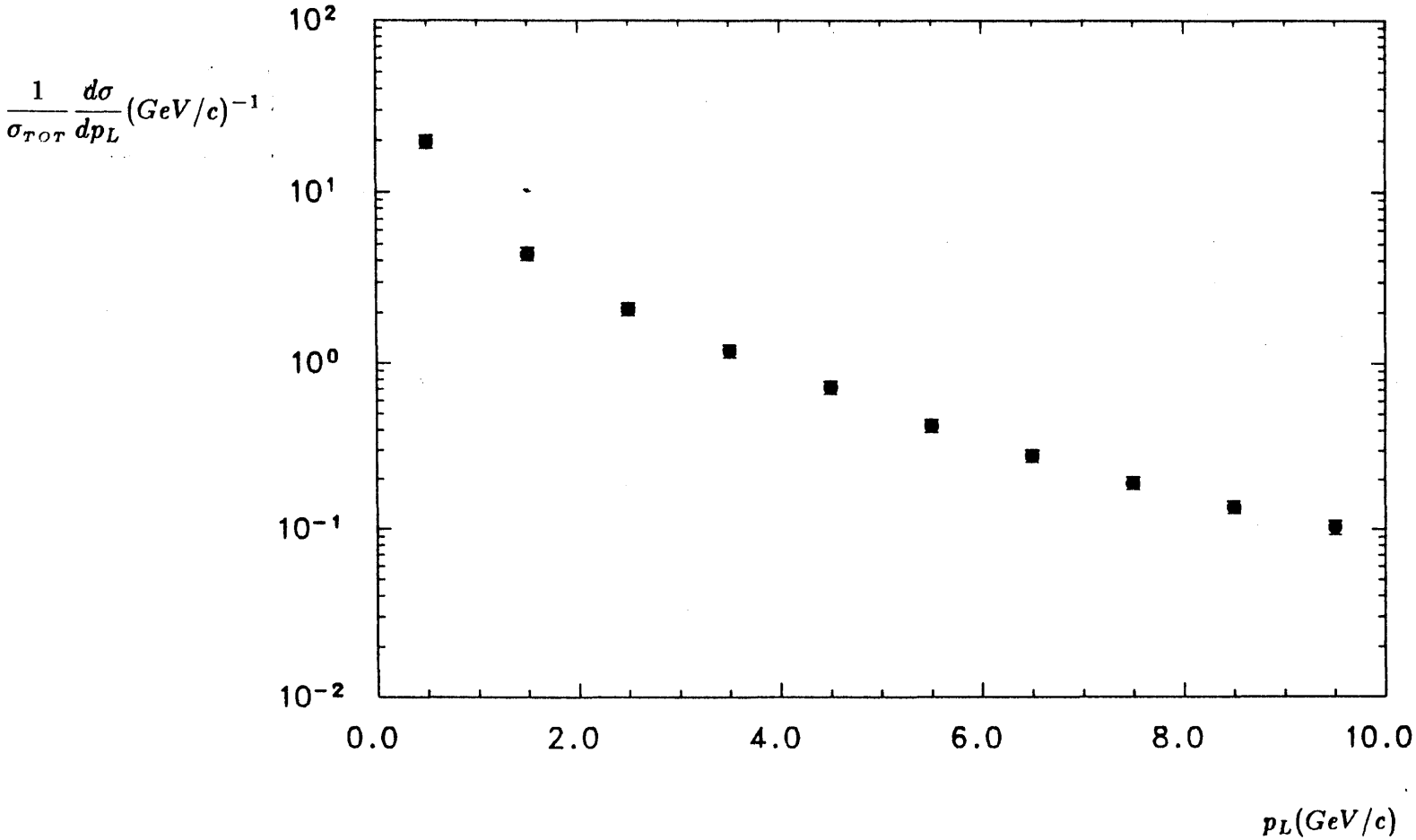

Figure 5.12 (b) : The longitudinal momentum spectrum with respect to the thrust axis

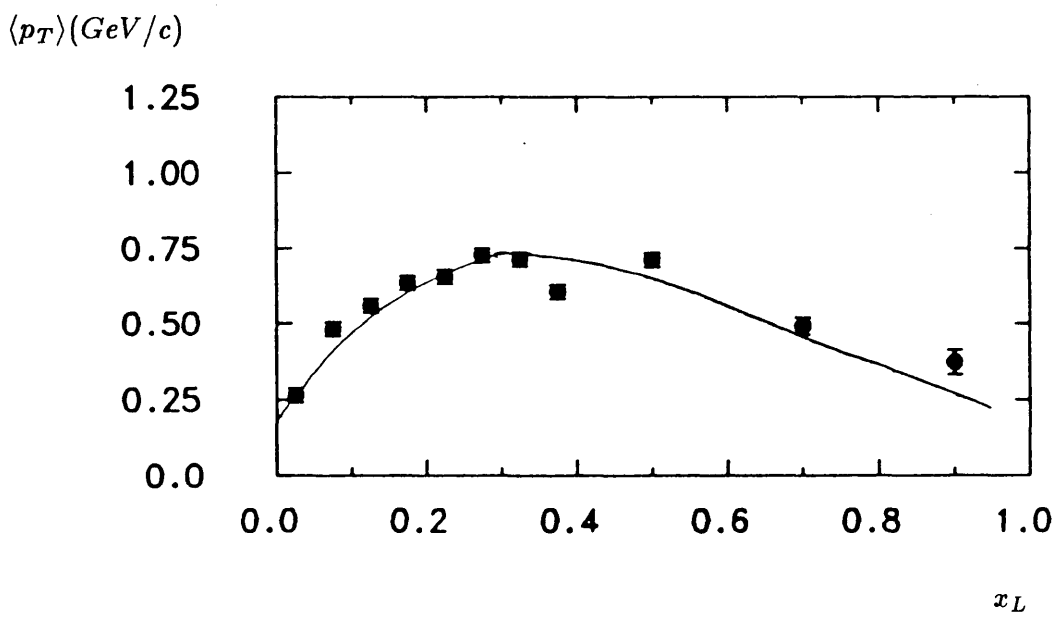

Figure 5.13 : The average transverse momentum as a function of the fractional longitudinal momentum with respect to the jet axis, using the sphericity axis. The solid line show the prediction of the QCD LUND model using standard parameters.

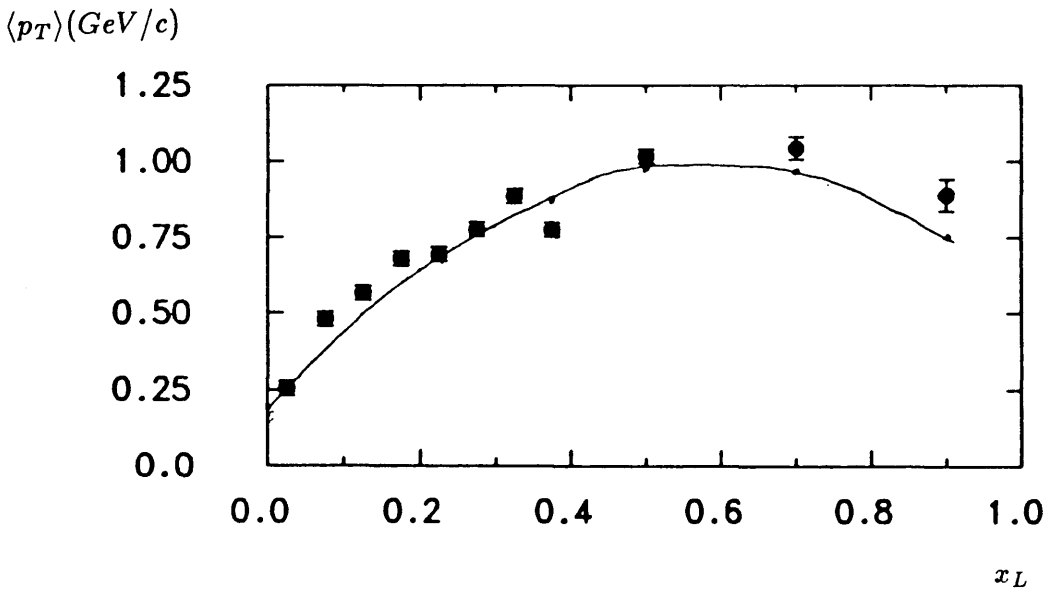

Figure 5.14 : The average transverse momentum as a function of the fractional longitudinal momentum with respect to the jet axis, using the thrust axis. The solid line show the prediction of the QCD LUND model using standard parameters.

difference in $\langle p_T \rangle$ of 0.25 GeV/c at $x_L = 0.5$ implies that there is an angle of 1.3° between the two axes. The $\langle p_T \rangle$ versus x_L figures follow the pattern of having a minimum near $x_L = 0$, then a broad maximum approximately between $x_L = 0.1$ and $x_L = 0.4$ with a gradual decrease as $x_L \rightarrow 1.0$. The transverse momentum should approach zero as x_L approaches 1 from kinematical constraints, that is, the axis is strongly weighted by the high x_L tracks and so these have small values of p_T. However, there is no kinematic constraint to limit $\langle p_T \rangle$ at $x_L = 0$.

(g) Rapidity. As mentioned earlier, the rapidity provides a method of analysing the particle production along the jet axis. The rapidity distribution is shown in figure 5.15, with the data folded around $y = 0$. At small values of y, the rapidity distribution is flat, with a plateau region extending from $y = 0$ to $y = 2$. The particle yield then decreases sharply as the value of y increases away from the flat region. The fact that all the charged particles were assumed to be pions will affect the region close to the maximum value of the rapidity. This is because particles that are in fact kaons or protons will have values of y that are larger than the correct values. The dependence of $\langle p_T \rangle$ on rapidity can also be examined in a similar manner to the variation of this quantity on x_L as described above. The result is shown in figure 5.16, with the $\langle p_T \rangle$ being calculated with respect to the sphericity axis. The minima around zero is less pronounced than in figure 5.13.

(h) Topological event measures. The shape of an event can be studied using the two event measures $\langle p^2_{Tin} \rangle$ and $\langle p^2_{Tout} \rangle$, in addition to the jet measures discussed in section (c). These two quantities are plotted in figures 17 and 18, respectively. It can be seen from these two distributions that the $\langle p^2_{Tin} \rangle$ distribution extends up to a higher value of $\langle p^2_T \rangle$ than the $\langle p^2_{Tout} \rangle$ figure. This indicates that most of the hadronic events occurring at this energy are planar in nature, since the $\langle p^2_{Tout} \rangle$ distribution has such a short

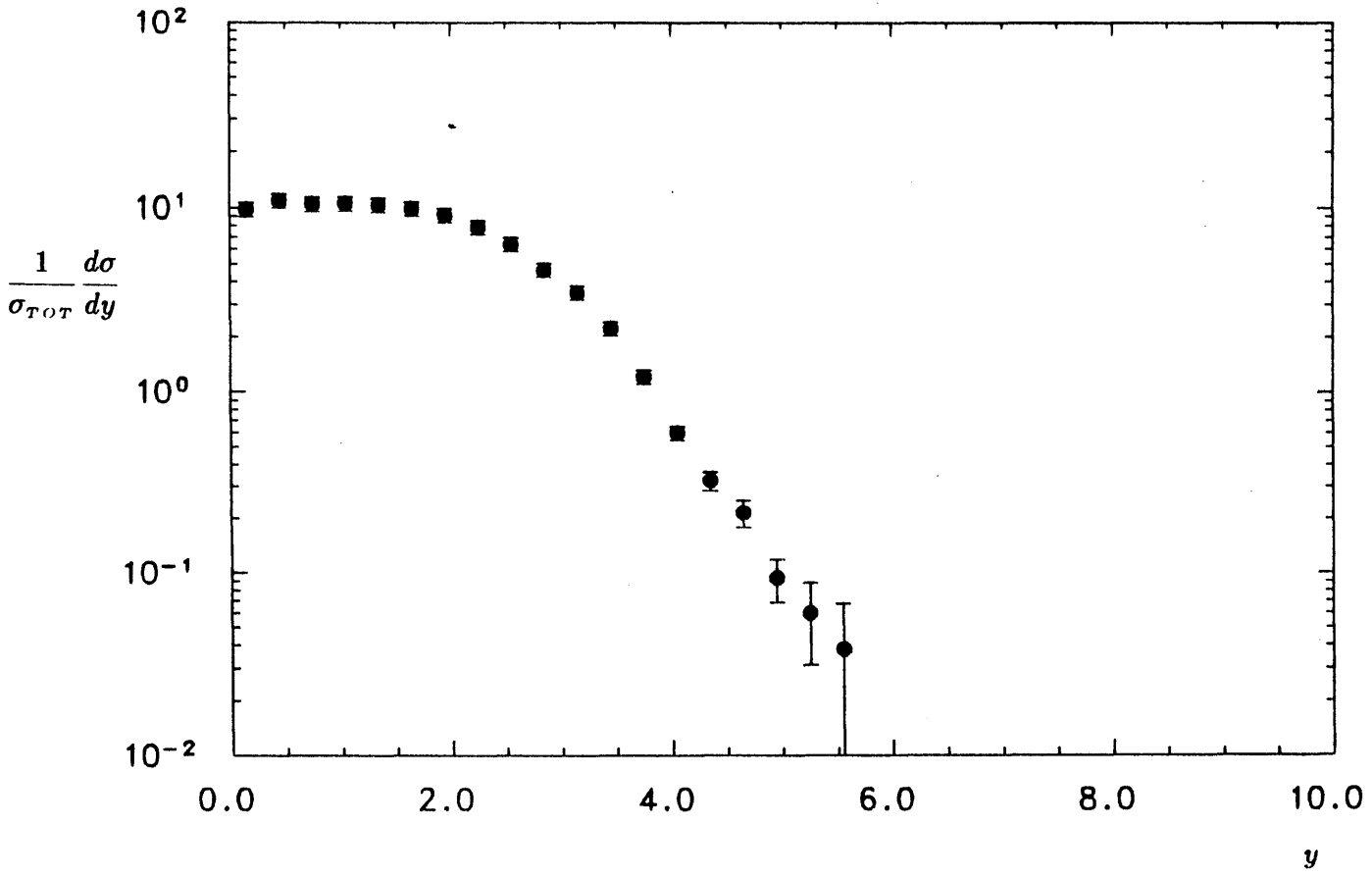

Figure 5.15 : The rapidity spectrum

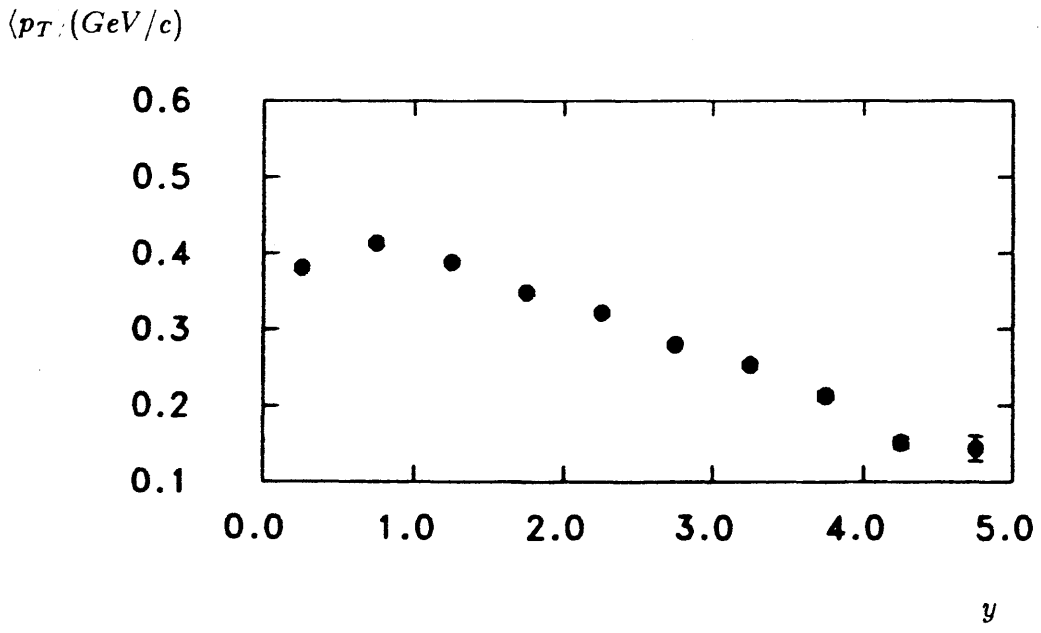

Figure 5.16 : The average transverse momentum as a function of the rapidity, using the sphericity axis as the jet axis

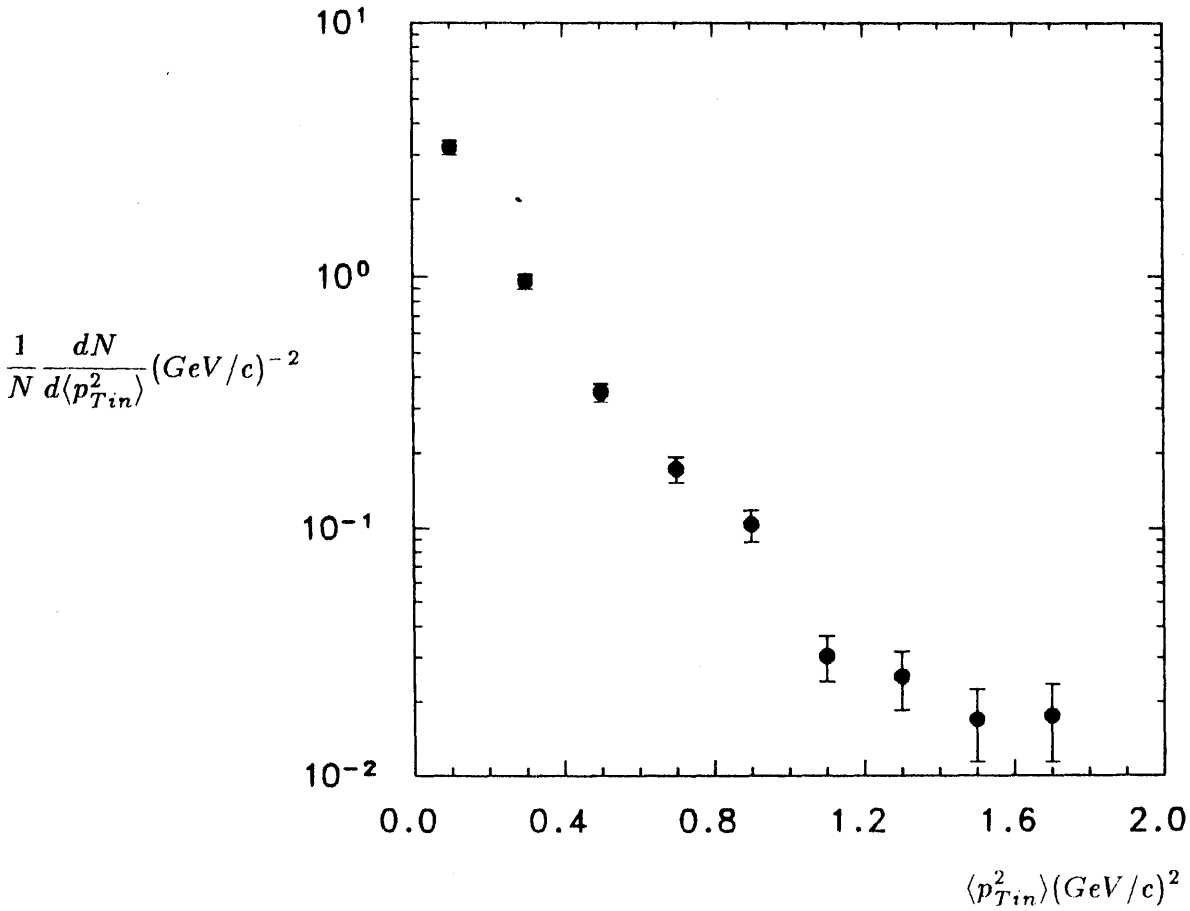

Figure 5.17 : The distribution of the transverse momentum squared in the event plane, averaged over the event

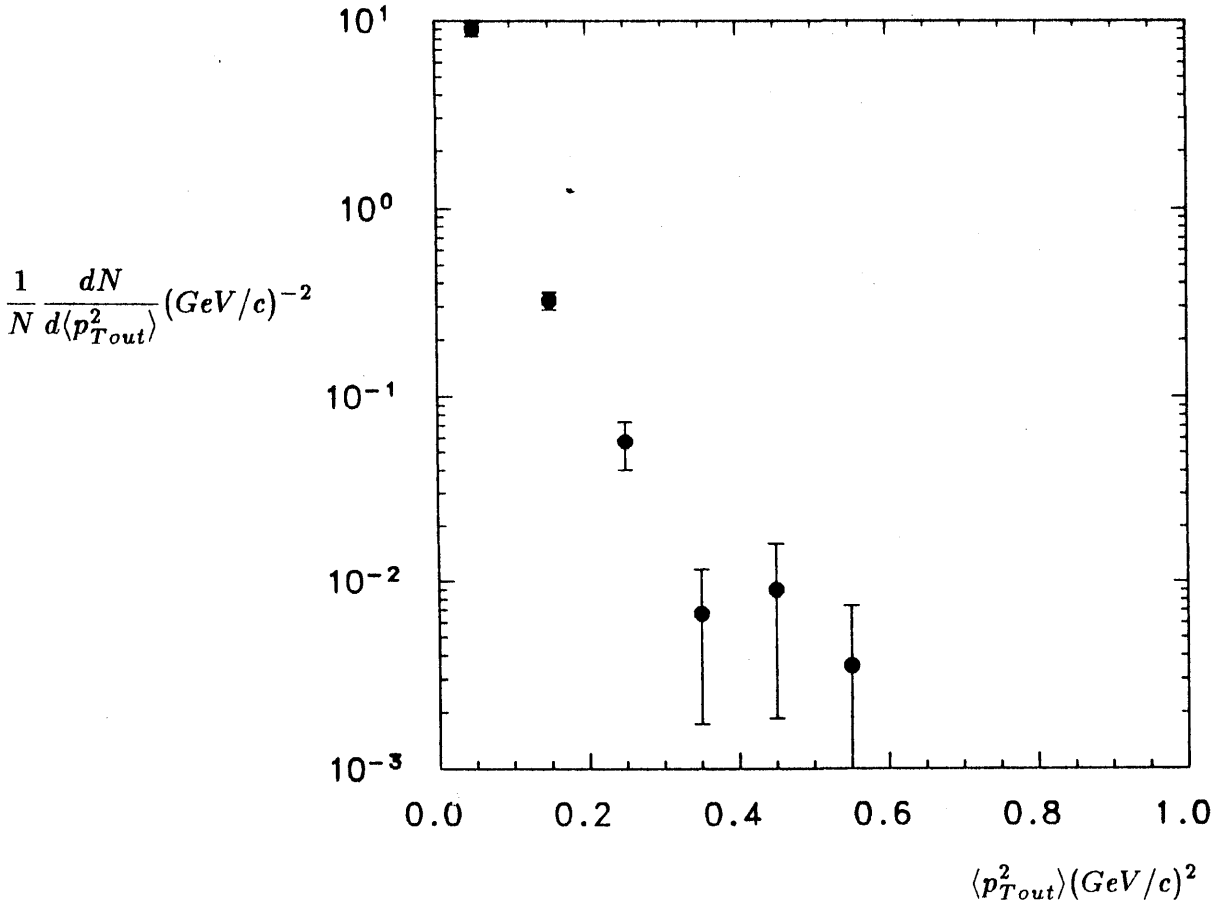

Figure 5.18 : The distribution of the transverse momentum squared out of the event plane, averaged over the event

tail.

(i) Energy energy correlation. The energy energy correlation was calculated using both the charged and selected neutral particles. The bin width $\Delta\chi$ was chosen to be 3.6°. Figure 5.19 shows the energy energy correlation, with self-correlations removed. The predominance of two-jet events can be seen from the two peaks, with the occurrence of soft gluon bremsstrahlung causing one peak to be higher than the other. The energy energy correlation asymmetry is shown in figure 5.20, and this indicates that there is a contribution to the events from hard noncollinear gluon radiation.

5.7 Summary

It is apparent from the many figures shown above that the majority of hadronic events are two-jet like in nature. In addition, the effects of QCD can be seen in the tails of some distributions. Thus, some of the events are shown to consist of three jets of particles, either as a result of hard or soft gluon bremsstrahlung. The results on the angular distributions of the jet axes support the theory that the underlying process is mainly half integer spin quark pair production.

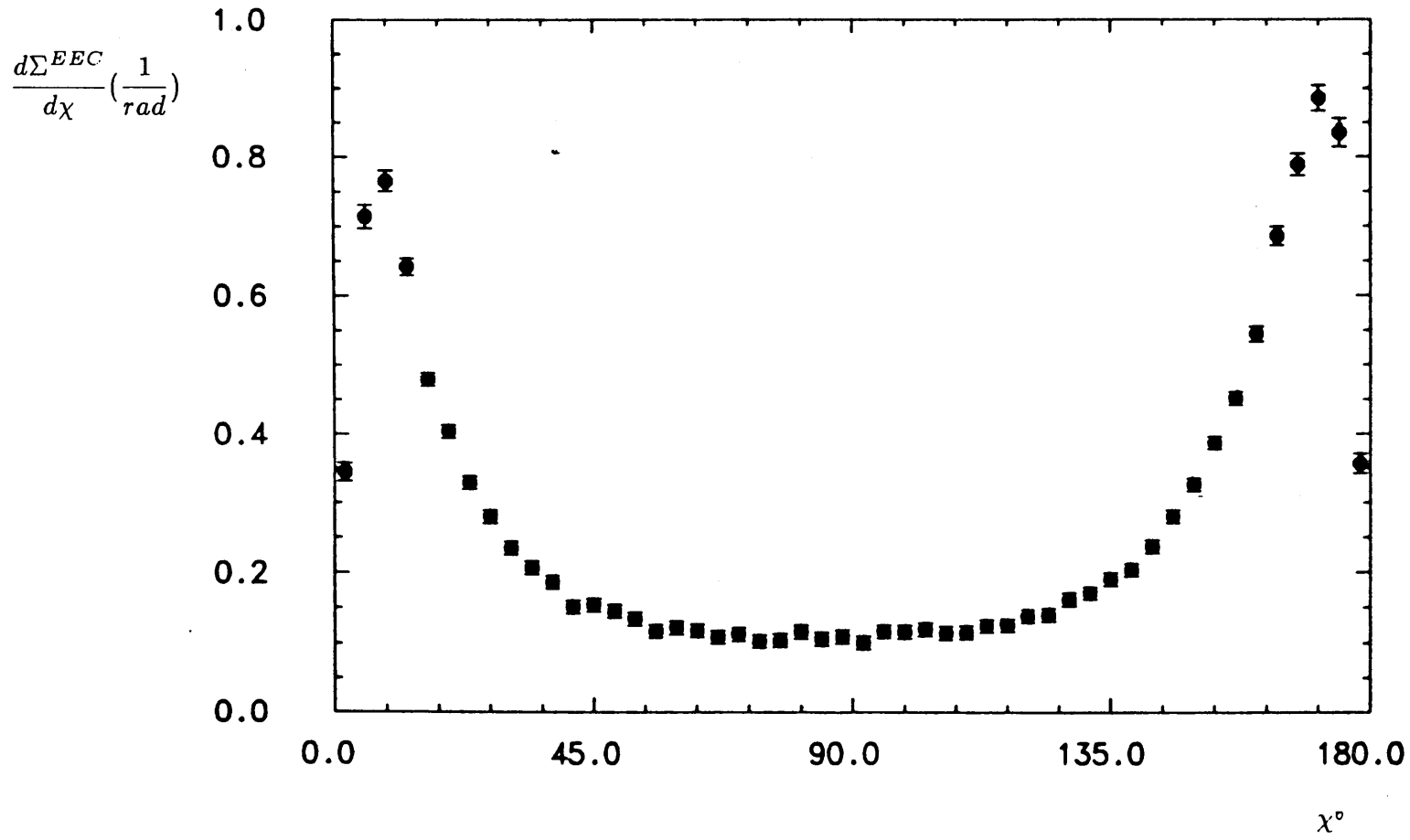

Figure 5.19 : The energy-energy correlation distribution

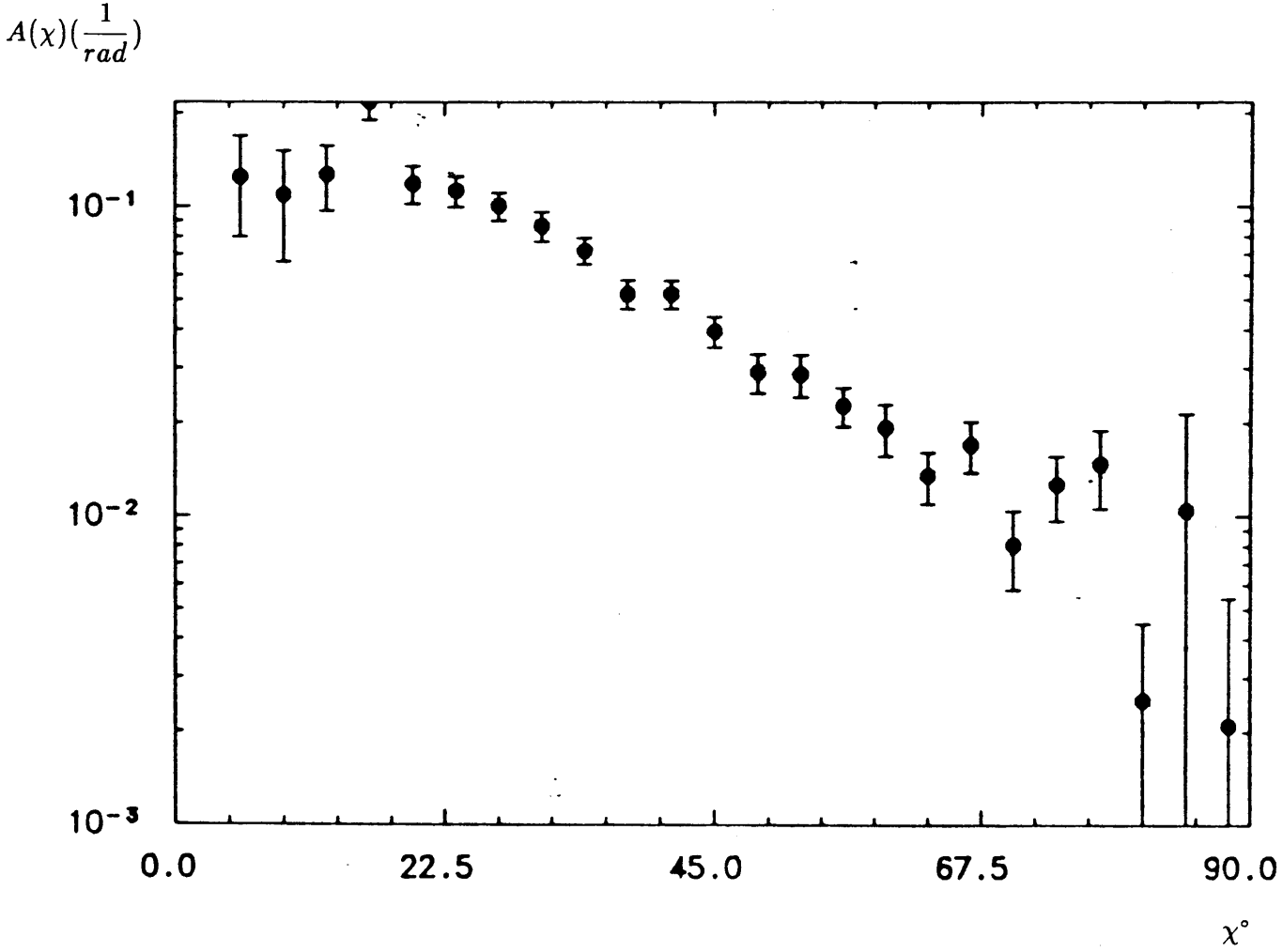

Figure 5.20 : The energy-energy correlation asymmetry distribution

CHAPTER SIX

DETERMINATION OF α_S

6.1 Introduction

As has been mentioned in chapter 2, the observation of three-jet events in e^+e^- annihilation into hadrons at a high centre of mass energy has provided direct evidence for gluon bremsstrahlung as predicted by QCD. A measurement of the three-jet cross section should therefore lead to a determination of α_S, since the strong coupling constant is directly proportional to the rate of three-jet events, provided the four-jet rate is not large. Obtaining a value of α_S from the data is however, made difficult by the fact that the QCD prediction is made at the parton level. Thus, the QCD calculation has to be combined with a model, which describes the fragmentation of quarks and gluons into hadrons. In this analysis, the LUND string model of fragmentation was chosen, for the reasons outlined in chapter 2. The use of only one fragmentation model should result in a reduced systematic uncertainty on the value of α_S. This is because different fragmentation schemes give a range of values of α_S as explained in chapter 2, and this effect has been found by the MARK J, CELLO and JADE collaborations to be the biggest source of systematic error. The α_S used in this analysis is that defined in the $(\overline{ms})$ scheme.

6.2 Procedure

The first stage in this analysis was to generate Monte Carlo events which could be compared with the corrected data. The Monte Carlo events were generated using the LUND Monte Carlo-JETSET version 5.2. The input parameters of the Monte Carlo were those determined in the previous chapter, apart from the value of α_S.

The data were corrected for the acceptance of the detector and for initial state photon radiation according to the prescription given in chapter 5. Thus, the various distributions could be compared directly with the properties of the hadrons generated by the Monte Carlo.

Several sets of Monte Carlo events were generated, each with a different input value of α_S. The values of α_S that were chosen covered a wide range and encompassed the values of α_S determined by other collaborations. Approximately 50,000 events were generated for each value of α_S, and this corresponds to ~ 10 times the number of accepted multihadrons in the data sample.

Thus, for each distribution investigated, the corrected data was compared with the several sets of Monte Carlo. The comparison between the data and the Monte Carlo yielded a χ^2 value for each value of α_S per histogram. A plot of χ^2 versus α_S could then be drawn for each distribution, and hence the position of minimum χ^2 could be found. Thus, the value of α_S that best described the corrected data at a centre of mass energy of 44 GeV could be calculated.

6.3 Results

The above procedure was carried out for several distributions, all of which were presented in chapter 5, apart from Q_2 and Q_3, two of the eigenvalues of the momentum tensor defined in chapter 1. The distributions were chosen since they are variables that are sensitive to the shape of an event, and hence to three-jet events. The exception to this is the energy energy correlation asymmetry, which was used because of its sensitivity to α_S, as discussed in the previous chapter.

It should be noted that only the large angle region, $\chi > 50°$, of the

energy energy correlation asymmetry was used to calculate α_S. This region of the energy energy correlation asymmetry is calculated from the section of the energy energy correlation (see figure 5.19) between $\chi = 50°$ and $\chi = 130°$. The determination of the value of α_S uses this area of the energy energy correlation asymmetry distribution because, at large angles, the energy energy correlation asymmetry is insensitive to the value of Y_{min}. This is because the value of Y_{min} is of greater importance in the case of two particles which are close together in χ, rather than in the case where the angle χ separating the particles is between 50° and 130°. This fact can be seen from the definition of Y_{min} given in chapter 5. Thus, using this half of the plot introduces less systematic errors into the value of α_S since the figure is not dependent on an artificial procedure for differentiating between two and three jet events.

The results are shown in table 6.1.

As can be seen from the table, the shape variables give compatible values of α_S. The value of α_S obtained from using the energy energy correlation asymmetry is smaller, but is still compatible with the other values of α_S, if systematic errors are taken into account.

The values of α_S found in this analysis should only be compared with the results of other experiments if those experiments were also carried out at a beam energy of 22 GeV. This is because of the 'running' nature of α_S as described in section 1.7 and embodied analytically in equation (1-3). Thus, the value of α_S which was obtained using the energy energy correlation asymmetry can be compared directly with the MARK-J group's result. The values of α_S obtained by both experiments are compatible within experimental errors, although the MARK-J result was obtained by taking the average of the string and independent fragmentation models. This is in contrast with the method employed in this study, which was to

eliminate the independent fragmentation model because of its theoretical limitations and its failure to describe accurately the experimental data of several collaborations. Thus, the systematic error on the value of α_S is smaller in this analysis for the reasons outlined in this chapter.

The value of α_S found in this work is in agreement with the results of table 2.3 (other experiments' determinations of α_S using the energy energy correlation asymmetry) but with a substantially lower systematic error. It should, however, be noted that the results of table 2.3 were obtained from experiments performed at a beam energy of 17 GeV.

Thus, it can be seen that one of the main aims of this work has been achieved, namely, the determination of the strong interaction coupling constant, α_S, at the highest currently available beam energy with a low systematic error.

Several possible sources of systematic error were investigated and evaluated. The first of these was the possible error introduced into the analysis by an incorrect choice of the parameters that were used in the LUND Monte Carlo. The magnitude of this systematic error was evaluated by changing the values of the input Monte Carlo parameters in such a way that the corrected distributions, that were used for the tuning procedure, were still described by the Monte Carlo at the generator level. This procedure was therefore an attempt to take into account the errors quoted for the TASSO and JADE corrected distributions. It was found that the systematic errors from this source are larger in the determination of α_S using the shape variables. This is essentially because the shape variables are more sensitive to the tuning of the Monte Carlo than is the energy energy correlation asymmetry as mentioned above. Hence, the measurement of α_S using the energy energy correlation asymmetry is the most accurate and reliable of the values presented in this chapter.

Fitted Distribution	Value of α_S	χ^2/d.f. at minimum
Sphericity	0.175 ± 0.015 ± 0.015	4.2/6
Thrust	0.164 ± 0.015 ± 0.015	13/6
Q_2	0.169 ± 0.015 ± 0.015	7.9/8
$\langle k_T^2{}_{in} \rangle$	0.180 ± 0.015 ± 0.015	12/9
Q_3	0.169 ± 0.015 ± 0.015	4.6/9
Asymmetry	0.152 ± 0.015 ± 0.010	5.1/5

Table 6.1 : The values of α_S that were calculated using the CELLO corrected data at W = 44 GeV.

Note:- The first error in the value of α_S is the statistical error and the second error is the systematic error.

The second source of systematic error that was examined was the procedure used to select the multihadronic data sample. An additional sample of multihadrons was obtained using a different set of selection criteria in order to check that there was no bias in the original data sample. This second selection procedure permitted each event to have a smaller total visible energy, for the event to be accepted. Hence, this second selection contained $\sim$ 10 % more multihadronic events. The value of α_S was then determined in an identical manner to that which was used for the first data sample. The magnitude of this systematic error was then found to be $\sim$ 10 %.

In order to investigate whether the CELLO corrected data at 44 GeV could be described by QCD, the distributions of chapter 5 were compared with the QCD model, using an α_S value of 0.16. Figures 6.1-6.7 show the results of this comparison, which confirms that a value of α_S at 44 GeV of 0.16 describes the essential features of the data obtained with the CELLO detector.

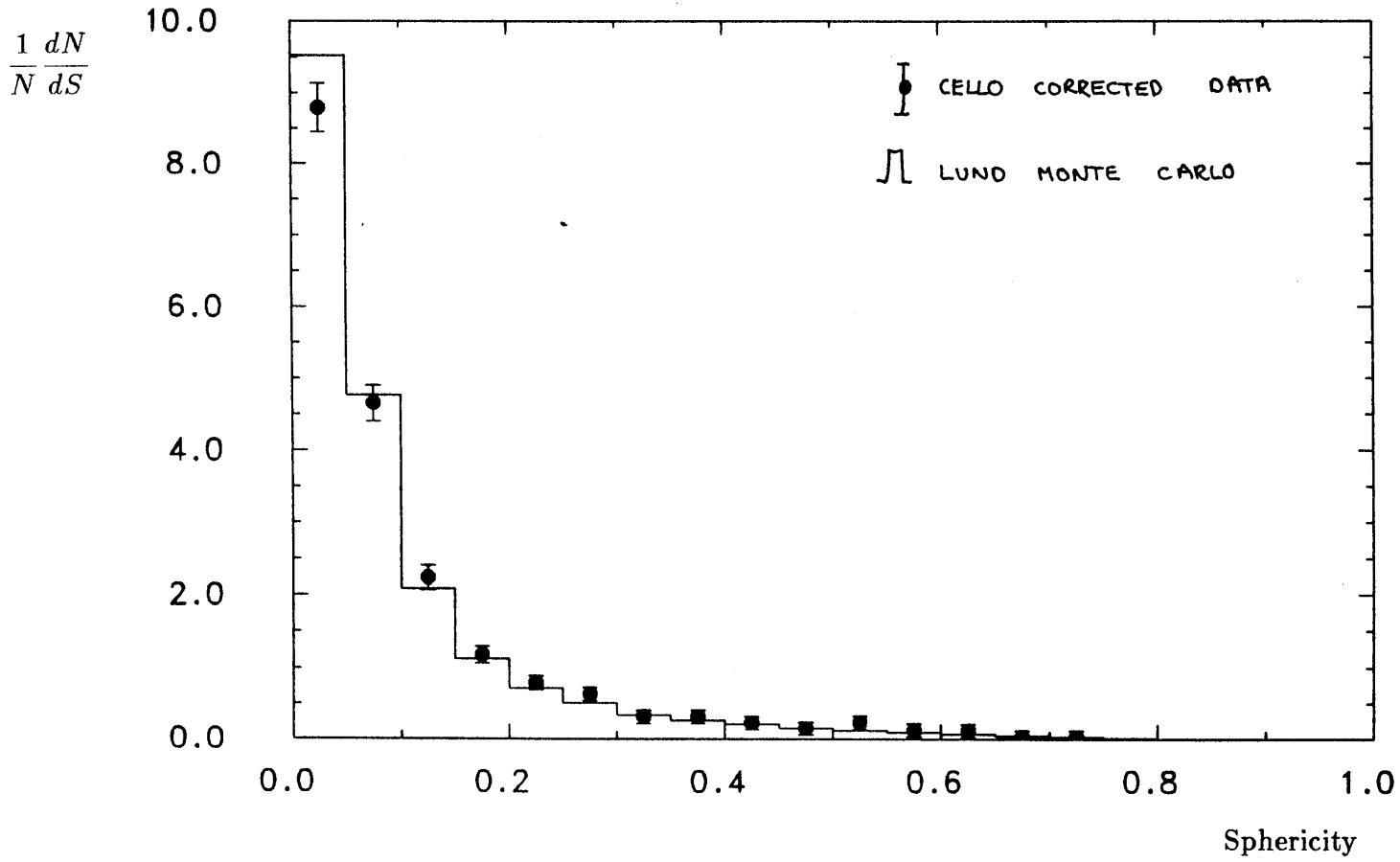

Figure 6.1 : Comparison between CELLO corrected data at W=44 GeV and the LUND Monte Carlo for the normalised sphericity distribution

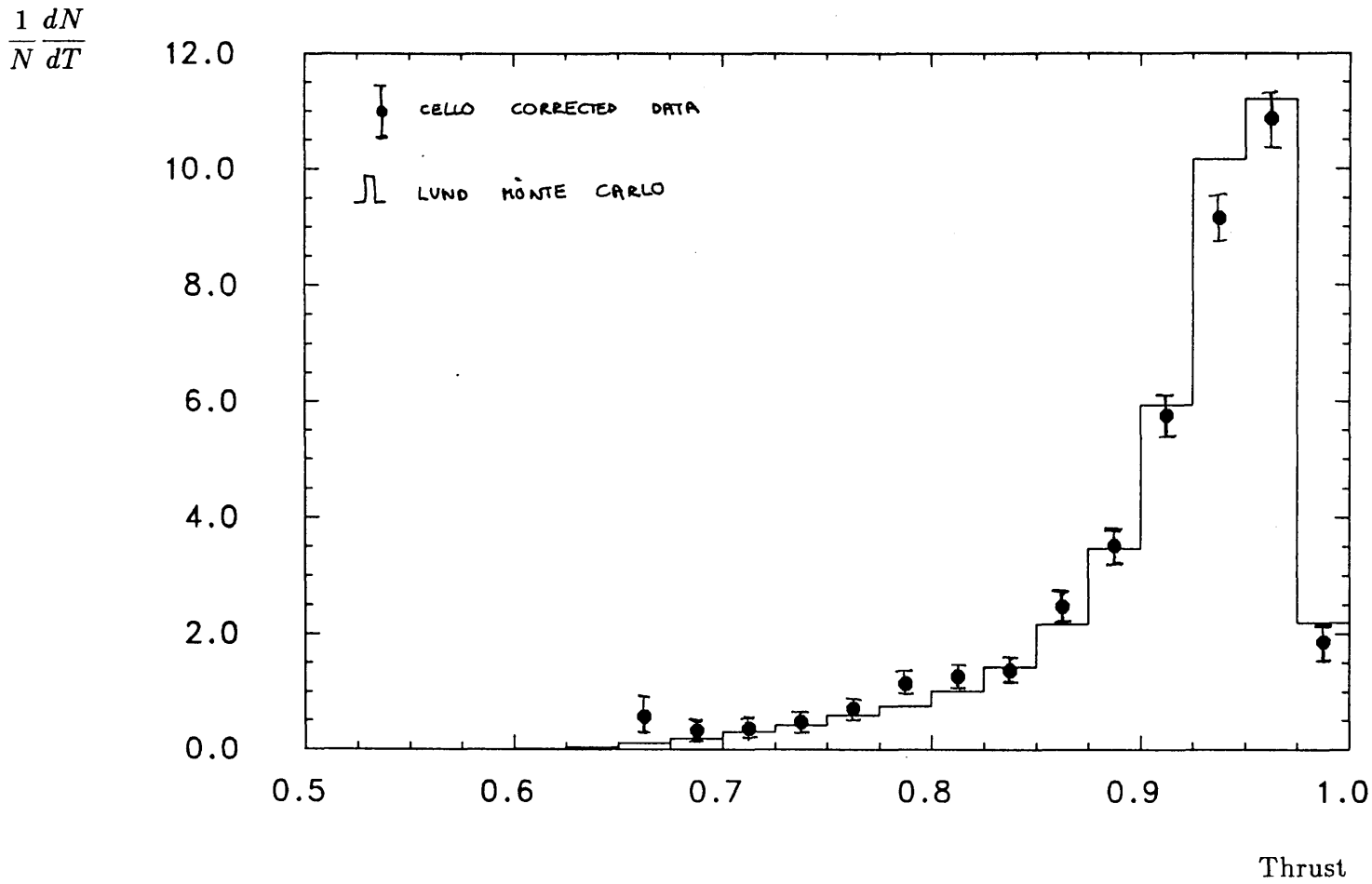

Figure 6.2 : Comparison between CELLO corrected data at W=44 GeV and the LUND Monte Carlo for the normalised thrust distribution

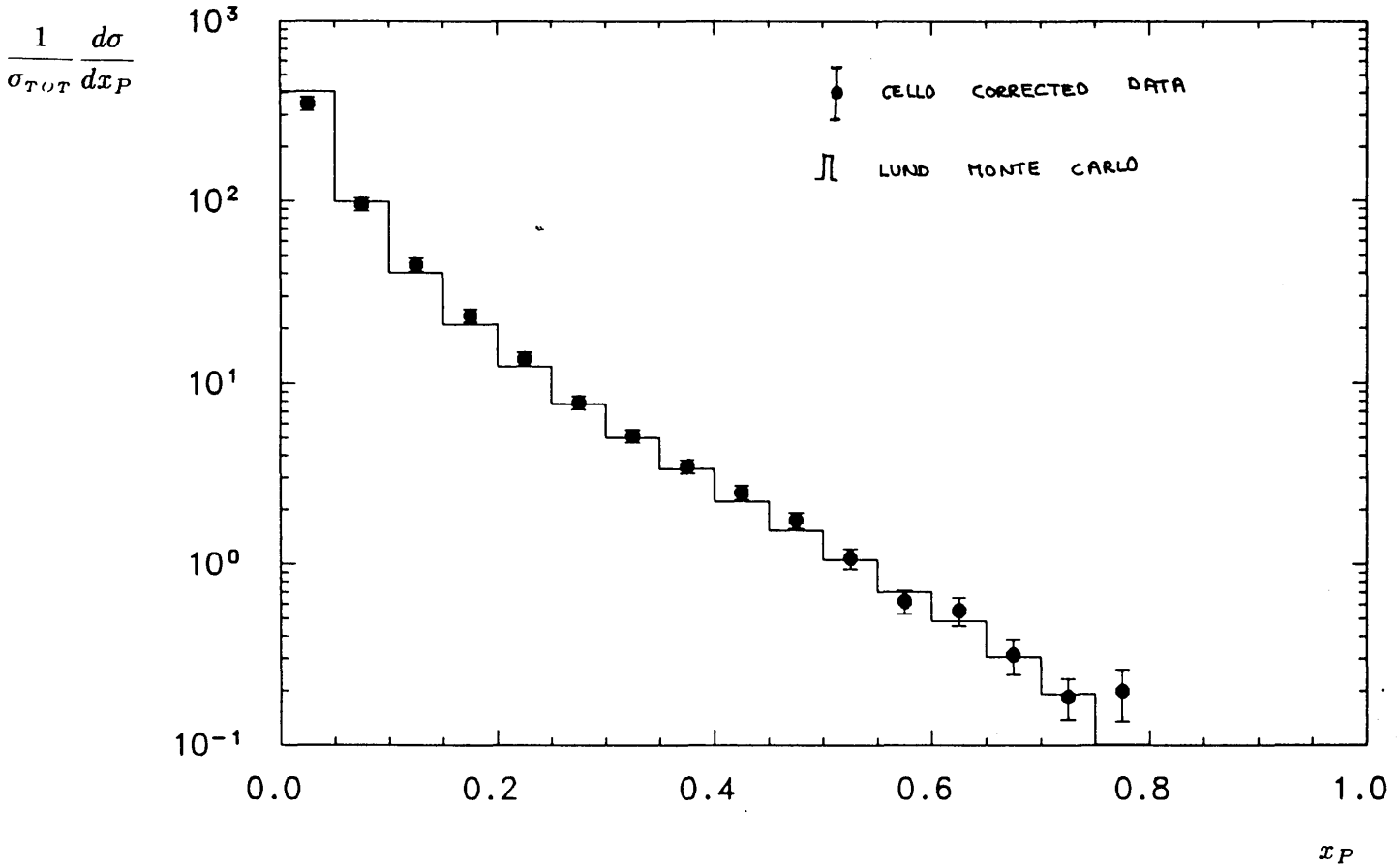

Figure 6.3 : Comparison between CELLO corrected data at W=44 GeV and the LUND Monte Carlo for the normalised fractional particle momentum spectrum

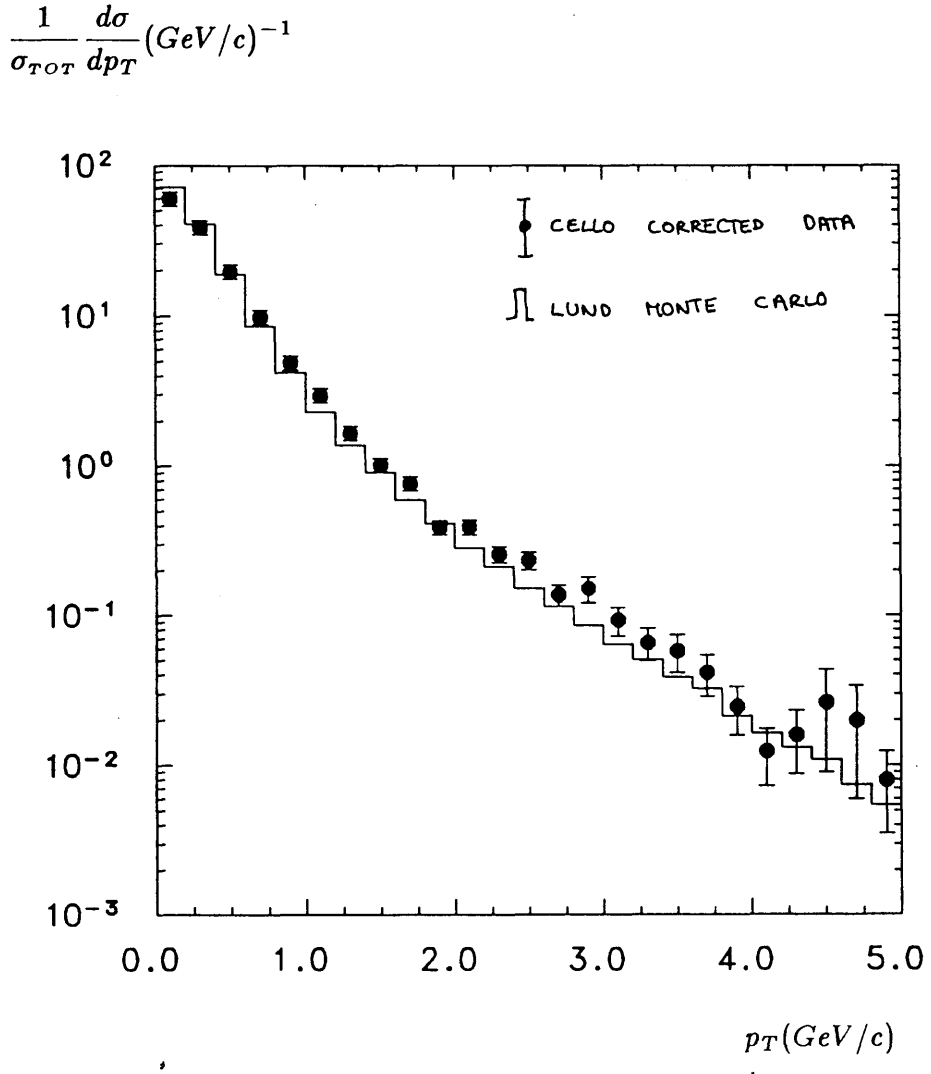

Figure 6.4 : Comparison between CELLO corrected data at W=44 GeV and the LUND Monte Carlo for the normalised transverse momentum distribution

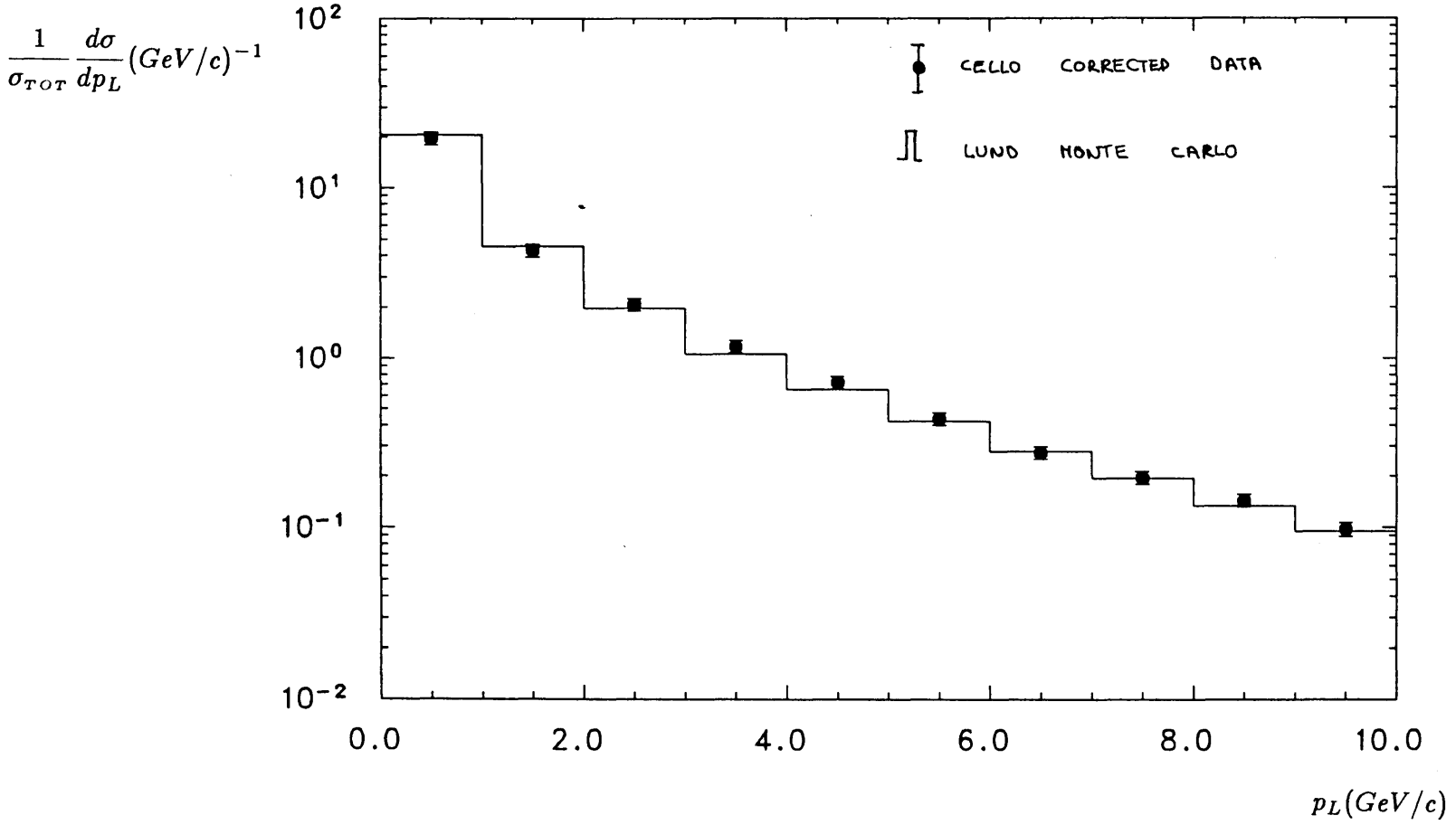

Figure 6.5 : Comparison between CELLO corrected data at W=44 GeV and the LUND Monte Carlo for the normalised longitudinal momentum distribution

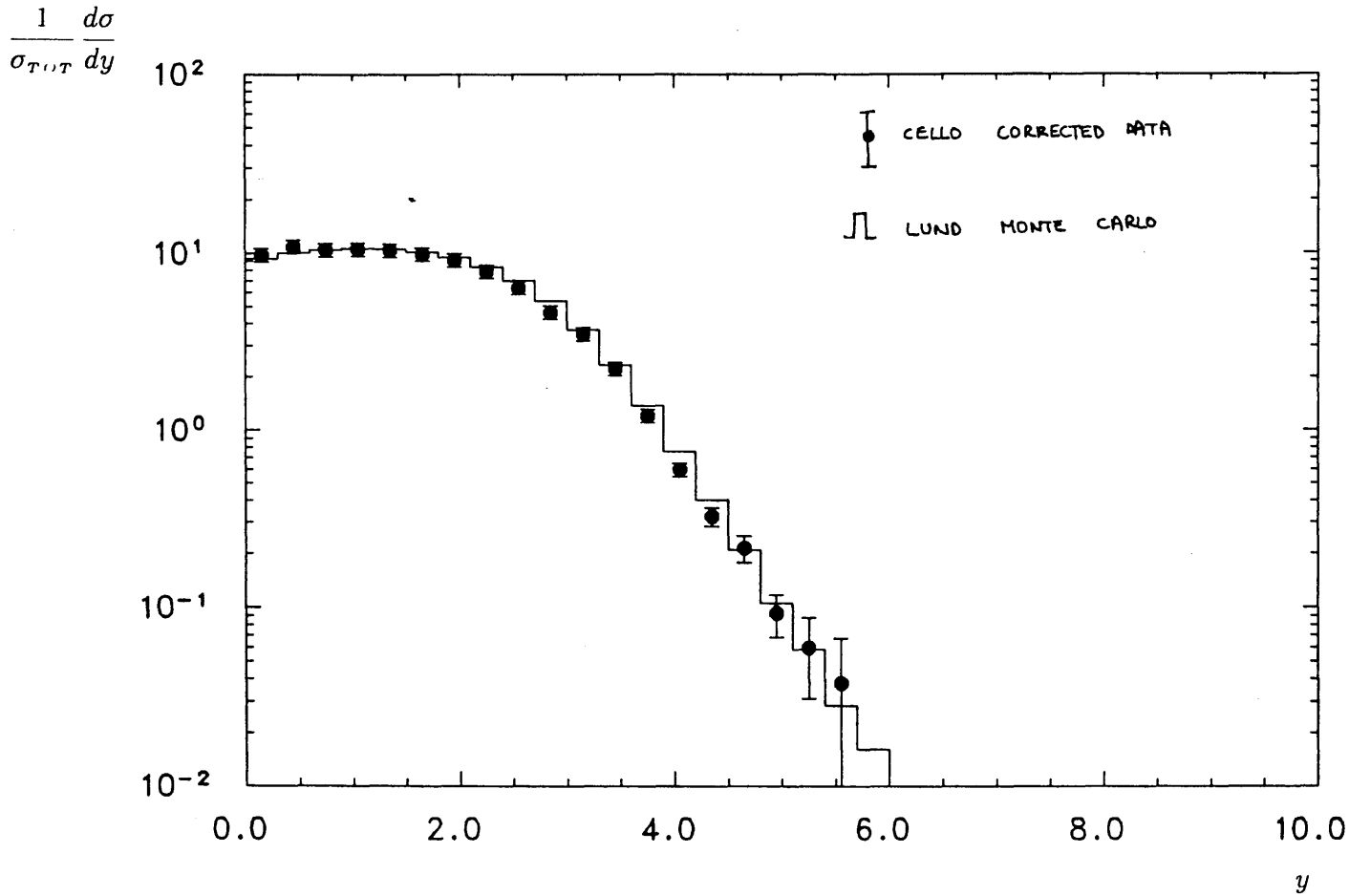

Figure 6.6 : Comparison between CELLO corrected data at W=44 GeV and the LUND Monte Carlo for the normalised rapidity distribution

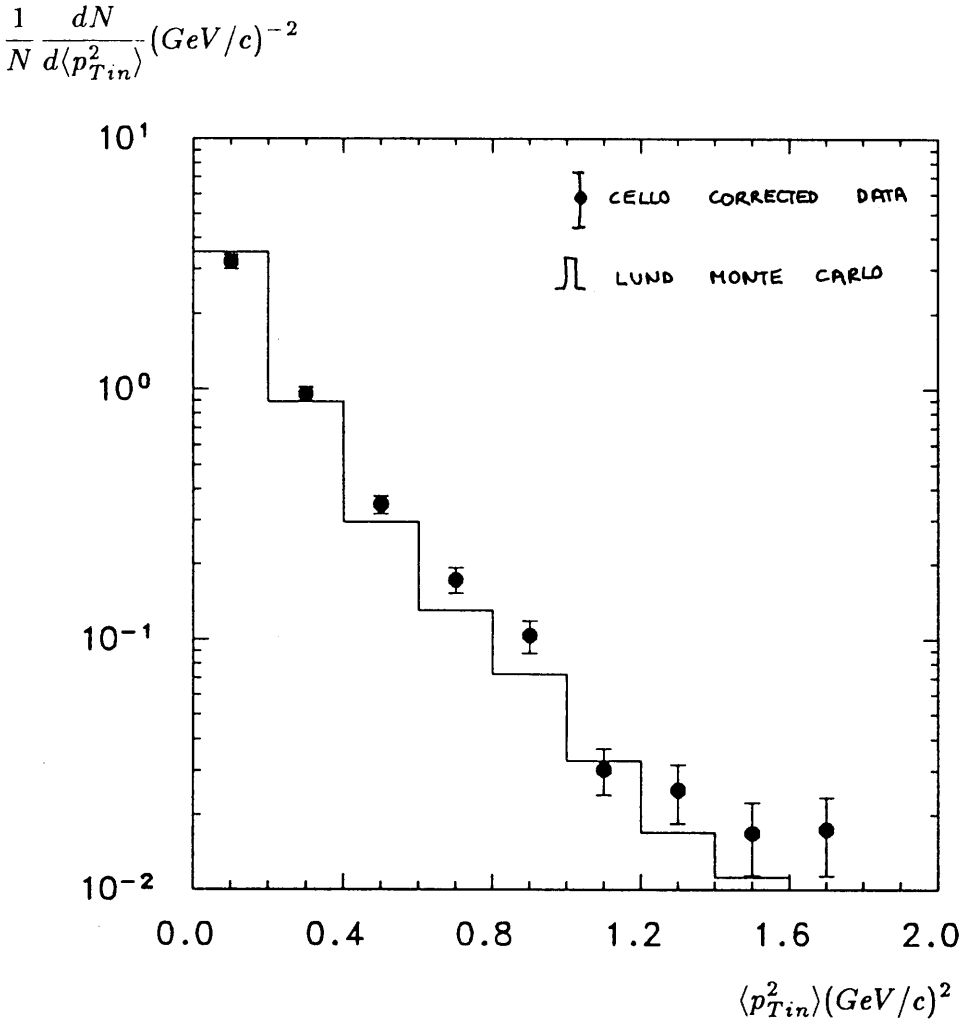

Figure 6.7 : Comparison between CELLO corrected data at W=44 GeV and the LUND Monte Carlo for the normalised transverse momentum squared in the event plane averaged over the event

CHAPTER SEVEN

SUMMARY AND CONCLUSIONS

In the first chapter of this thesis, an introduction was given into the theory of quantum chromodynamics (or QCD); the theory which attempts to describe the interaction of elementary particles through the exchange of gluons.

The experimental evidence that QCD is a plausible theory to describe the strong interaction was outlined in chapter 2. The second chapter also showed that in order to describe the experimental results from e^+e^- annihilation, a model to describe the fragmentation of the quarks and gluons is needed, in conjunction with QCD perturbation theory. The relative merits of several types of fragmentation models were considered from the conceptual point of view and from the models' ability to describe the main features of the data. This procedure led to the LUND string model of fragmentation being used in the second results chapter to determine the value of α_S. A brief summary and evaluation of previous attempts to determine α_S was also given in chapter 2, with the main conclusion being that the systematic error on the value of α_S was large. This was because of the uncertainties in the analysis procedure brought about by the various fragmentation models which gave different results for the value of α_S. The choice of the LUND fragmentation model for this study was intended to reduce this source of systematic error.

The main features of the detector were summarised in chapter 3, with particular emphasis on the CELLO detector's suitability for detecting multihadronic events.

A description of the data acquisition chain and the means whereby multihadronic events were separated from background events was given in chapter 4. It was found that after selection cuts had been made, the number

of background events was negligible. This result was found after visually scanning the multihadronic events and using extensive Monte Carlo techniques. Thus, after this procedure, which is explained in greater detail in chapter 4, a sample of multihadronic events was obtained which was relatively free of events originating from background processes.

The first results chapter described the procedure for obtaining distributions of the corrected data. This method was shown to be valid since, after some more specialised cuts, in particular those used to ensure well-measured photons, the agreement between the data and the Monte Carlo was good. Corrected data distributions for a large number of variables were then presented. These variables were chosen in order to ascertain if the data could be described by the theory of QCD. It was shown in chapter 5 that the main features of the data, such as the preponderance of two-jet events or the half integer spin nature of the interacting particles were in agreement with the predictions of QCD. Several of the distributions plotted, for example, the energy energy correlation asymmetry, show that there is a contribution to the multihadronic event sample from hard non-collinear gluon radiation. This process, together with soft gluon bremsstrahlung, results in the production of three-jet events, the evidence for which can be seen in the tails of many distributions, such as the p_T distribution. Thus it was shown that the corrected data obtained with the CELLO detector at a centre-of-mass energy of 44 GeV was in agreement with QCD for the variables used for this study.

In chapter 6, a method of determining the value of α_S was outlined in which the most reliable and well tested fragmentation model was used. This technique was used for several variables, all of which were chosen because of their sensitivity to the value of α_S. The energy energy correlation asymmetry gave the most accurate result because of its low systematic error, the

reasons for which are given in the second results chapter.

The final part of the work presented here was to compare the CELLO corrected data at a centre-of-mass energy of 44 GeV with QCD predictions using the value of α_S obtained in chapter 6. It was shown that the QCD predictions agreed well with the CELLO corrected distributions that were investigated.

Thus, it can be seen that the corrected multihadronic data collected with the CELLO detector at a centre-of-mass energy of 44 GeV can be well described by quantum chromodynamics.

CELLO Collaboration

H.-J. Behrend, J. Bürger, L. Criegee, J.B. Dainton [1], H. Fenner, J.H. Field, G. Franke, J. Fuster [2], Y. Holler, J. Meyer, V. Schröder, H. Sindt, U. Timm, G.G. Winter, W. Zimmermann

Deutsches Elektronen-Synchrotron, DESY, Hamburg, Germany

P.J. Bussey, C. Buttar, A.J. Campbell, D. Hendry, G. McCurrach, J.M. Scarr, I.O. Skillicorn, K.M. Smith

University of Glasgow, United Kingdom

J. Ahme, V. Blobel, M. Feindt, J. Harjes, M. Poppe, H. Spitzer

II. Institut für Experimentalphysik, Universität Hamburg, Germany

W.-D. Apel, A. Böhrer, J. Engler, G. Flügge, D.C. Fries, W. Fues, K. Gamerdinger, P. Grosse-Wiesmann [3], J. Hansmeyer, G. Hopp, H. Jung, J. Knapp, M. Krüger, H. Küster, P. Mayer, H. Müller, K.H. Ranitzsch, H. Schneider, J. Wolf

Kernforschungszentrum Karlsruhe und Universität Karlsruhe, Germany

W. de Boer, G. Buschhorn, G. Grindhammer, B. Gunderson, Ch. Kiesling, R. Kotthaus, H. Kroha, D. Lüers, H. Oberlack, B. Sack, P. Schacht, G. Shooshtari, W. Wiedenmann

Max-Planck-Institut für Physik und Astrophysik, München, Germany

A. Cordier, M. Davier, D. Fournier, M. Gaillard [4], J.F. Grivaz, J. Haissinski, P. Janot, V. Journé, F. Le Diberder, E. Ros [5], A. Spadafora, J.-J. Veillet

Laboratoire de l'Accélérateur Linéaire, Orsay, France

B. Fatah [6], R. George, M. Goldberg, O. Hamon, F. Kapusta, F. Kovacs, L. Poggioli, M. Rivoal

Laboratoire de Physique Nucléaire et Hautes Energies, Université de Paris, France

G. d'Agostini, F. Ferrarotto, M. Gaspero, B. Stella

University of Rome and INFN, Italy

R. Aleksan, G. Cozzika, Y. Ducros, Y. Lavagne, F. Ould Saada, J. Pamela, F. Pierre, J. Žáček [7]

Centre d'Études Nucléaires, Saclay, France

G. Alexander, G. Bella, Y. Gnat, J. Grunhaus, A. Levy

Tel Aviv University, Israel

---

[1] Permanent address: University of Liverpool, United Kingdom

[2] On leave of absence from Inst. de Fisica Corpuscular, Universidad de Valencia, Spain

[3] Now at Stanford Linear Accelerator Center, USA

[4] Now at Stanford Linear Accelerator Center, USA

[5] Now at Universidad Autónoma de Madrid, Spain

[6] Now at University of Sebha, Physics Department, Libya

[7] Now at Nuclear Center, Charles University, Prague, Czechoslovakia

1. S. L. Glashow, Nucl. Phys. **22** (1961), p. 579.

2. S. Weinberg, Phys. Rev. Lett. **19** (1967), p. 1264.

3. A. Salam, Phys. Rev. **184** (1969), p. 1750.

4. M. Kobayashi et al., Prog. Theor. Phys. **49** (1972), p. 282.

5. J. D. Bjorken, Proc. 3rd Int. Symp. on Electron and Photon Interactions, Stanford (1967).

R. P. Feynman, Phys. Rev. Lett. **23** (1969), 1415–1417.

J. D. Bjorken et al., Phys. Rev. **185** (1969), 1975–1982.

6. O. W. Greenberg, Phys. Rev. Lett. **13** (1964), 598–602.

7. R. C. Mills et al., Phys. Rev. **96** (1954), 191–195.

8. G. 't Hooft et al, Nucl. Phys. B **44** (1972), 189–213.

9. K. Fabricius et al., Phys. Lett. **97B** (1980), p. 431; *II*, Z. Phys. C **11** (1982), p. 315.

10. R. K. Ellis et al., Phys. Lett. **45B** (1980), p. 1226; Nucl. Phys. B **178** (1980), p. 421.

11. J. Vermaseren et al., Nucl. Phys. B. **187** (1981), p. 301.

12. T. D. Gottschalk et al., Phys. Lett. **150B** (1985), 451–454.

13. M. R. Pennington, Reports on Progress in Physics **46** (1983), 393–513.

14. J. D. Bjorken et al., Phys. Rev. **D1** (1970), p. 1416.

15. S. Brandt et al., Phys. Lett. **12** (1964), p. 57.

E. Fahri, Phys. Rev. Lett. **39** (1977), p. 1587.

16. P. Soding et al., Annual Review of Nuclear and Particle Science **31** (1981), 231–294.

17. J. H. de Groot et al., Phys. Lett. **82B** (1979), 456–460; *II*, Z. Phys. C **1** (1979), 143–162.

W. B. Atwood, Proc. 1979 SLAC Summer Institute on Particle Physics (1980), 1–58.

18. D. J. Fox et al., Phys. Rev. Lett. **33** (1974), 1504–1507.

C. Chang et al., Phys. Rev. Lett. **35** (1975), 901–904.

19. D. J. Gross et al., Phys. Rev. Lett. **30** (1973), p. 1343; *II*, Phys. Rev. **D9** (1974), p. 980.

H. Georgi et al., Phys. Rev. **D9** (1974), p. 416.

20. M. Dine et al., Phys. Rev. Lett. **43** (1979), 668–671.

K. G. Chetyrkin et al., Phys. Lett. **85B** (1979), 277–279.

W. Celmaster et al., Phys. Rev. Lett. **44** (1980), 560–564; *II*, Phys. Rev. **D21** (1980), 3112–3128.

21. G. G. Hanson et al., Phys. Rev. Lett. **35** (1975), p. 1609.

22. R. P. Feynman et al., Nucl. Phys. B **136** (1978), p. 1.

23. A. Ali et al., Z. Phys. C **2** (1979), p. 33; *II*, Phys. Lett. **83B** (1979), p. 375; *III*, Phys. Lett. **93B** (1980), p. 155; *IV*, Nucl. Phys. B **168** (1980), p. 409.

24. P. Hoyer et al., Nucl. Phys. B **161** (1979), p. 349.

25. C. Peterson et al., Phys. Rev. **D27** (1983), p. 105.

26. B. Andersson et al., Phys. Lett. **94B** (1980), p. 211; *II*, Z. Phys. C **6** (1980), p. 235; *III*, Nucl. Phys. B **197** (1982), p. 45.

27. G. C. Fox et al., Nucl. Phys. B **168** (1980), p. 285.

R. D. Field et al., Nucl. Phys. B **213** (1983), p. 65.

28. B. R. Webber, Nucl. Phys. B **238** (1984), p. 492.

29. T. D. Gottschalk, Nucl. Phys. B **214** (1983), 201–222; *II*, Nucl. Phys. B **239** (1984), 325–348; *III*, Nucl. Phys. B **239** (1984), 349–381.

30. JADE Collaboration, W. Bartel et al., Phys. Lett. **101B** (1981), p. 129.

31. JADE Collaboration, W. Bartel et al., Z. Phys. C **21** (1983), p. 37; *II*, Phys. Lett. **134B** (1984), p. 275.

32. TPC Collaboration, Phys. Rev. Lett. **54** (1985), p. 270.

33. TASSO Collaboration, R. Brandelik et al, Z Phys. C **26** (1984), p. 157; *II*, Z Phys. C **29** (1985), p. 29.

34. JADE Collaboration, W. Bartel et al, Phys. Lett. **157B** (1985), 340–344.

35. TPC Collaboration, Phys. Rev. Lett. **54** (1985), p. 270; *II*, Z. Phys. C **28** (1985), 31–44.

36. H. Daum et al., Z. Phys. C **8** (1981), p. 167.

37. JADE Collaboration, W. Bartel et al, Proc. 20th Int. Conf. High Energy Physics, New York (1980).

MARK-J Collaboration, D. P. Barber et al, Phys. Lett. **89B** (1979), p. 139; *II*, Proc. 20th Int. Conf. High Energy Physics, New York (1980).

PLUTO Collaboration, Ch. Berger et al, Phys. Lett. **97B** (1980), p. 459.

TASSO Collaboration, R. Brandelik et al, Phys. Lett. **94B** (1980), p. 437.

38. CELLO Collaboration, H.-J. Behrend et al, Nucl. Phys. B **218** (1983), p. 269; *II*, Phys. Lett. **138B** (1984), p. 311.

39. JADE Collaboration, W. Bartel et al, Phys. Lett. **119B** (1982), p. 239.

40. CELLO Collaboration, H.-J. Behrend et al, Phys. Lett. **138B** (1984), p. 311.

41. MARK-J Collaboration, B. Adeva et al, Phys. Rev. Lett. **50** (1983), p. 2051.

42. JADE Collaboration, W. Bartel et al, Phys. Lett. **119B** (1982), p. 239; *II*, Z. Phys. C **25** (1982), p. 231.

43. MARK-J Collaboration, B. Adeva et al, MIT technical report number 148 (1986).

44. T. Sjostrand, DESY report **84-023** (1984).

45. CELLO Collaboration, H.-J. Behrend et al, Phys. Scripta **23** (1981), p. 610.

46. H. Desportes et al, *Construction and test of the CELLO thin wall solenoid*, Contribution to the 21st Cryogenic Engineering Conference, Wisconsin (1979).

47. M. Cohen, *Etude des performances des chambres proportionelles du detecteur central de CELLO, These 3eme cycle.*

48. U. Binder, *Diplomarbeit.*

W. de Boer et al, Nucl. Instr. and Meth. **156** (1978), p. 249.

W. de Boer et al, Nucl. Instr. and Meth. **176** (1980), p. 167.

49. B. Sack, *Diplomarbeit.*

50. H. Oberlack, General Meeting on LEP - Villers (1981).

F. Le Diberder, *Premiers resultats de calorimetres a Argon liquide avant et arriere de l'experience CELLO, These de 3eme cycle.*

E. Ros, *These de 3eme cycle.*

51. R. Aleksan et al, Nucl. Instr. and Meth. **185** (1981), 95–105.

J. Pamela, *These d'Etat.*

52. R. Pain, *These de 3eme cycle (unpublished).*

L. Poggioli, *Etude du detecteur avant de CELLO, application a la recherche d'une resonnance hadronique, These de 3eme cycle*, Universite de Paris-Sud (1981).

53. H.-J. Behrend, Computer Physics Comm. **22** (1981), 365–374.

54. CELLO Note O-073.

55. R. Aleksan, *Traitement des donnees en ligne pour une experience aupres de l'anneau de collision PETRA, These de 3eme cycle*, Universite Paris VII (1978).

56. D. Notz, Nucl. Inst. A **235** (1985), p. 380.

57. C. L. Basham et al, Phys. Rev. **D19** (1979), p. 2018.

58. T. Sjostrand, Computer Physics Comm. **27** (1982), p. 243; *II*, Computer Physics Comm. **28** (1983), p. 229.

59. F. A. Berends et al, Nucl. Phys B **177** (1981), p. 237; *II*, Nucl. Phys B **178** (1981), p. 141.

60. JADE Collaboration, W. Bartel et al, Z. Phys. C **25** (1984), p. 231.

61. TASSO Collaboration, R. Brandelik et al, Z. Phys. C **22** (1984), p. 307.

GLASGOW
UNIVERSITY
LIBRARY